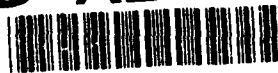


PL-TR-92-2117(II)

AD-A256 691



2

Research at the Center for Seismic Studies

*Lori Grant
Vladislav Ryaboy
Anne Suteau-Henson*

*Harley Benz
Steve Bratt
Jerry Carter
Dave Corely
William Leith
John Unger*

DTIC
ELECTE
AUG 12 1992
S A D

Science Applications International Corporation
Center for Seismic Studies
1300 N. 17th Street, Suite 1450
Arlington, VA 22209

30 April 1992

Final Report: Part II
October 1990 - March 1992

92-22624



92 8 10 108

APPROVED FOR PUBLIC RELEASE; DISTRIBUTION UNLIMITED



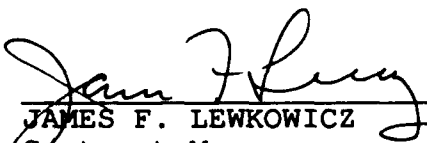
PHILLIPS LABORATORY
AIR FORCE SYSTEMS COMMAND
HANSCOM AIR FORCE BASE, MASSACHUSETTS 01731-5000

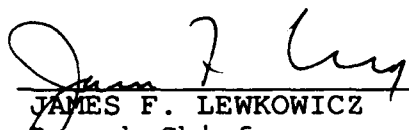
SPONSORED BY
Defense Advanced Research Projects Agency
Nuclear Monitoring Research Office
ARPA ORDER NO. 5307

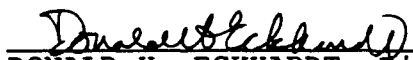
MONITORED BY
Phillips Laboratory
Contract No. F19628-89-C-0203

The views and conclusions contained in this document are those of the authors and should not be interpreted as representing the official policies, either expressed or implied, of the Defense Advanced Research Projects Agency or the U.S. Government.

This technical report has been reviewed and is approved for publication.


JAMES F. LEWKOWICZ
Contract Manager
Solid Earth Geophysics Branch
Earth Sciences Division


JAMES F. LEWKOWICZ
Branch Chief
Solid Earth Geophysics Branch
Earth Sciences Division


DONALD H. ECKHARDT, Director
Earth Sciences Division

This report has been reviewed by the ESD Public Affairs Office (PA) and is releasable to the National Technical Information Service (NTIS).

Qualified requestors may obtain additional copies from the Defense Technical Information Center. All others should apply to the National Technical Information Service.

If your address has changed, or if you wish to be removed from the mailing list, or if the addressee is no longer employed by your organization, please notify PL/IMA, Hanscom AFB, MA 01731-5000. This will assist us in maintaining a current mailing list.

Do not return copies of this report unless contractual obligations or notices on a specific document requires that it be returned.

REPORT DOCUMENTATION PAGE			Form Approved OMB No. 0704-0188	
<small>Public reporting burden for this collection of information is estimated to average 1 hour per response, including the time for reviewing instructions, searching existing data sources, gathering and maintaining the data needed, and completing and reviewing the collection of information. Send comments regarding this burden estimate or any other aspect of this collection of information, including suggestions for reducing this burden, to Washington Headquarters Services, Directorate for Information Operations and Reports, 1215 Jefferson Davis Highway, Suite 1204, Arlington, VA 22202-4302, and to the Office of Management and Budget, Paperwork Reduction Project (0704-0188), Washington, DC 20503.</small>				
1. AGENCY USE ONLY (Leave blank)		2. REPORT DATE April 30, 1992		3. REPORT TYPE AND DATES COVERED Final Report Part 2 (10/90-3/92)
4. TITLE AND SUBTITLE Research at the Center for Seismic Studies			5. FUNDING NUMBERS F19628-89-C-0203 PE 62714E PR 9A10 TA DA WU BI	
6. AUTHOR(S) Lori Grant, Vladislav Ryaboy, Anne Suteau-Henson, Harley Benz*, Steven Bratt, Jerry Carter, David Corley, William Leith*, John Unger*				
7. PERFORMING ORGANIZATION NAME(S) AND ADDRESS(ES) Science Applications International Corporation Center for Seismic Studies 1300 N. 17th Street, Suite 1450 Arlington, VA 22209			8. PERFORMING ORGANIZATION REPORT NUMBER	
9. SPONSORING/MONITORING AGENCY NAME(S) AND ADDRESS(ES) Phillips Laboratory Hanscom AFB, MA 01731-5000 Contract Manager: James Lewkowicz/GPEH			10. SPONSORING/MONITORING AGENCY REPORT NUMBER PL-TR-92-2117 (II)	
11. SUPPLEMENTARY NOTES * USGS				
12a. DISTRIBUTION/AVAILABILITY STATEMENT APPROVED FOR PUBLIC RELEASE; DISTRIBUTION UNLIMITED			12b. DISTRIBUTION CODE	
13. ABSTRACT (Maximum 200 words) This is Part II of a two part report. It contains papers primarily focused on regional monitoring of underground nuclear explosions. A broad spectrum of issues is addressed; from improving automatic processing to an assessment of monitoring capability using certain network configurations. The first two papers examine the use of three-component seismic data for phase identification; one applies discriminant analysis to the three-component IRIS/IDA stations in the former USSR in anticipation of those stations being added to the Intelligent Monitoring System (IMS), and the other applies the same techniques to the three component stations of ARCESS and NORESS in a comparison with newly-developed neural network techniques. The third section uses travel-time information from long range refraction profiles that is independent of the IMS to derive an average travel-time curve for Fennoscandia. In addition, regional variations in the Pn travel times are defined and used to relocate a small set of events. The fourth paper is the result of work performed on a Deep Seismic Sounding profile that was obtained by the USGS. The validity of the preliminary interpretation of the data by Russian Seismologists is examined in this paper. (continued on reverse)				
14. SUBJECT TERMS Phase identification, IMS, Polarization, DSS, Event Location, Seismic Noise, Regional Network			15. NUMBER OF PAGES 166	
			16. PRICE CODE	
17. SECURITY CLASSIFICATION OF REPORT UNCLASSIFIED	18. SECURITY CLASSIFICATION OF THIS PAGE UNCLASSIFIED	19. SECURITY CLASSIFICATION OF ABSTRACT UNCLASSIFIED	20. LIMITATION OF ABSTRACT SAR	

Block 13 continued:

The final two sections deal with monitoring networks. One presents the results of network simulation of the GSE Network using empirical noise calculations from the recent technical test. The other is a summary note on starting and improving a regional network. It summarizes and integrates the results of our research related to the way the US would proceed to monitor with an in-country regional network of three-component (3-C) stations and arrays.

Accession For	
NTIS CRA&I	<input checked="checked" type="checkbox"/>
DTIC TAB	<input type="checkbox"/>
Unannounced	<input type="checkbox"/>
Justification	
By	
Distribution/	
Availability Codes	
Dist	Avail and/or Special
A-1	

DTIC QUALITY INSPECTION

Table of Contents

List of Figures	v
------------------------------	----------

List of Tables	xii
-----------------------------	------------

Foreword	xiii
-----------------------	-------------

Initial Phase Identification at the IRIS/IDA Stations in the USSR

Introduction	1
Analysis of March 1989 Data	1
Analysis of April 1989 GAR Data	10
Comparison of IPI Using Two Different Polarization Recipes	16
Effect of Detection Threshold on Initial Phase Identification	18
Study of Misidentification	20
Conclusions and Discussion	21
References	23

Confidence in Initial Phase Identification from Polarization at ARCESS and NORESS: a Comparison between Discriminant and Neural Network Methods

Introduction	25
Confidence in Phase Identification From Discriminant Analysis	25
Comparison of Discriminant and Neural-Network Failures	29
Comparison of Discriminant and Neural-Network Confidence for Failures	40
Conclusions and Discussion	42
References	46

Implications of DSS Observations within Scandinavia and North-western Russia for IMS Data Processing

Abstract	47
Introduction	48
Pn Wave Analysis	49
Relocation of Seismic Events Originally Located by the IMS	68
Discussion and Conclusions	76
Acknowledgments	77
References	87

The Norilsk DSS Profile in Northern Siberia: an Analysis of the 2-d Crustal Velocity Section Constructed by Soviet Seismologists

Introduction	91
Geological and Geophysical Background	91
Analysis of the Crustal Velocity Model for the Norilsk DSS Profile	94
Conclusions	100
References	102

Simulations of Network Detection Capability Based on Noise Measurements from the GSETT-2 Experiment

Introduction	103
Description of the NETSIM Program	104
NETSIM Input Parameters	104
Seismic Networks	107
NETSIM Input Data from GSETT-2 Observations: Noise Study	107
Network Simulations of Detection Threshold	116
Summary	135
Future Work	136
Acknowledgments	136
References	137

Summary Note on Starting and Improving a Regional Network

Introduction	139
Azimuth Estimation	140
Phase Identification	141
Detection and Bulletin Production	141
Knowledge Acquisition	141
Conclusions	143
References	144

List of Figures

Initial Phase Identification at the IRIS/IDA Stations in the USSR

1. The densities of the three discriminant variables obtained at station GAR are displayed for the four detection groups: Teleseismic ("T"), Regional P ("P"), Regional S ("S"), and noise ("N").4
2. The success rate (in percent) of Initial Phase Identification at station GAR is plotted for each detection group: Teleseismic ("T"), Regional P ("P"), Regional S ("S"), and noise ("N"), and for the average of all groups ("A"). Three cases are shown: from *left to right*, only the first discriminant variable, the first two, and all three, were used for the classification.5
3. The densities of the three discriminant variables obtained at station ARU are plotted for each of the four detection groups (see Figure 1 for details).7
4. The densities of the three discriminant variables obtained at station KIV are plotted for each of the four detection groups (see Figure 1 for details).9
5. Box plots describing the distributions of four detection and polarization attributes measured at station GAR are displayed for each of the four detection groups: Teleseismic ("T"), Regional P ("P"), Regional S ("S"), and noise ("N"). The noise detections have average and dispersed values, except for SNR that tends to be low.12
6. Ratio of horizontal to vertical power ("H/V") is plotted against rectilinearity for the detections in the April 1989 dataset at GAR. Note that the variables are normalized and standardized. The noise detections ("N", circled) have close to average values of H/V for below average rectilinearity, but their values depart from average for above average rectilinearity.13
7. The distributions of a characteristic polarization attribute obtained using polarization recipes 1 and 2 are compared for the Teleseismic and noise detection groups. The April 1989 dataset for station GAR is used.19

Confidence in Initial Phase Identification from Polarization at ARCESS and NORESS: a Comparison between Discriminant and Neural Network Methods

8. The probability (in percent) of an arrival being of P-type is plotted, for those arrivals in the first testing set that were identified by the analyst as either P or S (*left and right* of the first vertical line, respectively), for various subsets of the data. The horizontal scale is identical for all plots, to facilitate the comparison.27

9. The probability (in percent) of an arrival being of P-type is plotted for those arrivals in the first testing set at ARCESS that were identified as S phases by the analyst. A low "P-probability" means a high confidence in the identification. The subset of arrivals between the dotted vertical lines has an anomalous distribution.28
10. The probability (in percent) of an arrival being of P-type is plotted for all arrivals in the first testing set at ARCESS. Eight subsets of the data are shown. From *left to right*: P correctly identified by both the Discriminant Analysis (DA) and Neural Network (NN) methods, P misidentified by both, P misidentified by DA, P misidentified by NN, S correctly identified by both, S misidentified by both, S misidentified by DA, S misidentified by NN.30
11. The probability (in percent) of an arrival being of P-type is plotted for all arrivals in the first testing set at NORESS. Eight subsets of the data are shown. From *left to right*: P correctly identified by both the Discriminant Analysis (DA) and Neural Network (NN) methods, P misidentified by both, P misidentified by DA, P misidentified by NN, S correctly identified by both, S misidentified by both, S misidentified by DA, S misidentified by NN.31
12. Boxplots show the distributions of the discriminant variable for eight subsets of the data in the first testing set (see text for details).32
13. a): the 3-component SNR is plotted for the subsets "P_DA_Fail" and "S_N_N_Fail" at ARCESS (*left* and *right* of the solid vertical line, respectively); b) same as a), but for the subsets "S_DA_Fail" (*left*) and "P_NN_Fail" (*right*); c): the tangent of incidence angle is plotted for the subsets "S_DA_Fail" (*left*) and "P_NN_Fail" (*right*); note the anomalous distribution for the arrivals between the two dotted vertical lines.35
14. a): the 3-component SNR is plotted for the subsets "P_DA_Fail" and "S_N_N_Fail" at NORESS (*left* and *right* of the solid vertical line, respectively); b) same as a), but for the subsets "S_DA_Fail" (*left*) and "P_NN_Fail" (*right*); c): the tangent of incidence angle is plotted for the subsets "S_DA_Fail" (*left*) and "P_NN_Fail" (*right*).36
15. Boxplots show the distributions of dominant frequency (*left*) and SNR (*right*) of the "best" detection beam for the four data subsets where initial phase identification from Discriminant Analysis (DA) and Neural Network (NN) differ.37
16. Maps show the locations of the events corresponding to various failure subsets at ARCESS. A triangle indicates the station location. *Left*: actual P misidentified by DA ("P_DA_Fail", *squares*) and actual S misidentified by NN

	("S_NN_Fail", <i>asterisks</i>). <i>Right</i> : actual S misidentified by DA ("S_DA_Fail", <i>squares</i>) and actual P misidentified by NN ("P_NN_Fail", <i>asterisks</i>).	38
17.	Maps show the locations of the events corresponding to various failure subsets at NORESS. A triangle indicates the station location. <i>Left</i> : actual P misidentified by DA ("P_DA_Fail", <i>squares</i>) and actual S misidentified by NN ("S_NN_Fail", <i>asterisks</i>). <i>Right</i> : actual S misidentified by DA ("S_DA_Fail", <i>squares</i>) and actual P misidentified by NN ("P_NN_Fail", <i>asterisks</i>).	39
18.	The confidence in the phase identification from Discriminant Analysis (DA) is plotted against the confidence from the Neural Network (NN) for the subsets of the data where one of the two methods failed (see text for details).	41
19.	Histograms are plotted for the distributions of confidence from Discriminant Analysis (DA) and Neural Network (NN), for actual S-type phases misidentified by the DA method. "Bad" refers to the subsets of arrivals from the period August 22 to September 3, 1990, with anomalous polarization measurements. The remaining arrivals form the "good" subsets.	43
20.	Same as Figure 18, except the "bad" data points have been removed.	44

Implications of DSS Observations within Scandinavia and Northwestern Russia for IMS Data Processing

21.	A map of DSS profile locations and Pg / Pn cross-over distance. 1 - 3 - DSS profiles with different methods of field observations, 4-5 - main shot points, 6 - Pg / Pn cross-over distance. DSS profile locations adapted from a paper (Sharov, 1991).	50
22.	Trace-normalized record sections from shot point (SP) D5 (FENNOLORA DSS profile) recorded at the NORSAR array (filter: 2 to 8 Hz). Azimuth from NORESS to SP D is 85.92°. Seismic wave amplitudes for top record section were increased relative to bottom one to search for low amplitude arrivals. One can see that the first arrivals of the Pn wave have small amplitudes, and later arrivals are stronger and usually have lower frequencies.	52
23.	Same as Figure 22 but for SP E4. Azimuth from NORESS array to SP E is 58.82°.	53
24.	Same as Figure 22 but for SP C1. Azimuth from NORESS array to SP C is 124.90°.	54
25.	Same as Figure 22 but for SP B4. Azimuth from NORESS array to SP B is 152.95°.	55

26. Top: same as Figure 22 but for SP H3 and SP I1. Azimuths from the NORESS array to SP H3 and SP I1 are 22.53 and 20.78 , respectively. Bottom: record section constructed from NORSAR recordings of a nuclear shot on 4 September 1972 (SP Kola) in the southwestern part of the Kola peninsula (Apatity area). Origin time and location of SP Kola are based on relocation results (Shore, 1982). Azimuth from NORESS array to SP Kola is 44.13 °. 56
27. NORESS recordings at a distance of 963.5 km from SP A (POLAR DSS profile in northern Norway and Finland). A2 - A5 are beams constructed with a velocity of 8.0 km/sec (filter: 2 to 8 Hz) for four different shots with charge 960 , 960, 1680, and 1680 kg, from top to bottom. A is a coherent stack of the four beams A2 - A5. One can see an improvement in SNR for the Pn wave after stacking the beams.57
28. Record section for the FENNOLORA DSS profile from SP I to the south (adapted from Hauser and Stangl, 1990). Note the delayed travel-time branch beyond 850-900 km, followed by an increased apparent velocity and frequency drop.59
29. Record section for the Oslo-Helsinki-Leningrad profile overlain by theoretical travel-time curves of waves refracted in two upper mantle layers separated by a low-velocity zone from approximately 105 to 135 km depth (adapted from Ryaboy, 1990). This record section was constructed mainly for mine explosions recorded at NORESS array. One can see that the first arrivals can be traced continuously to a distance of 800-850 km, where there is a break and shift of approximately 2.0 sec in the travel-time curve and an increase of apparent velocity.60
30. Record section for a North sea - southern Norway DSS profile (adapted from Cassell *et al.*, 1983). Shots were detonated in the North Sea and seismic waves were recorded within southern areas of the Baltic shield. The records beyond 450 km were recorded by the NORSAR array. The azimuth from NORESS is 224.75 . The P_g / Pn cross-over distance is 150 km.61
31. Top: record section for the SVEKA DSS profile in central Finland from shot point E (adapted from Luosto *et al.*, 1984). Bottom: the record section is shown on an enlarged scale for the distance range of 180-260 km. The P_g / Pn cross-over distance is approximately 270km . A wave refracted in the lower crust with apparent velocity 7.35 km/sec was recorded within the distance range 210-270 km.62
32. Results from ultrasonic modelling (A and B) and record section (C) of waves generated in media with a dipping interface (adapted from Berzon, 1977). A - physical model of the medium (S-1 and S-2 are sources of vibration; velocities and densities vary on boundaries 1 and 2). B - record section

- constructed for source of vibration S-1 (P - refracted wave, (PP)1 - wave reflected from dipping interface 1, (PP)2 - wave reflected from horizontal interface 2; (PP)1 wave was not recorded for source of vibration S-2). C - example of record section constructed for refraction profile in Altay region crossing a dipping overthrust (Pg - wave refracted in the basement, P1 - wave reflected from the overthrust).64
33. Pn-wave travel-times for Scandinavia and northwestern Russia. One can see a large scatter in Pn travel-times and discrepancies of up to 2-3 sec at distances greater than 500-600 km between DSS data and Pn travel-time curves used to locate events for the IMS and Helsinki University seismological bulletins.66
34. Density plot of Pn travel-time residuals.67
35. A map of Pn-wave travel-time residuals for the distance range from the Pg / Pn cross-over point to 400 km. 1-3 - DSS profiles with different methods of field observations, 4-5 - main shot points, 6 - isolines of Pn travel-time residuals in sec. The DSS profile locations are adapted from Sharov (1991).69
36. A map of locations of selected events and regional seismic arrays. I, II, III, and IV are groups of events selected for testing. Solid lines are boundaries between the event groups. NEW, NOR1, and NOR2 are zones with different Pn travel-time curves around the NORESS array. Dashed lines are boundaries between azimuth zones with constant Pn travel-time curves. The zones and their travel-time curves have the same designations (see Figure 37).70
37. Pn travel-time curves developed for NORESS array. NOR1 and NOR2 are travel-time curves constructed for zones to south and east from NORESS array (see Figure 36). NEW is the new Pn reference travel-time curve used for areas without pronounced residuals from the reference travel-time curve. As comparison, Pn travel-time curve (IMS) used for location events by the IMS system is also shown.71
38. Density plots of distance (top) and origin time differences (bottom) between relocated events and the IMS bulletin for new Pn and Sn (solid lines) and new Pn (dotted lines) travel-time tables inferred from DSS data.73
39. Comparison of locations of relocated events (crosses) and events listed in the IMS bulletin (small squares) for area 1 (top) and area 2 (bottom).74

The Norilsk DSS Profile in Northern Siberia: an Analysis of the 2-d Crustal Velocity Section Constructed by Soviet Seismologists

40. Location map of the DSS profiles in Northern Siberia and neighboring regions: 1-1 -- Norilsk profile, 2-2 -- Dikson-Khilok profile, 3-3 -- Vorkuta-

	Tixsie profile, 4-4 -- a profile based on recordings of mine explosions. Adapted from Egorkin et al.,(1989) with additions.	92
41.	Field observation system for the Norilsk DSS profile.	93
42.	Crustal velocity section constructed by Soviet seismologists (A.V. Egorkin, L.N. Solodilov <i>et al.</i>) for the Norilsk profile. Numbers are velocities of P- and S-wave in km/s (above and below lines, respectively). Vertical exaggeration is 10:1.	95
43.	Two-dimensional crustal velocity model used for calculations of theoretical travel-time curves and synthetic seismograms. The model is a generalized version of the crustal velocity section constructed by Soviet seismologists for the Norilsk DSS profile (Figure 42). Numbers are P-wave velocities (in km/s) within crustal layers and blocks, and beneath the Moho.	96
44.	Two-dimensional ray tracing for reversed and overlapping shot points SP1 (top), SP73 (bottom). Open squares denote observed travel-times for first arrivals. Theoretical travel-time curves of reflected and refracted waves and ray paths are shown in solid lines.	97
45.	Synthetic (A) and observed (B and C) record sections of P-waves for SP17. Recordings (B and C) are trace-normalized and bandpass filtered between 3 and 10 Hz. Seismic wave amplitudes for (C) were increased relative to (B) to search for low amplitude arrivals. Solid lines on record sections (B) and (C) denote theoretical travel-time curves for first arrivals.	98
46.	Same as Figure 45, but for SP73.	99

Simulations of Network Detection Capability Based on Noise Measurements from the GSETT-2 Experiment

47.	Schematic flow diagram for NetSim. Taken from Sereno <i>et.al.</i> 1990.	105
48.	Stations used in simulations. GSETT-2 stations are denoted by a cross inside a circle; GSETT-2 arrays by a cross inside a square; and open circles represent additional stations in the hypothetical network.	108
49.	Power spectral density of noise measured on GSETT-2 waveforms. Units are in dB relative to 1 nm ² /Hz. 5-second windows begin 15 seconds and end 10 seconds before reported first P-phase. Noise spectra were corrected for the instrument response received from each station during GSETT-2.	113
50.	Nyquist frequency (open square) and cut-off frequency (solid dot) for each GSETT-2 station with noise measurements	115
51.	One noise spectrum from each of groups 1-5. Station LTX is in the lowest noise-level group, 1. Station KIV is in the highest noise-level group, 5. A 30	

	dB difference in noise levels between groups 1 and 5 is observed through the 2 to 10 Hz band. Cut-off frequencies are shown in parenthesis to the right of the station name.	117
52.	World map showing 6 areas for quantitative comparison of simulation results.(1)Eurasia, (2) Australia and Southeast Pacific Ocean, (3) Indian Ocean and South Atlantic Ocean, (4) South America and Southwest Pacific Ocean, (5) North America and North Atlantic Ocean.	118
53.	90% M_{Lg} Detection Threshold for GSETT-2 Network. (a) Detection criteria of 2 P phases at any 2 stations. (b) Detection criteria of 3 P phases at any 3 stations. (c) Difference between (b) and (a) showing increase in detection threshold when 3 P's are required versus 2 P's for a valid event.	124
54.	90% M_{Lg} Detection Threshold for 12-Array Network. (a) Detection criteria requiring 3 P phases at any three stations.(b) Detection criteria requiring 2 P phases at any two stations or one Pg and one Lg at any station.	127
55.	90% M_{Lg} Detection Threshold for 4-Array Network. (a) Detection criteria requiring 3 P phases at any three stations.(b) Detection criteria requiring 2 P phases at any two stations or one Pg and one Lg at any station.	129
56.	90% M_{Lg} Detection Threshold for Hypothetical 85-Station Network. (a) Detection criteria requiring 3 P phases at any three stations.(b) Difference plot showing theoretical improvement in detection threshold compared to the GSETT-2 Network shown in Figure 53(b).	133

List of Tables

Initial Phase Identification at the IRIS/IDA Stations in the USSR

1.	Performance of Initial Phase Identification at GAR	5
2.	Performance of Initial Phase Identification at GAR, ARU, and KIV	10
3.	Comparison of the Classification Performance at GAR for Two Datasets	14
4.	Performance of the Classification at GAR as a Function of SNR	14
5.	Comparison of Classification Performance for Two Polarization Recipes	17
6.	Comparison of Classification Performance for Two Detection Thresholds	20
7.	Misidentification Results	21

Confidence in Initial Phase Identification from Polarization at ARCESS and NORESS: a Comparison between Discriminant and Neural Network Methods

8.	Comparison of DA and NN Failure Sets	29
----	--	----

Implications of DSS Observations within Scandinavia and Northwestern Russia for IMS Data Processing

9.	Comparison of IMS Locations and Locations Using New P_n and S_n Tables	78
10.	Comparison of IMS bulletin with two-array (NORESS, FINESA) locations	84

Simulations of Network Detection Capability Based on Noise Measurements from the GSETT-2 Experiment

11.	SNR Thresholds by Phase and Station Type.	107
12.	Stations Used in the Simulations	109
13.	Noise Data for Each Station	119
14.	GSETT-2 90% M_{Lg} Detection Threshold	131
15.	GSETT-2 Sub-networks 90% M_{Lg} Detection Threshold, Requiring 3 P	132
16.	GSETT-2 Sub-networks Requiring 2 P or 2 Local Phases	132
17.	Hypothetical 85-Station Network Requiring 3 P Phases	135

Foreword

Jerry A. Carter

This is the final report of a multi-year effort by the researchers at the Center for Seismic Studies under contract # F19628-89-C-0203. The papers presented within are not a complete description of all of the work that was performed under this contract; rather, they represent the research that was performed in the last 15 months of the contract. Previous work is described in PL-TR-91-2127, *Nuclear Monitoring Research at the Center for Seismic Studies*.

The report has been divided into two parts. The first part is devoted entirely to a description of, and research performed on, the hand digitized waveforms of Soviet regional data that were obtained by Dr. Alan Ryall of DARPA and Sgt. Mike Berry of AFTAC as part of the bi-lateral Nuclear Testing Talks between the U.S. and the former U.S.S.R. Digitized by ENSCO Inc. at Indian Harbour Beach, FL., the data were subsequently compiled by Dr. Herron and her staff at AFTAC and are now available at the Center for Seismic Studies. The first paper of Part I is a description of the data. This is followed by two papers that analyze the RMS Lg magnitudes at Novaya Zemlya and Semipalatinsk, respectively. The Semipalatinsk report also compares the RMS Lg measurements and the Bocharov yields as well as exploring the effects of depth on the magnitude measurement. The fourth paper combines the data from the two test sites with data from underground nuclear explosions elsewhere in the former Soviet Union in a decomposition of the RMS Lg measurement into source, path, and station terms. The last paper in Part I examines the RMS Lg measurement as a function of frequency in order to explain the variability of the $m_b(Lg)$ - yield scale among stations.

Part II contains reports primarily focused on regional monitoring of underground nuclear explosions. A broad spectrum of issues is addressed; from improving automatic processing to an assessment of monitoring capability using certain network configurations. The first two papers examine the use of three-component seismic data for phase identification; one applies discriminant analysis to the three-component IRIS/IDA stations in the former USSR in anticipation of those stations being added to the Intelligent Monitoring System (IMS), and the other applies the same techniques to the three component stations of ARCESS and NORESS in a comparison with newly-developed neural network techniques. The third report uses travel-time information from long range refraction profiles that is independent of the IMS to derive an average travel-time curve for Fennoscandia. In addition, regional variations in the Pn travel times are defined and used to relocate a small

set of events. This type of regional knowledge, when incorporated into event location routines, should reduce location errors. The fourth report is the result of work performed on a Deep Seismic Sounding profile that was obtained by the USGS. A reinterpretation of this data has been made by the USGS and the results were reported at various meetings. The Centers contribution was to determine the validity of the preliminary interpretation of the data. H. Benz, J. Unger, and W. Leith, though not funded under this contract were co-authors of this report. The final two reports in Part II deal with monitoring networks. One presents the results of network simulation of the GSE Network using empirical noise calculations from the recent technical test. This research was funded primarily by the Center for Seismic Studies Contract and was co-authored by Steve Bratt and David Corely. Because the research is germane to this contract, some of the effort was funded under the research contract and we include it in this final report. The final report is a summary note on starting and improving a regional network. It summarizes and integrates the results of our research related to the way the US would proceed to monitor with an in-country regional network of three-component (3-C) stations and arrays.

Initial Phase Identification at the IRIS/IDA Stations in the USSR

Anne Suteau-Henson

Introduction

In a previous study (Riviere *et al.*, 1992) Initial Phase Identification (IPI) at the IRIS/IDA stations in the USSR was investigated. Approximately one month of data in March 1989 was analyzed, at stations GAR, ARU, and KIV (not enough data were available at OBN). Arrivals identified as either Teleseismic P, Regional P or Regional S by the analyst were classified using an automated procedure based on multivariate discriminant analysis. In the operation of the Intelligent Monitoring System (IMS, Bache *et al.*, 1990) many detections are not identified as seismic arrivals by the analyst. These can be glitches, coda detections, or noise detections, and must also be processed. In practice, the IPI module in the IMS uses four groups to classify detections for array data: Teleseismic, Regional P, Regional S, and Noise. The first three groups include coda detections, as well as actual seismic arrivals.

In this report we extended the previous study for continuous March 1989 data to include a fourth category of detections, namely, "noise detections". We did not include glitches in our analysis. Presumably, an effective deglitcher would remove most of them. Also, coda detections were not part of this dataset. Then, detections from event segments recorded at GAR in April 1989 were analyzed in a similar way. A comparison of signal and noise characteristics was performed for this dataset, to gain insight into the limitations of IPI at this 3-component (3-C) station when noise detections were included. A set of coda detections was assembled to investigate how the discriminant function classifies them.

Additional studies were conducted on the April 1989 dataset. The first was a comparison of IPI for two different polarization recipes, in order to assess if the recipe selected to optimize backazimuth estimation would also perform satisfactorily for IPI. The effect of varying the detection threshold was also investigated, to determine if increasing the threshold would improve the classification performance. Finally, we studied the classification of misidentified detections, thus identifying which specific groups the discriminant had difficulty separating.

Analysis of March 1989 Data

As described in Riviere *et al.* (1992) IPI in the IMS is an automated process which is based on measurements of detection characteristics. These measurements are stored in the

IMS database. Such a process has been successfully implemented at the Scandinavian arrays, where it relies on measurements of apparent velocity from f-k analysis. At single 3-C stations other types of measurements must be used. Our previous study indicated that a combination of polarization and frequency characteristics could be used to classify most detections corresponding to seismic arrivals as Teleseismic, Regional P, or Regional S, at GAR, ARU, and KIV. The success rate varied from 67% to 93%, depending on phase type and station.

In this section, noise detections are added to the dataset of continuous data from March 1989, that was used in our previous study. Since noise detections are characterized, in general, by low SNR, SNR was added to the set of measurements. Both STA/LTA of the "best" filtered channel that detected (i.e., SNR stored in the ARRIVAL database table) and 3-C SNR from polarization analysis (i.e., SNR stored in the APMA table) were used. The other nine measurements were the same as previously: dominant frequency from detection, "best" detection channel (horizontal or vertical), center frequency from polarization analysis, rectilinearity, planarity, ratio of horizontal to vertical power (measured assuming either P- or S-type motion), incidence angle of the long axis, and incidence angle of the short axis of the polarization ellipsoid. The same classification technique based on Discriminant Analysis (DA) was applied to separate the four detection groups. As previously, each station was studied separately.

GAR

At GAR 305 noise detections were added to the set of 108 Teleseismic P, 767 Regional P, and 854 Regional S. The dataset was divided into training and testing samples of about equal size. Discriminant Analysis was performed, varying the number of Principal Components (PC's) used as predictors of phase type. A study of the correlation between detection groups and discriminant variables indicated it was not necessary to include more than the first 5 PC's in the analysis. They account for 67% of the standard deviation in the data. Three discriminant variables were obtained, with correlations of 79%, 45%, and 36%, respectively:

- The first discriminant variable is mostly correlated with polarization: it has high values for detections on the vertical channel, with high rectilinearity, low horizontal-to-vertical power ratio, motion mostly in a near-vertical plane (i.e., large short-axis incidence), and low incidence angle.
- The second is mostly correlated with frequency: it has high values for detections with low dominant frequency.
- The third is mostly correlated with SNR: high values occur for detections with high

SNR .

Figure 1 shows plots of the densities of the three discriminant variables for each of the four groups forming the training set. Similar results are obtained for the testing set. We observe that:

- The values of the first discriminant variable (*top*) are high for Teleseismic P, intermediate for Regional P and noise, and low for Regional S. This is consistent with the fact that it is correlated with P-type polarization. It separates Teleseismic and Regional P from Regional S and noise.
- The second discriminant variable (*middle*) has high values for Teleseismic P, and low values for Regional P and S. This is consistent with its correlation with low dominant frequency. It separates Teleseismic from Regional P.
- The third discriminant variable (*bottom*) is characterized by high values for Teleseismic, and low values for noise, in agreement with our observation that SNR is lower for noise, on average. It helps separate noise from Regional S.

Therefore, the first two discriminant variables are similar to those obtained in our previous study, and help separate the three seismic phase groups. The third is necessary to further distinguish noise detections from seismic arrivals.

Table 1 shows the performance of the discriminant variables, i.e., the success rate in percent, for each detection group, and for the average of all groups. Results are shown for three cases: only the first discriminant variable included, the second added, and all three used. In each case, the first line corresponds to the training set, the second, to the testing set, and the third, to their average. The results for the average of the training and testing sets are also displayed in Figure 2. We observe that :

- The overall success rate increases from 58%, to 66%, to 76%, as more discriminant variables are added. Therefore, all three are required to correctly identify three out of four detections. In particular, it is necessary to include SNR as a predictor to improve the success rate.
- The best success rate is obtained for teleseismic phases (82%), while it is 73-74% for the other groups. Including more discriminant variables slightly degrades the performance for some detection groups (Teleseismic, Regional S), while significantly enhancing that of other groups (Regional P, noise).
- Results for the training and testing sets are similar for some groups (Regional), but differ more for others (Teleseismic, noise), possibly due to smaller populations.

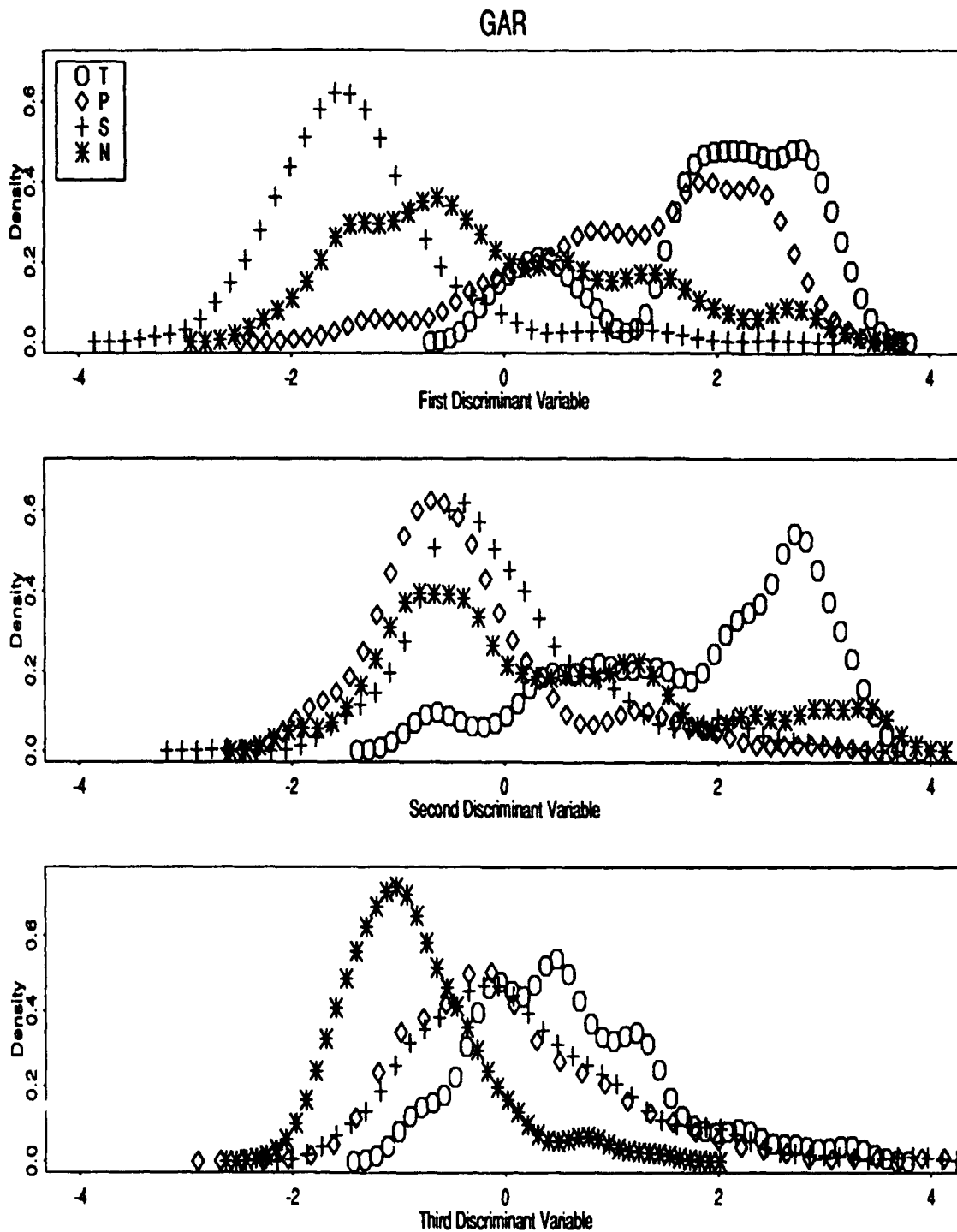


Figure 1: The densities of the three discriminant variables obtained at station GAR are displayed for the four detection groups: Teleseismic ("T"), Regional P ("P"), Regional S ("S"), and noise ("N").

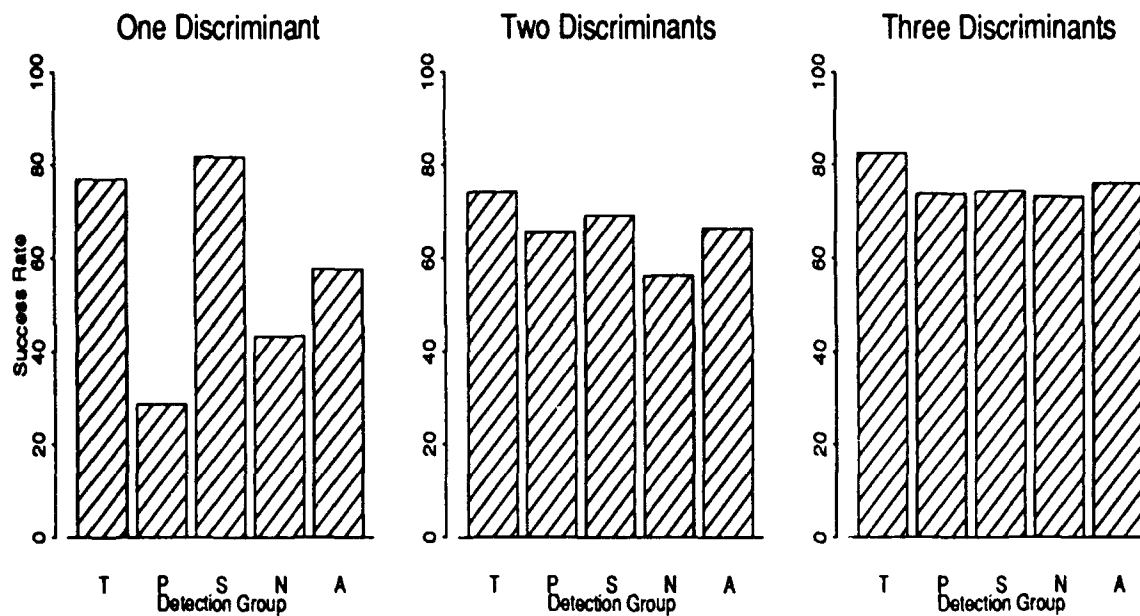


Figure 2: The success rate (in percent) of Initial Phase Identification at station GAR is plotted for each detection group: Teleseismic ("T"), Regional P ("P"), Regional S ("S"), and noise ("N"), and for the average of all groups ("A"). Three cases are shown: from *left to right*, only the first discriminant variable, the first two, and all three, were used for the classification.

Table 1: Performance of Initial Phase Identification at GAR

	Tele P	Reg P	Reg S	Noise	All
1 Discriminant	74.1%	28.4%	80.6%	43.1%	56.5%
	79.6%	29.0%	82.7%	43.4%	58.7%
	76.9%	28.7%	81.7%	43.3%	57.6%
2 Discriminants	68.5%	66.1%	69.6%	50.3%	63.6%
	79.6%	64.8%	68.6%	61.8%	68.7%
	74.1%	65.5%	69.1%	56.1%	66.2%
3 Discriminants	79.6%	74.5%	74.2%	69.9%	74.6%
	85.2%	73.1%	74.2%	76.3%	77.2%
	82.4%	73.8%	74.2%	73.1%	75.9%

ARU

At ARU, 203 noise detections were added to the set of 56 Teleseismic P, 74 Regional P, and 101 Regional S. Because of the small size of the dataset, we did not divide it into training and testing samples, except for the subset of noise detections. The first four Principal Components were included in the discriminant analysis. They account for 58% of the standard deviation in the data. The correlation between discriminant variables and groups is 79% for the first, 63% for the second, and 35% for the third, and they have the following characteristics:

- The first is mostly correlated with polarization, and high values characterize P-type phases.
- The second is mostly (inversely) correlated with SNR, and also with dominant frequency (the reverse of the third discriminant variable at GAR).
- High values of the third characterize detections on the horizontals, with high rectilinearity and planarity.

Figure 3 displays the densities of the three discriminant variables for the four groups. The noise subset shown is the training set, but similar results are obtained for the testing set. We observe the following:

- As expected, the first discriminant variable has high values for Teleseismic, intermediate values for Regional P, and low values for both Regional S and noise.
- The values of the second are high for noise and regional P, intermediate for Teleseismic, and low for Regional S. Therefore, it helps separate noise from Regional S.
- The third is not very efficient at separating the groups, but its values decrease, on average, from noise, to Teleseismic, Regional S, and Regional P.

The performance of the discriminant variables for each detection group, and for the average of all groups is as follows (the results for the training and testing noise subsets have been averaged):

- The overall success rate rises from 59% to 73% when the second discriminant variable is added, but does not increase with the third.
- The third discriminant variable causes a significant increase in the success rate for Regional P (from 53% to 64%), at the slight expense of each of the other groups.
- Teleseismic P has the highest success rate (82%), that for Regional S and noise is 72%, and Regional P has the lowest rate (64%).

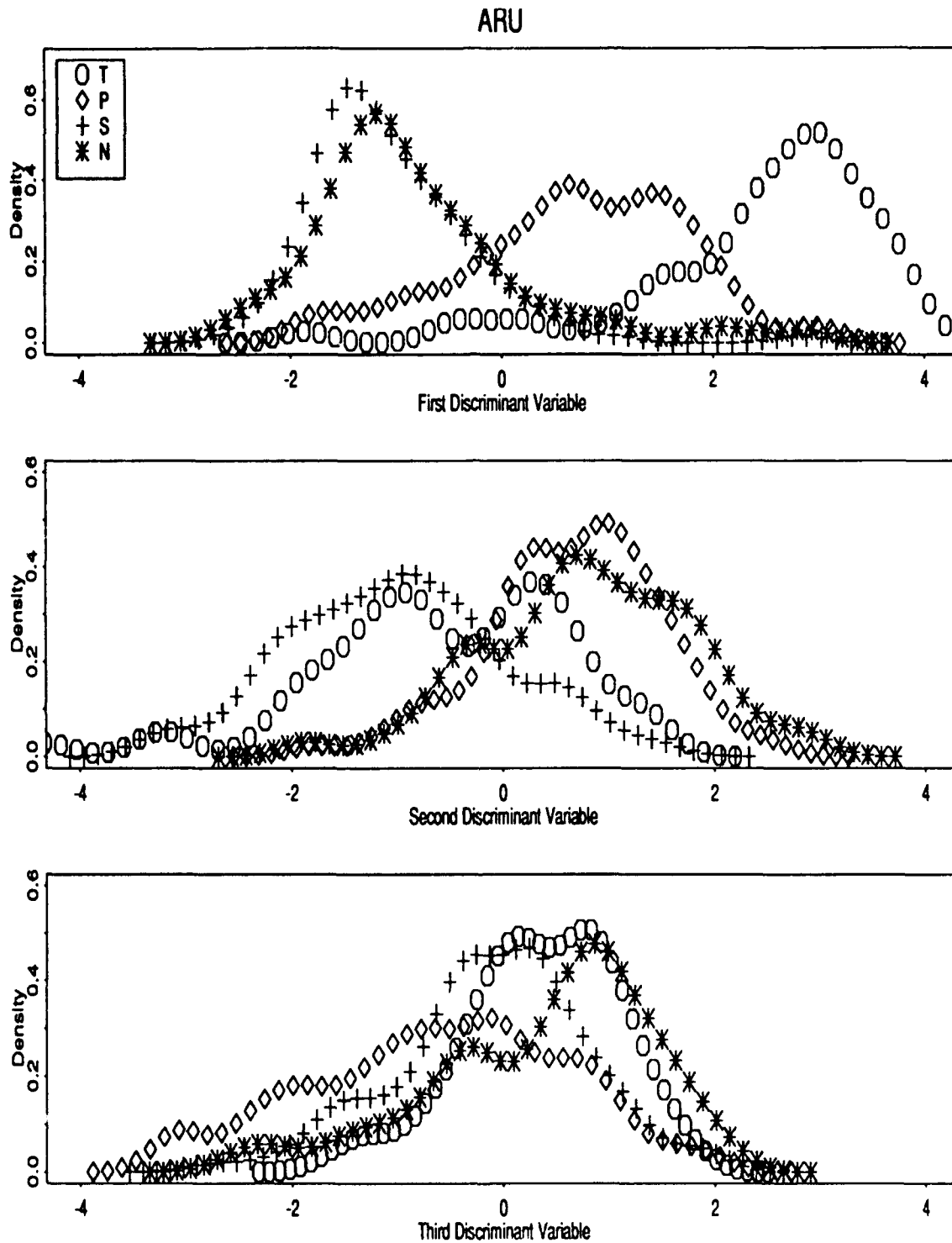


Figure 3: The densities of the three discriminant variables obtained at station ARU are plotted for each of the four detection groups (see Figure 1 for details).

- The results for the training and testing noise subsets are similar, but testing should be performed for the other groups as well, when enough data are available, to confirm these preliminary results.

KIV

At KIV 168 noise detections were used. They were added to 51 Teleseismic, 41 Regional P and 40 Regional S. A testing sample was formed for the noise group only, due to the small size of the other groups. The first five Principal Components (accounting for 65% of the standard deviation in the data) were used in the discriminant analysis. The correlation between groups and discriminant variables was 76%, 63%, and 47%, for the first, second and third discriminant variable, respectively. We observe that:

- The first discriminant variable is mostly correlated with polarization and frequency: high values correspond to detection on the horizontals, high horizontal-to-vertical power ratio, particle motion dominantly in a horizontal plane, large incidence (i.e., S-type polarization) and high frequency.
- High values of the second discriminant variable correspond to detections with low rectilinearity and high SNR.
- The third is correlated with detection on the horizontals and low dominant frequency.

Figure 4 displays the densities of the three discriminant variables for the four detection groups (the noise training set is shown). The following results are obtained:

- The first discriminant variable has high values for Regional S, intermediate values for noise and Regional P, and low values for Teleseismic.
- The second shows much overlap, but, on the average, decreases from Regional S, to Regional P, Teleseismic, and noise. Noise detections at KIV are characterized by low SNR, but also high rectilinearity, and therefore, adding the second discriminant variable helps separate this group from the others.
- The third helps separate Regional P from the other groups, since Regional P is characterized by low values (detection on the vertical and high frequency).

The performance of the classification as more discriminant variables are added can be summarized as follows:

- The overall success rate increases from 58% to 67% with the second discriminant variable, and to 72% with the third.

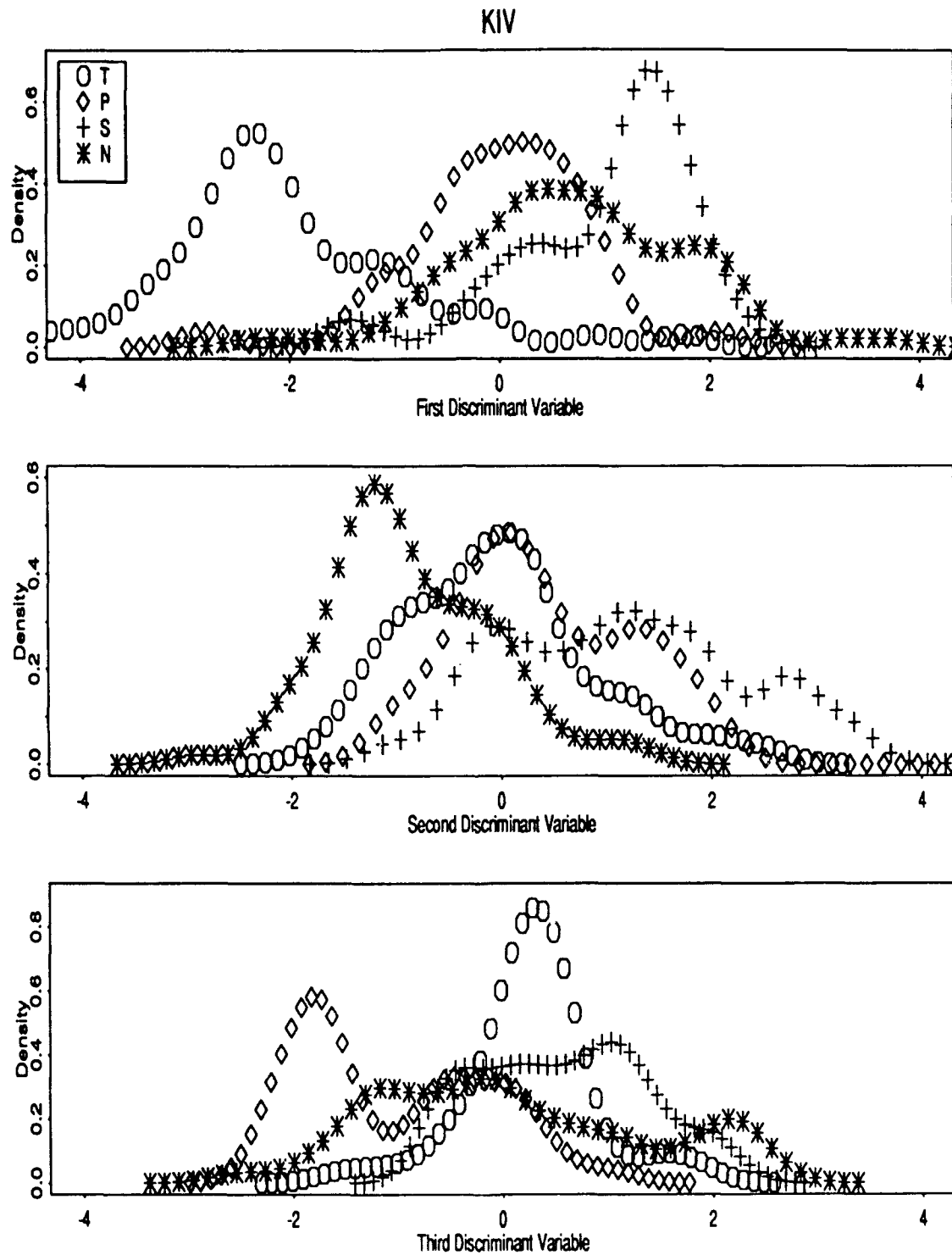


Figure 4: The densities of the three discriminant variables obtained at station KIV are plotted for each of the four detection groups (see Figure 1 for details).

- The addition of the third discriminant variable causes a significant improvement in the identification of Regional P (from 49% to 66%).
- The highest success rate is obtained for Teleseismic (80%), while Regional P, Regional S and noise have rates of 66%, 68%, and 73%, respectively.
- Similar results are obtained for the training and testing noise samples.

Conclusions

Table 2 summarizes the performance of the procedure for each station, when all three discriminant variables are used.

Table 2: Performance of Initial Phase Identification at GAR, ARU, and KIV

Station	Tele P	Reg P	Reg S	Noise	All
GAR	82%	74%	74%	73%	76%
ARU	82%	64%	72%	73%	73%
KIV	80%	66%	68%	73%	72%

The main conclusions of this study are:

- The performance of the discriminant analysis is about 75% for all stations (i.e., three out of four detections are correctly identified). The performance is best at GAR and worst at KIV.
- Teleseismic P has the highest success rate, on the order of 80%, at all three stations.
- At ARU and KIV, the success rate for Regional P is relatively low (about 65%).
- The relative performance for the various seismic phase groups compares well with that obtained in our previous study (Riviere *et al.*, 1991, Table 5), except for Regional S, for whom the performance is significantly degraded.
- This success rate of about 75% for Initial Phase Identification when noise detections are included falls short from the goal of 90% set for the IMS.

Analysis of April 1989 GAR Data

Event segments from data recorded in April 1989 at station GAR were processed and analyzed

using the same procedure as for the March 1989 continuous data, after some improvement was made in the signal processing software. The azimuthal dependence of polarization of Regional P found with the previous dataset (Riviere *et al.*, 1991) is still observed: local and regional events from the South arrive at steeper incidence angles than those from the North. A total of 350 detections were studied: 72 Teleseismic, 38 Regional P, 37 Regional S, and 203 noise detections. In the following, we compare noise characteristics to those of signals of the various types. Then, we perform Initial Phase Identification on this dataset, and compare the results with those obtained with the dataset of continuous March 1989 data. Finally, we use the results of Discriminant Analysis to classify coda detections.

Comparison of Signal and Noise Characteristics

In general, the three signal groups (Teleseismic, Regional P, Regional S) have distinctive characteristics, while the noise group significantly overlaps with at least one of the other groups. This is illustrated in Figure 5, that displays some characteristic detection and polarization attributes for each group. P phases are mostly detected on the vertical (93% of Teleseismic and 79% of Regional P), and S phases on a horizontal channel (89%), while noise detections are approximately as likely to be detected on the vertical (43%) as on a horizontal channel. The most distinctive characteristic of noise is its relatively low detection SNR, although some overlap is observed too.

Figure 6 shows the ratio of horizontal to vertical power (H/V) vs. rectilinearity (normalized and standardized variables) for all detections. The data points corresponding to the noise detections are circled. Noise detections with below average rectilinearity have H/V close to average, as expected. However, 57% of all noise detections have above average rectilinearity, and are characterized by either small or large values of H/V. This property makes it more difficult to distinguish them from seismic phases. It indicates that some noise detections that are well polarized may actually be seismic signals, not identified as such by the analyst because of their low SNR. However, it is possible for real noise detections to be well polarized and have characteristics close to those of a seismic phase group.

Initial Phase Identification

Initial Phase Identification was performed using the technique previously applied to the March 1989 data. Because of the small population of regional phases no testing sample was used to test the validity of the discriminant variables obtained. The results of this pre-

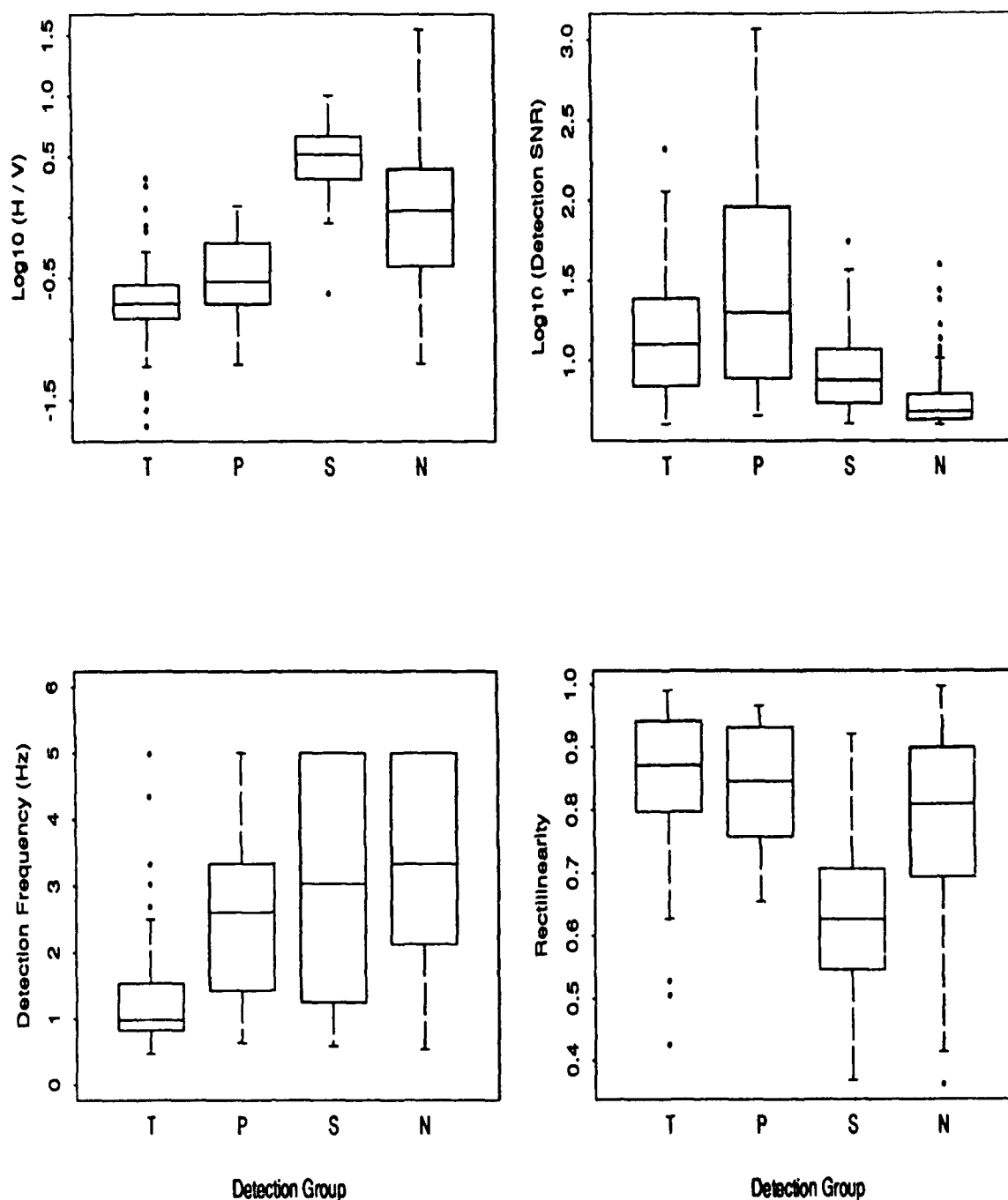


Figure 5: Box plots describing the distributions of four detection and polarization attributes measured at station GAR are displayed for each of the four detection groups: Teleseismic ("T"), Regional P ("P"), Regional S ("S"), and noise ("N"). The noise detections have average and dispersed values, except for SNR that tends to be low.

Detections at GAR, April 1989

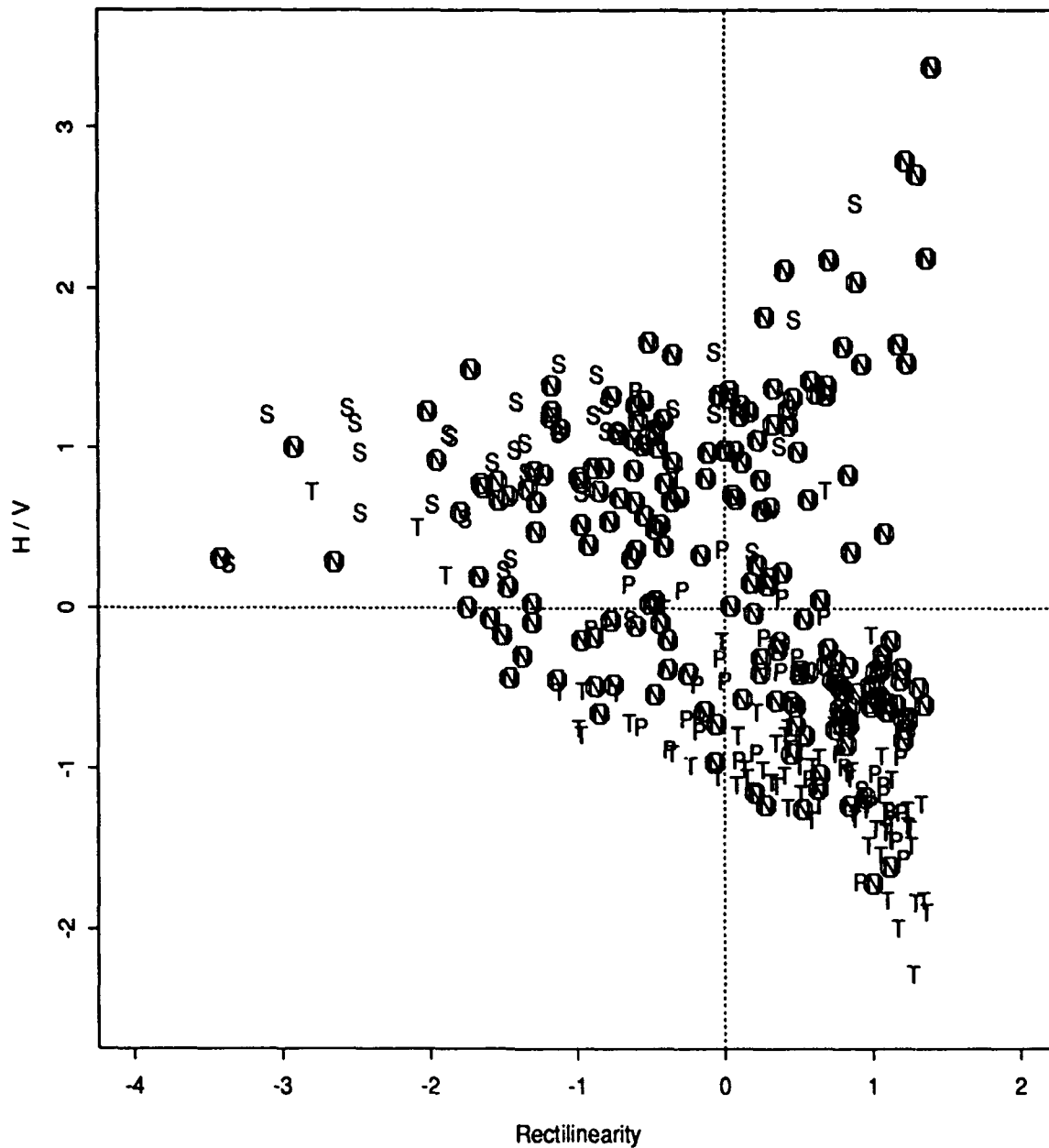


Figure 6: Ratio of horizontal to vertical power ("H/V") is plotted against rectilinearity for the detections in the April 1989 dataset at GAR. Note that the variables are normalized and standardized. The noise detections ("N", circled) have close to average values of H/V for below average rectilinearity, but their values depart from average for above average rectilinearity.

liminary study are compared to those for March 1989 in Table 3.

Table 3: Comparison of the Classification Performance at GAR for Two Datasets

Dataset	Tele P	Reg P	Reg S	Noise	All
March 1989	82%	74%	74%	73%	74%
April 1989	78%	71%	86%	74%	76%

The overall performance of the classification is not significantly better for the April 1989 dataset, in spite of the improvement in signal processing software. The only detection group showing some improvement is the Regional S group. We suspect that the characteristics of the noise detections (described in the previous subsection) are an intrinsic limitation of our analysis. However, one must exercise caution in comparing those two sets of results for the following reasons:

- The second set is much smaller and the relative sizes of the various groups are different. In particular, the proportion of noise detections is much larger (58% instead of 15%). This group is dispersed in both polarization and dominant frequency, and overlaps much with the other groups, so that increasing its relative size might degrade the performance.
- Also, no testing set was used for April 1989.
- The second set is made up of detections from selected event segments as opposed to continuous data. Since SNR is the major factor distinguishing noise detections from seismic phases, we expect the effect of SNR on the classification performance to be important. The performance is given in Table 4 for the subsets of the April 1989 data with detection SNR < 7 and > 7, respectively. Note that the total and relative sizes of the populations for these two subsets differ.

Table 4: Performance of the Classification at GAR as a Function of SNR

Subset	Tele P	Reg P	Reg S	Noise	All
SNR < 7	67%	43%	82%	79%	77%
SNR > 7	81%	77%	90%	50%	74%

The overall performance in each case is still similar to those previously obtained. For SNR < 7, the performance of the P phase groups is strongly degraded, while about 80% of Regional S and noise detections are correctly identified. For SNR > 7, 82% of seismic arrivals, but only one out of two noise detections is correctly identified. This trade-off results from our use of SNR as a discriminant between noise and seismic phases.

Classification of Coda Detections

The dataset used to obtain the discriminant variables did not include coda detections. In this subsection we classify a set of coda detections, using those discriminant variables. We expect coda detections to be classified as either "noise" or the corresponding seismic phase. The following results were obtained:

- **Teleseismic:** Out of 144 Teleseismic coda detections, 77% were "correctly" classified as noise (60%) or Teleseismic (17%), while 23% were "incorrectly" classified as Regional (16% S and 7% P).
- **Regional P:** Out of 35 Regional P coda detections, 9% were incorrectly classified as Teleseismic, 51% were classified as Regional S, 29% as Regional P, and 11% as noise. The high proportion of detections classified as S may reflect P to S conversions.
- **Regional S:** There were only 12 Regional S coda detections in the event segments processed, which does not provide an adequate statistical sample. Half were classified as noise, only one as Teleseismic, and the remaining five as Regional S.

Conclusions

- Noise detections are distinguished from seismic arrivals mainly through their low SNR. Their dominant frequency and polarization distributions tend to have average means and large variances, and strongly overlap with those of seismic arrivals.
- The performance of Initial Phase Identification did not significantly improve, compared to the March 1989 results, in spite of improvements in the signal processing software. The regional S group only showed some improvement. Note, however, that a much smaller dataset was used, and more data would be required to reach definite conclusions. The performance is sensitive to SNR, and 82% of seismic arrivals are correctly identified for $\text{SNR} > 7$. The lack of significant improvement in the overall performance is attributed to the dispersion of the noise group, in both dominant frequency and polarization.
- Most coda detections were "correctly" classified as either noise or the corresponding seismic phase. One exception is Regional P coda detections, that were half the time identified as Regional S, which might be explained by P to S conversions.

Further performance improvement for IPI may require:

- Improvement of signal processing recipes to try and reduce the scatter in the measurements, particularly for noise detections.
- Improvement of the detector, to reduce the number of noise detections. For example, the data-adaptive, statistically optimal detector proposed by Kushnir *et al.* (1990) could be

applied. It detects signals based not only on power, but also on coherence properties.

- Inclusion of other measurements: "context information" (such as relative arrival time and amplitude), spectral shape, signal length, etc. Some can be derived from data stored in the database, others may require additional signal processing.

Comparison of IPI Using Two Different Polarization Recipes

The analysis performed so far has been based on polarization measurements obtained using a standard recipe that we will refer to as "recipe 1". In this section we compare our previous results for the April 1989 dataset at GAR to those obtained using another recipe ("recipe 2"), which had been found to optimize backazimuth estimation at station GAR (Riviere *et al.*, 1990). Our goal is to evaluate the effect of recipe on the measurements of polarization characteristics, and consequently, on the performance of Initial Phase Identification, and to investigate the feasibility of using one single recipe for both IPI and backazimuth estimation at GAR.

Description of Recipes 1 and 2

Recipes 1 and 2 differ in two ways: frequency bandwidth and time resolution:

- A set of three frequency bands are used for recipe 1, making it a wide-band recipe: 1-2 Hz, 2-4 Hz, 4-8 Hz. Recipe 2, on the other hand, uses the long-period narrow band 1-2 Hz.
- The time resolution is half for recipe 1: polarization is measured for a set of five 50% overlapping time windows, starting 2 sec before the onset time, and covering 6 sec of data. For recipe 2, five 50% overlapping time windows start 1 sec before the onset time and span 3 sec of data.

Comparison of Polarization Characteristics

- Teleseismic P: The results obtained for the two recipes differ in both the degree and type of polarization. The major difference is in rectilinearity: it is significantly higher, on average, for recipe 2 (mean of 0.96 instead of 0.85), as seen in the *top* part of Figure 7 (histograms for recipes 1 and 2 are displayed on the *left* and *right*, respectively). This explains the better backazimuth estimation obtained using recipe 2. Though dispersed, planarity is also higher, on average (0.49 instead of 0.34). There is slightly more vertical motion (H/V has a mean of 0.1 instead of 0.2), for recipe 2.
- Regional P: Differences are observed in SNR and polarization. Polarization SNR is lower, on average, for recipe 2 (with a mean of 7 instead of 21), although distributions of detection SNR are very similar. This is probably due to the fact that the higher frequencies of the signal are not included in the analysis. Again, rectilinearity (mean of 0.94 vs. 0.84)

and planarity (mean of 0.55 vs. 0.34) are higher, on average, for recipe 2. Incidence is slightly larger for recipe 2 (mean of 36° instead of 31°). Those results are preliminary, because of the small size of the sample.

- **Regional S:** Again, rectilinearity is higher for recipe 2 (mean of 0.88 vs. 0.63), as well as planarity (mean of 0.49 vs. 0.36). The direction of polarization is less distinct for recipe 2. For example, while the preferred orientation of the polarization plane is near-horizontal for recipe 1 (mean of short-axis incidence of 23°), it is less characteristic for recipe 2 (mean of 40°). As for Regional P, a larger sample is needed to reach definite conclusions.

- **Noise Detections:** Polarization SNR is slightly less, on average, for recipe 2 (mean of 1.7 vs. 2.5). Again, rectilinearity is higher for recipe 2 (mean of 0.89 vs. 0.78), as well as planarity (mean of 0.51 vs. 0.34). There are some differences in the direction of polarization: for example, a peak at 35° for the incidence of principal motion observed when recipe 1 is used is not present with recipe 2 (*bottom* of Fig. 7).

Initial Phase Identification

Initial Phase Identification was performed using the measurements obtained with recipe 2. Only ten signal measurements were used, since "polarization frequency" is now a constant (1.5 Hz, the center of the narrow band 1-2 Hz). The first eight Principal Components were included in the discriminant analysis. The performance for the two recipes is compared in Table 5.

Table 5: Comparison of Classification Performance for Two Polarization Recipes

Recipe	Tele P	Reg P	Reg S	Noise	All
1	78%	71%	86%	74%	76%
2	81%	59%	76%	63%	68%

When using recipe 2 the overall performance is degraded from 76% to 68%. For the regional phases and the noise detections, at least 10 percentage points are lost. These results are not surprising. Most of the signal information for Teleseismic P is in the 1-2 Hz band. Therefore, there is no degradation of IPI for this group. The other groups, however, have important polarization information above 2 Hz, which is lost when using recipe 2.

Other factors affecting polarization measurements, and consequently, phase identification, were identified in the previous subsection. We observed that polarization SNR is degraded for Regional P and noise. Also, rectilinearity becomes systematically high for all groups, making it less strong a discriminant between P, noise, and S. Also, more scatter was

observed in some measurements, such as polarization of Regional S.

Conclusions

- Polarization characteristics measured using recipes 1 and 2 are different. In particular, recipe 2 (long period, high time resolution) results in higher average rectilinearity and planarity for all detection groups; lower 3-C SNR for Regional P and noise (high-frequency detections); and some loss of directionality, especially for Regional S and noise. The increase in rectilinearity may be due to a combination of the use of a narrow frequency band and shorter time windows.
- The overall performance of Initial Phase Identification is lower for recipe 2, and is particularly low for the Regional P and noise groups, because of their polarization characteristics.

Although there may be some advantages in using shorter time windows, it appears that wide-band polarization analysis gives better results. This is due to the high-frequency content of regional phases and noise. This high-frequency content is documented, for example, by Khalturin and Rautian (1977) for Hindu-Kush earthquakes that constitute a significant part of the data (Riviere *et al.*, 1991). It is explained by a zone of anomalously low attenuation for this path to station GAR.

This study indicates that it may be difficult to optimize the polarization recipe for both Initial Phase Identification and backazimuth estimation. The former task requires a wide frequency band to use the important information contained in high-frequency signal and noise. The latter requires a narrow, long-period band to increase rectilinearity and reduce the effects of scattering, thus stabilizing backazimuth estimates. Because of those conflicting requirements, it appears preferable to perform those two tasks in separate steps.

Effect of Detection Threshold on Initial Phase Identification

The performance of Initial Phase Identification is compared for two different levels of detection threshold. We have described IPI performed on the GAR April 1989 dataset of event segments, with the detection threshold set at $\text{SNR} = 4$. We simulate a higher detection threshold (of $\text{SNR} = 5$) by extracting the subset of the data with detection $\text{SNR} > 5$, and redoing the analysis (i.e., determining a new discriminant function based on this subset). Table 6 compares the results obtained for these two values of the detection threshold.

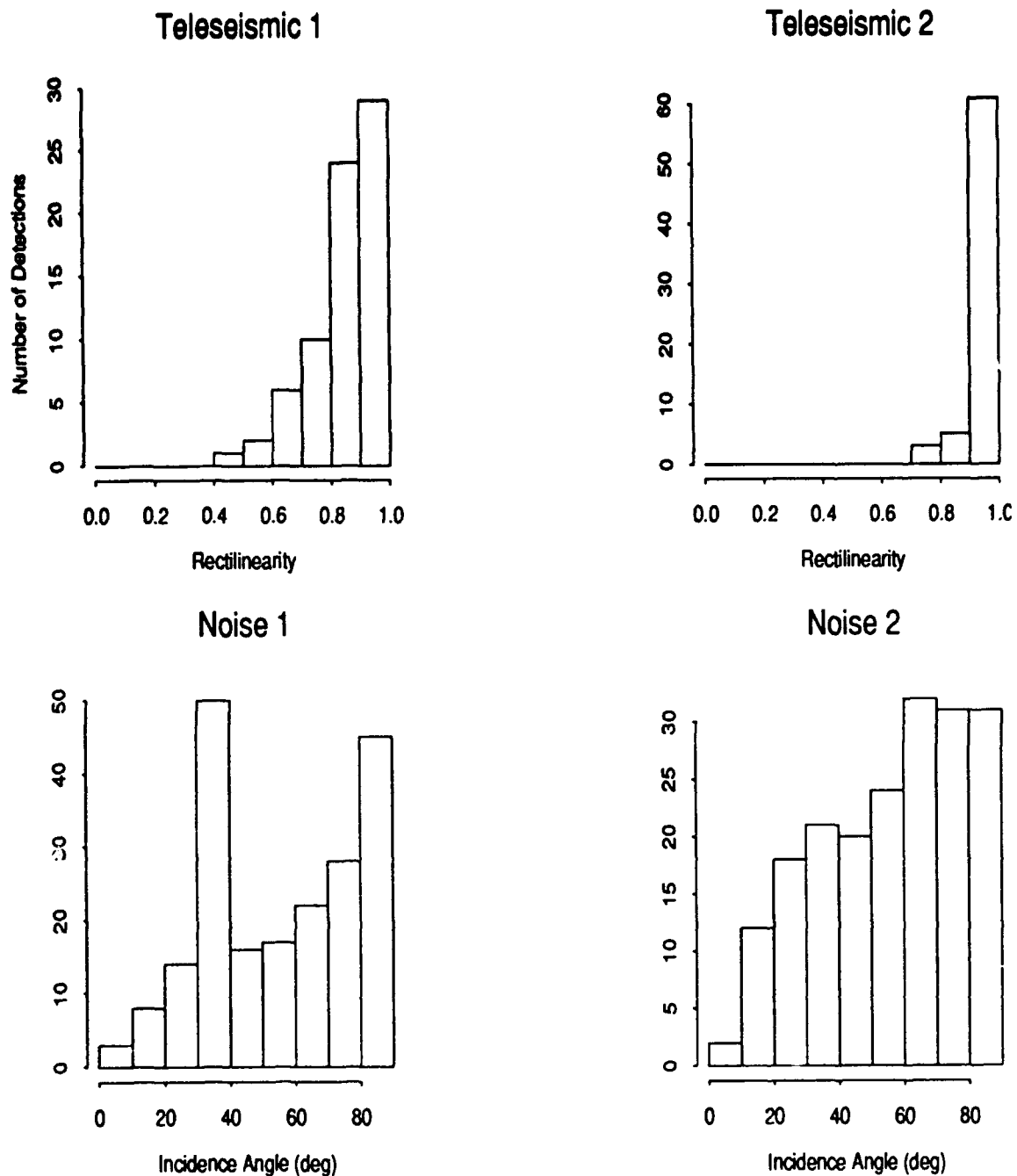


Figure 7: The distributions of a characteristic polarization attribute obtained using polarization recipes 1 and 2 are compared for the Teleseismic and noise detection groups. The April 1989 dataset for station GAR is used.

Also indicated in parentheses is the number of detections in each group.

Table 6: Comparison of Classification Performance for Two Detection Thresholds

Threshold	Tele P	Reg P	Reg S	Noise	All
4	78% (72)	71% (38)	86% (37)	74% (203)	76% (350)
5	73% (63)	69% (36)	86% (29)	77% (90)	76% (218)

62% of the original detections remain in the subset with $\text{SNR} > 5$. Although this subset includes 87% of seismic arrivals, only 44% of the noise detections are left. It would be interesting to repeat this study with even higher detection thresholds, but the current set of seismic arrivals is not large enough for this purpose. Table 6 shows that the overall performance of the discriminant analysis is the same with the threshold set at 4 or 5, in spite of some slight changes in the performance for Teleseismic P, noise, and Regional P.

Therefore, based on this limited dataset, it appears that increasing the detection threshold from 4 to 5 does not increase the success rate of Initial Phase Identification. It does, however, significantly reduce the number of noise detections to process, with the drawback that 13% of seismic arrivals are lost.

Study of Misidentification

It is also interesting to study misidentification of detections: that is, if a detection in a particular group is misidentified, which group it is more likely to have been assigned to. Table 7 gives the percentage of group membership assignments for each detection group. For example, the first line shows the percentage of actual Teleseismic P classified, from *left to right*, as Teleseismic P, Regional P, Regional S, and noise, respectively. Three cases are given: detection threshold of 4 (first line), detection threshold of 5 (second line), detection threshold of 4 but results for data with $\text{SNR} > 7$ only are shown (third line).

Table 7 shows:

- Incorrect classifications are not evenly distributed among all groups: Teleseismic P and Regional P, on one hand, Regional S and noise, on the other, are much more likely to be taken one for the other. Most misidentified Teleseismic P are classified as Regional P. Most misidentified Regional P are assigned to either the Teleseismic or the noise group. Almost all misidentified Regional S are classified as noise. Most misidentified noise detections are assigned to either the Teleseismic or, more commonly, the Regional S group.
- Increasing the detection threshold from 4 to 5 does not significantly change the results of misidentification.

Table 7: Misidentification Results

	Tele P	Reg P	Reg S	Noise
Tele P	78%	14%	4%	4%
	73%	24%	2%	2%
	81%	17%	2%	0%
Reg P	18%	71%	0%	11%
	14%	69%	0%	17%
	23%	77%	0%	0%
RegS	0%	3%	86%	11%
	0%	3%	86%	10%
	0%	5%	90%	5%
Noise	8%	1%	17%	74%
	8%	1%	14%	77%
	6%	6%	39%	50%

- A detection in the group {Teleseismic and Regional P} is much less likely to be incorrectly assigned to the group {Regional S and noise} for detections with SNR > 7.

In conclusion, for each detection group, there is one group to which the misidentified arrivals are most likely to be assigned: Regional P for Teleseismic P, and vice-versa, noise for Regional S, and vice-versa. The latter observation has important consequences for automated processing. For example, suppose a given detection has been identified as Teleseismic P. If further processing indicates a possible error in the identification, the next most likely identification will be Regional P, and the probability of any other identification will be low.

Conclusions and Discussion

A fourth group (noise detections) was added to the three groups of seismic arrivals (Teleseismic,

Regional P, and Regional S) used in a previous study (Riviere *et al.*, 1991) to perform Initial Phase Identification at the 3-C stations GAR, ARU and KIV. As a result, the success rate decreased, down to about 75% on average. A more detailed study was performed at station GAR, to gain insight on this relatively poor performance, and investigate ways to

improve it. A decrease in success rate can be expected as a new group is added. Furthermore, the noise detection group is characterized, in general, by average and strongly dispersed properties, except for low SNR. That makes it difficult to separate from the other groups, especially Regional S, whose success rate is particularly affected. Increasing the SNR detection threshold does not improve the performance, since, although it sharpens the characteristics of actual signals, it also results in more polarized noise detections.

A study of misidentification revealed that the procedure had difficulty separating Teleseismic from Regional P, and Regional S from noise, as one might expect, from both theoretical considerations and the observed properties of the various detection groups. This suggests an alternate method for performing phase identification at single 3-C stations: discriminate first between P and S, in the Initial Phase Identification step, then separate Teleseismic from Regional P, and Regional S from noise at a later stage of the processing. Such a method is being developed for implementation in the IMS (T. Sereno, personal communication). Other ways to improve IPI at 3-C stations are also currently being explored:

- Include context information as a predictor, in particular, the number of detections surrounding the current one, and their relative arrival times (Patnaik and Sereno, 1991);
- Use a Neural Network approach, instead of multivariate statistical analysis, to classify detections (Patnaik and Sereno, 1991);
- Use a hybrid method combining Discriminant Analysis and a Neural Network.

References

- Bache, T. C., S. R. Bratt, J. Wang, R. M. Fung, C. Kobryn, and J. W. Given (1990). The Intelligent Monitoring System, *Bull. Seism. Soc. Am.* 80, Part B, 1833-1851.
- Khalturin, V. I., T. G. Rautian, and P. Molnar (1977). The spectral content of Pamir-Hindu-Kush intermediate depth earthquakes: evidence for a high-Q zone in the upper mantle, *Journ. Geoph. Res.* 82, 2931-2943.
- Kushnir, A. F., V. M. Lapshin, V. I. Pinsky, and J. Fyen (1990). Statistically Optimal Event Detection Using Small Array Data, *Bull. Seism. Soc. Am.* 80, Part B, 1934-1950.
- Patnaik, G. B., and T. J. Sereno (1991). A Neural Network Approach to Initial Phase Identification From Three-Component Polarization Measurements, *Proceedings of 13th Annual PL/DARPA Seismic Research Symposium*, 8-10 October 1991, Keystone, Colorado. PL-TR-91-2208, ADA241325.
- Riviere-Barbier, F., A. Suteau-Henson, V. Z. Ryaboy, and J. A. Carter (1992). Analysis of 3-Component Data From IRIS Stations in the USSR, *Bull. Seism. Soc. Am.* 82, 192-220.

Confidence in Initial Phase Identification from Polarization at ARCESS and NORESS: a Comparison between Discriminant and Neural Network Methods

Anne Suteau-Henson

Introduction

In the Intelligent Monitoring System (IMS) the first step in identifying detections as seismic phases is Initial Phase Identification (IPI), as described in Bache *et al.* (1990). For array data, it consists in classifying detections as either Teleseismic, Regional P, Regional S, or noise. IPI for data from single 3-component ("3-C") stations has been investigated in previous studies. Suteau-Henson (1991) shows how Regional P (Pn and Pg) can be distinguished from Regional S (Sn and Lg) at NORESS and ARCESS, using multivariate discriminant analysis based on polarization measurements. Riviere *et al.* (1991) apply the same technique to separate Teleseismic P, Regional P, and Regional S at IRIS/IDA stations in the USSR (GAR, ARU, KIV), using both polarization and frequency. This study was extended to include noise detections (this report, Section 1).

A Neural Network (NN) approach was proposed by Patnaik & Sereno (1991) to discriminate between P and S-type phases at ARCESS and NORESS, based on 3-C measurements of polarization and frequency. An extensive dataset extracted from the IMS database was used. Discriminant Analysis (DA) based on the same measurements was applied to the same data, and the performance results were compared. Similar results were obtained, with a slight advantage of the NN technique, especially for S phases.

In this study we compare those results in more detail, by examining the confidence in the initial phase identification obtained with the two methods. Our goal is to investigate the feasibility of combining the two (for example, in a "voting scheme"), to improve the performance of the classification. First, we investigate the confidence obtained using DA. Then, we compare the subsets of detections misidentified by either method ("failure sets"), to determine how much they overlap. A small overlap would increase the chance of a combination of both methods resulting in better performance. Finally, we compare the confidence in phase identification for the subsets of arrivals for which only one method was successful, in an attempt to evaluate the usefulness of this confidence in a voting scheme.

Confidence in Phase Identification From Discriminant Analysis

In this section the confidence in Initial Phase Identification at ARCESS and at NORESS

from Discriminant Analysis is studied for P- and S-type phases. Three different training and testing sets were used for each classification experiment (Patnaik & Sereno, 1991), and the results will be shown for selected testing sets. Similar results are obtained for the others, as well as for the training sets. As a measure of confidence in the identification we use the probability (in percent) that a given arrival belongs to the phase group it was assigned to. This probability is a function of the generalized distance from the discriminant score of the arrival to the centroid of the population for each phase group (Suteau-Henson, 1991).

Figure 8a displays the probability of an arrival being a P-type phase ("P-probability") for the first testing set at ARCESS. Note that the probability of an arrival being an S is simply 100 minus P-probability in percent. The first vertical line separates analyst-identified P arrivals (*left*) from S arrivals (*right*). The horizontal line, corresponding to 50% probability, separates correctly from incorrectly identified arrivals; i.e., actual P with less than 50% and actual S with more than 50% P-probability were misidentified. The confidence is higher, on average, for correctly identified P than for correctly identified S. Misidentified P have a near random distribution of P-probability below 50%. For S phases, however, there is a concentration of P-probability around 50%, corresponding to S phases with weak characteristics.

A subset of the data of particular interest is that with 3-C SNR > 2 (Patnaik & Sereno, 1991). Figure 8b shows the P-probability of this subset for the first testing sample at ARCESS. For P phases the confidence of phase identification is higher, on average, than in the case where arrivals of all SNRs are included (Figure 8a).

Similar results are obtained at NORESS, as illustrated in Figures 8c and 8d, that display the P-probability for the first testing set at NORESS, with all SNRs included, and for SNR > 2, respectively. However, the confidence for correctly identified arrivals is higher, on average, at NORESS than at ARCESS, as can be seen by comparing with Figures 8a and 8b.

Figure 8 indicates that a subset of S arrivals has an unusually high failure rate. This is further investigated in Figure 9, where the P-probability is plotted against the "arid" (arrival identification number in the IMS database) for the actual S arrivals in the first testing set at ARCESS. A group of arrivals between arid 340000 and 410000 shows this anomalous distribution. They were recorded during the time period August 22 - September 3, 1990, at the start of signal-processing operation at NORSAR (August 22). Therefore, we suspect that these are "bad" data, reflecting an operational problem that was corrected later on.

In summary, this study of the confidence on Initial Phase Identification (measured as the probability of membership in the most likely phase group) for P- and S-type phases, at

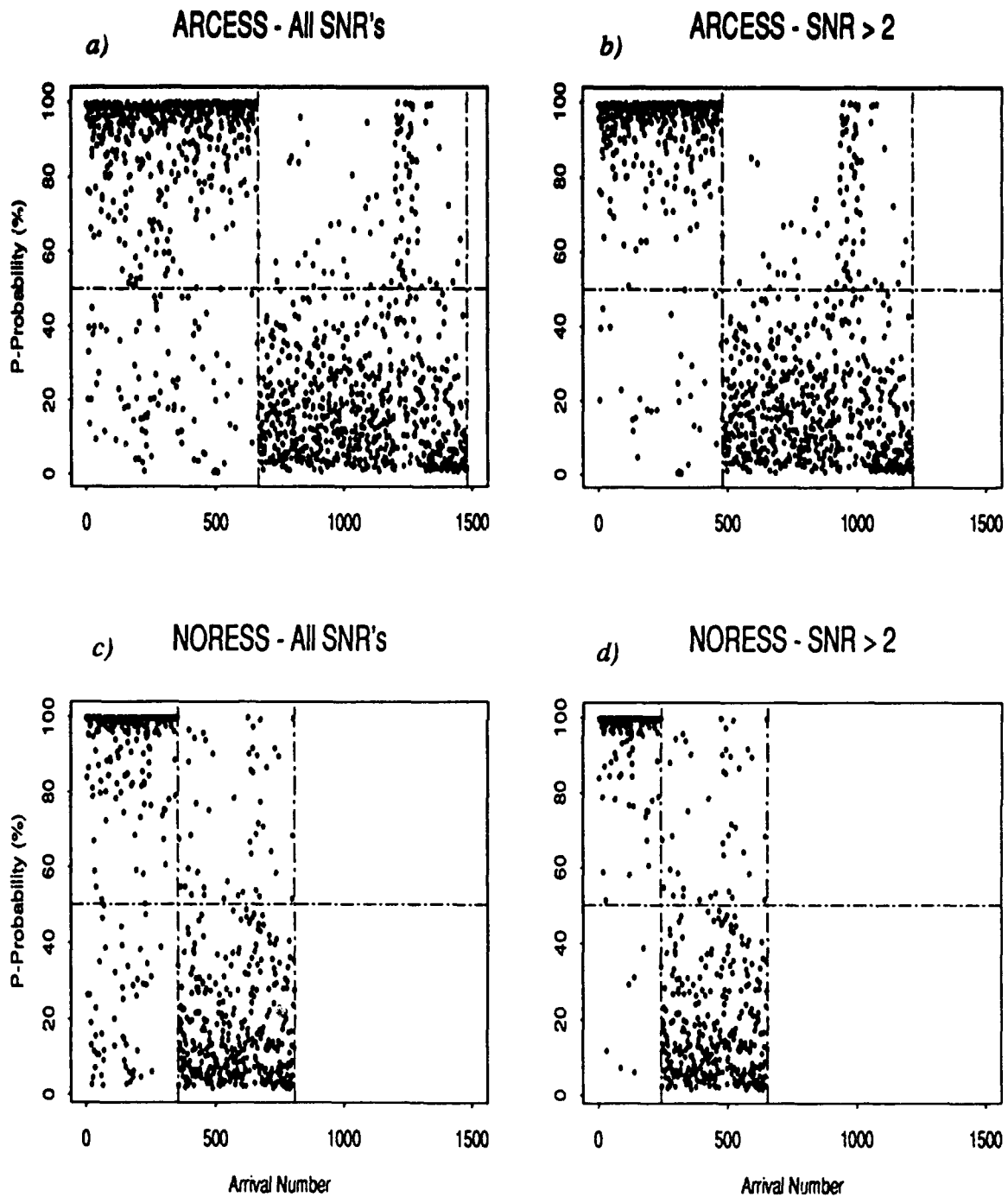


Figure 8: The probability (in percent) of an arrival being of P-type is plotted, for those arrivals in the first testing set that were identified by the analyst as either P or S (*left and right* of the first vertical line, respectively), for various subsets of the data. The horizontal scale is identical for all plots, to facilitate the comparison.

S At ARCESS - All SNR's

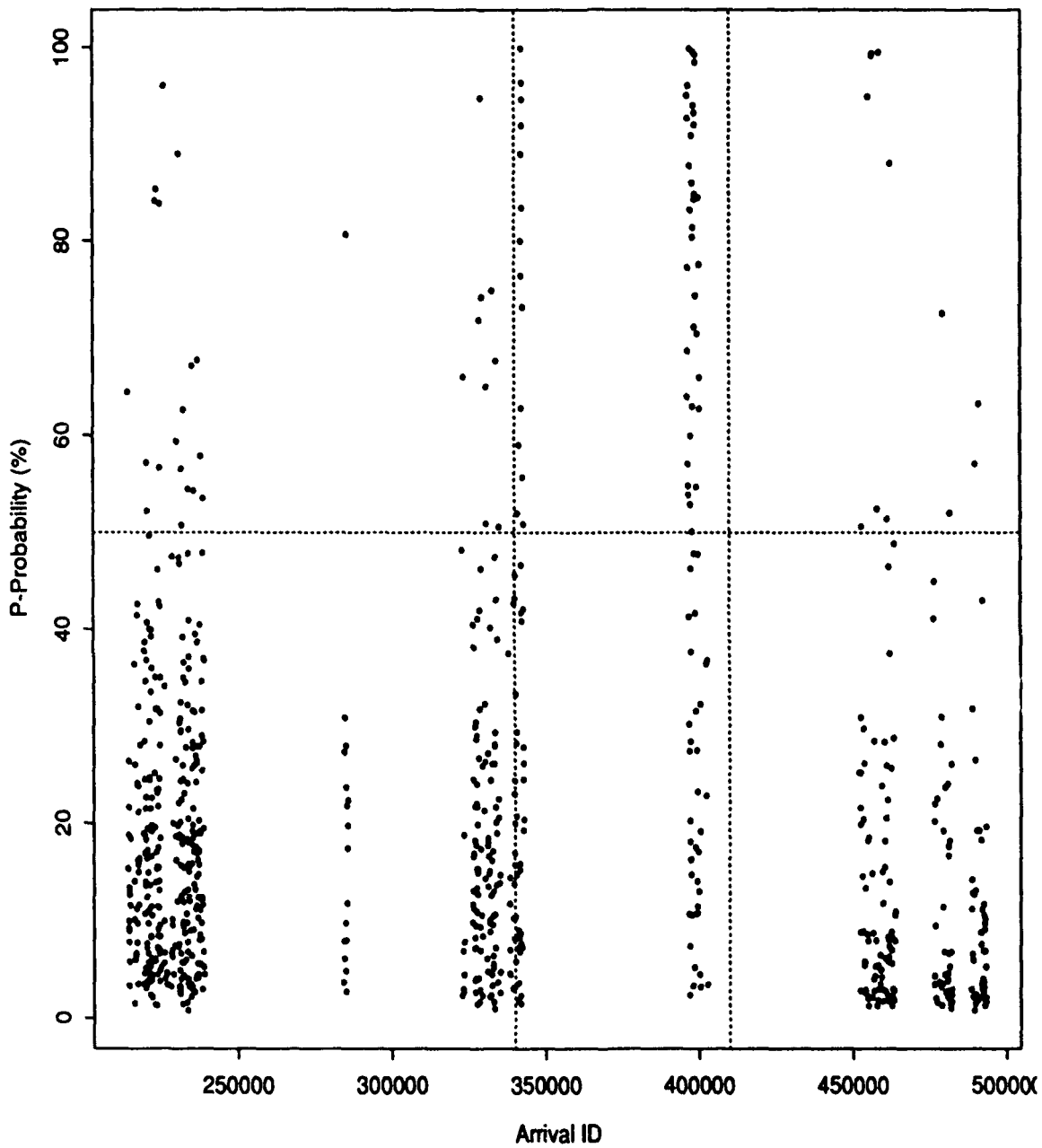


Figure 9: The probability (in percent) of an arrival being of P-type is plotted for those arrivals in the first testing set at ARCESS that were identified as S phases by the analyst. A low "P-probability" means a high confidence in the identification. The subset of arrivals between the dotted vertical lines has an anomalous distribution.

ARCESS and NORESS, shows that:

- The confidence is higher, on average, for correctly identified P-type phases than for correctly identified S-type phases.
- The confidence increases for P-type phases with $\text{SNR} > 2$.
- The confidence for correctly identified arrivals is higher, on average, at NORESS than at ARCESS.
- Because of the scatter in the distribution of confidence for S-type phases at ARCESS, some S phases are misidentified for lack of distinctive characteristics (their probability of membership in either phase group is around 50%).
- The confidence in S-type phase identification is anomalously low for a particular time period, and this appears to be due to operational problems. The overall confidence distribution is degraded as a result.

Comparison of Discriminant and Neural-Network Failures

The sets of failures of Initial Phase Identification at ARCESS and at NORESS are compared for the two methods: Discriminant Analysis (DA) and Neural Network (NN). Table 8 gives the number of actual P and S arrivals: analyzed, correctly identified by both methods, misidentified by both, and misidentified by one only. The amount of overlap for the failure sets (i.e., the ratio of the number of arrivals for which both methods failed to the number of arrivals for which at least one method failed) is 56% for P and 22% for S at ARCESS, and 62% for P and 21% for S at NORESS. The smaller overlap for S phases reflects the significantly larger number of DA failures.

Table 8: Comparison of DA and NN Failure Sets

Subset	ARCESS P	ARCESS S	NORESS P	NORESS S
All Arrivals	1996	2446	1064	1359
Hits	1688	2127	885	1189
Both Failed	171	69	111	36
DA Failures	103	211	32	111
NN Failures	34	39	36	23

Figures 10 and 11 show the P-probability from DA for various subsets of the data, at ARCESS and NORESS, respectively. Figure 12 displays boxplots of the discriminant dis-

ARCESS

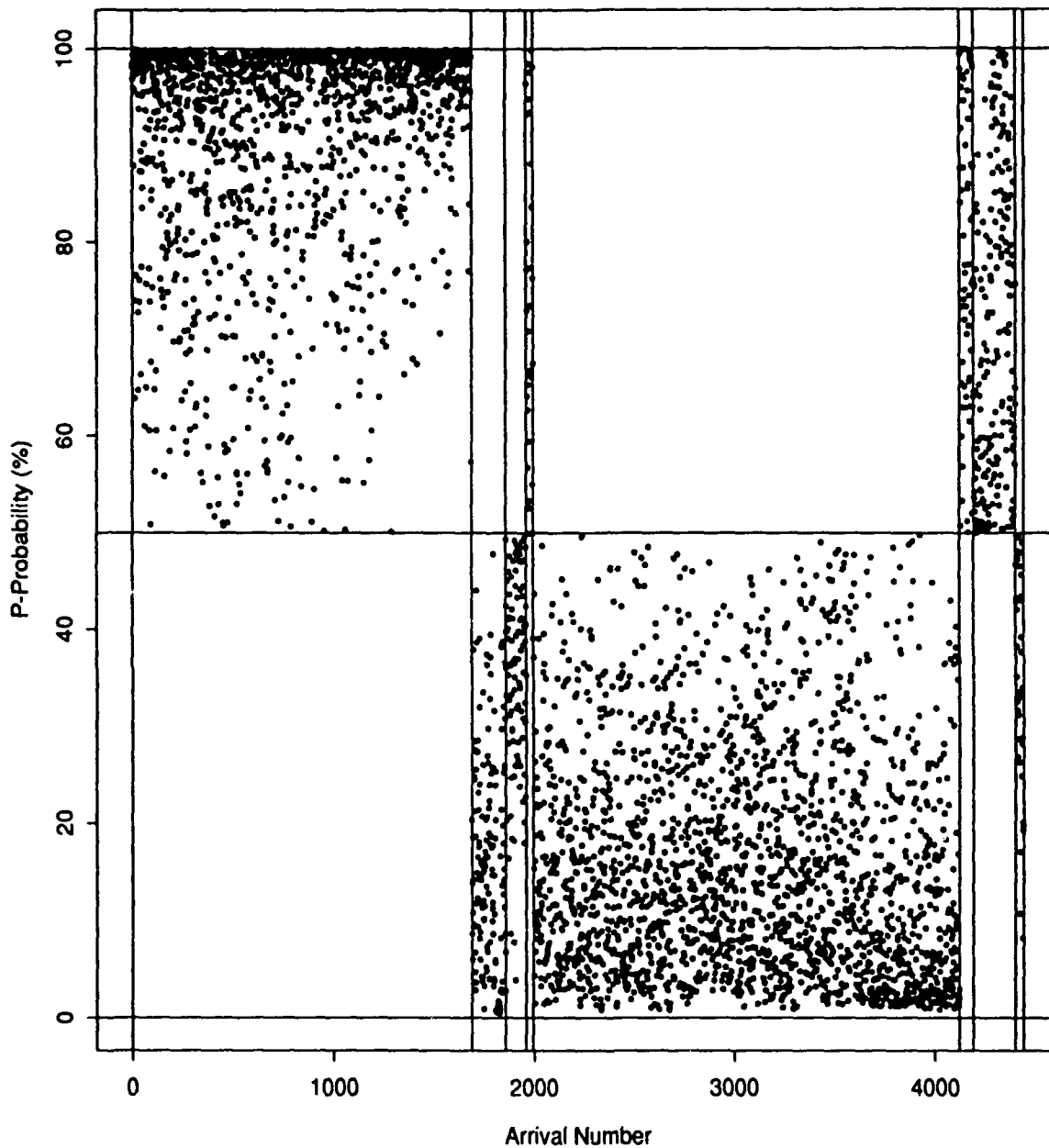


Figure 10: The probability (in percent) of an arrival being of P-type is plotted for all arrivals in the first testing set at ARCESS. Eight subsets of the data are shown. From *left to right*: P correctly identified by both the Discriminant Analysis (DA) and Neural Network (NN) methods, P misidentified by both, P misidentified by DA, P misidentified by NN, S correctly identified by both, S misidentified by both, S misidentified by DA, S misidentified by NN.

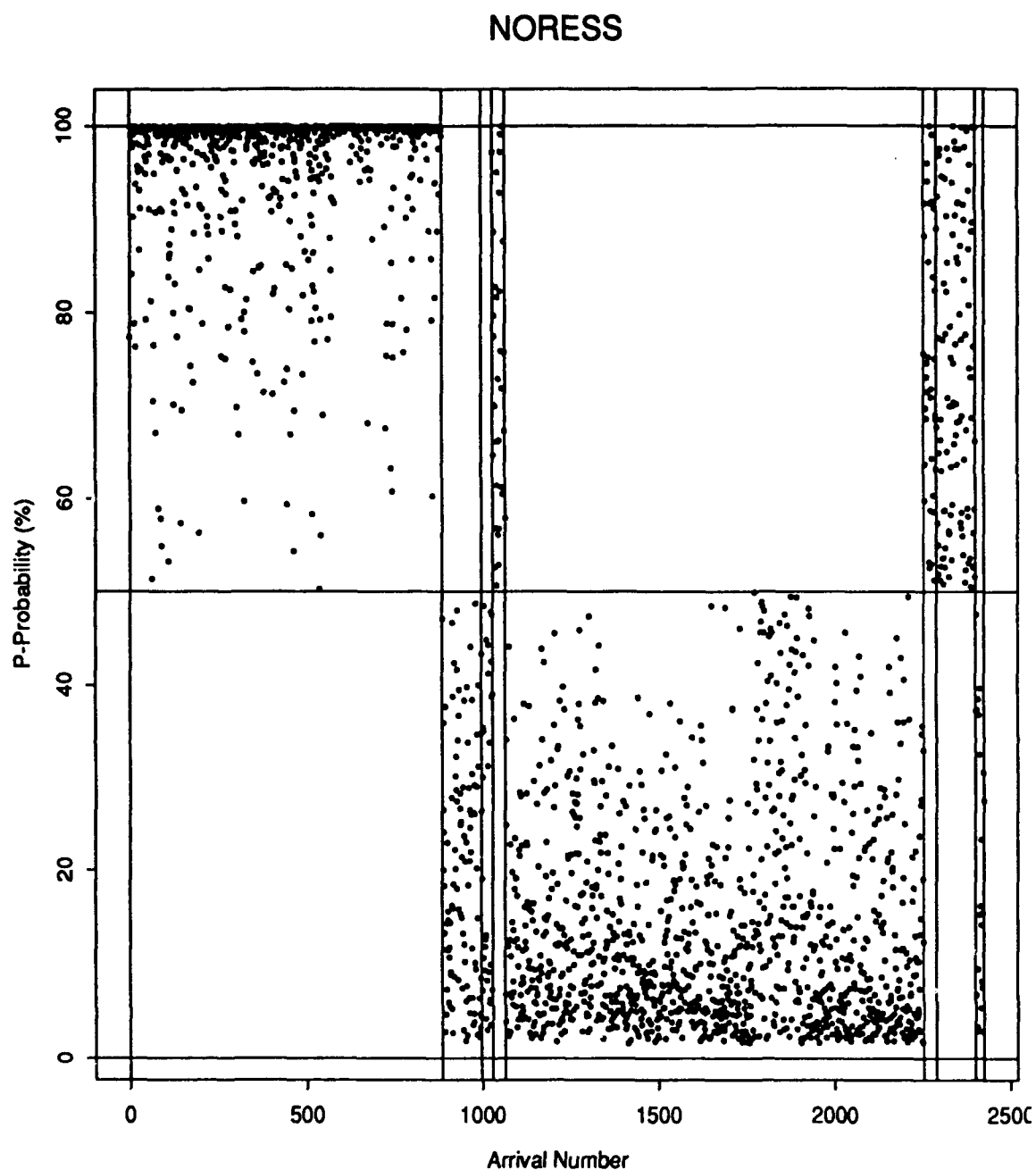


Figure 11: The probability (in percent) of an arrival being of P-type is plotted for all arrivals in the first testing set at NORESS. Eight subsets of the data are shown. From left to right: P correctly identified by both the Discriminant Analysis (DA) and Neural Network (NN) methods, P misidentified by both, P misidentified by DA, P misidentified by NN, S correctly identified by both, S misidentified by both, S misidentified by DA, S misidentified by NN.

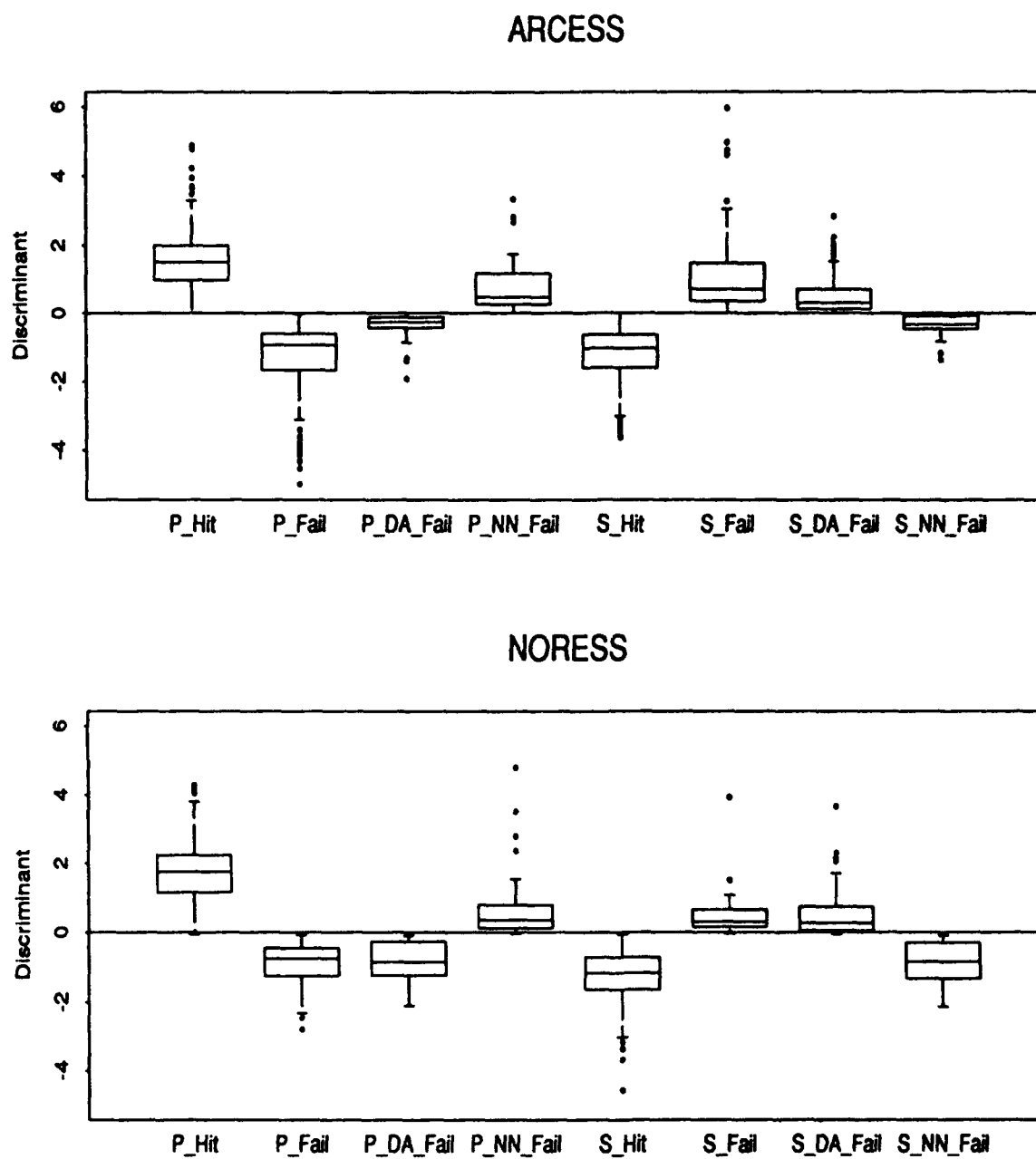


Figure 12: Boxplots show the distributions of the discriminant variable for eight subsets of the data in the first testing set (see text for details).

tribution for the same eight subsets. From *left* to *right* are shown:

- Actual P correctly identified by both methods ("P_Hit");
- Actual P misidentified by both ("P_Fail");
- Actual P misidentified by DA only ("P_DA_Fail");
- Actual P misidentified by NN only ("P_NN_Fail");
- Actual S correctly identified by both methods ("S_Hit");
- Actual S misidentified by both ("S_Fail");
- Actual S misidentified by DA only ("S_DA_Fail");
- Actual S misidentified by NN only ("S_NN_Fail");

Of particular interest are the subsets where NN and DA conflict, i.e., NN identified an arrival as P and DA identified it as S, and vice-versa. Those are the failures that could potentially be remedied by a voting scheme. Therefore, we further study the following two cases:

- Identification is P from NN and S from DA;
- Identification is S from NN and P from DA.

In each case, the correct identification could be either P or S. Therefore, the following subsets are compared:

- Actual S misidentified by NN and actual P misidentified by DA (case 1);
- Actual P misidentified by NN and actual S misidentified by DA (case 2);

The following measurements are compared for those subsets: polarization attributes (center frequency, rectilinearity, horizontal-to-vertical power ratio, incidence, short-axis incidence); the discriminant variable; the P-probability; the detection frequency, the detection-beam type (horizontal or vertical), and the detection SNR (STA/LTA); the 3-C SNR. As seen in Figures 10, 11 and 12, the distributions of P-probability and discriminant for the two groups in case 1 ("P_DA_Fail" and "S_NN_Fail") show significant overlap, and the same applies to the two groups in case 2 ("P_NN_Fail" and "S_DA_Fail"). Those groups are not easily separated based solely on the original set of measurements used for phase identification and the variables derived from them. Therefore, we investigated whether additional independent information would help, such as other measurements stored in the IMS database tables APMA and ARRIVAL.

For example, 3-C SNR shows somewhat different distributions in each case for the two subsets at ARCESS, as seen in Figure 13. For case 1 (*top*), "P_DA_Fail" is displayed to the *left* and "S_NN_Fail" to the *right* of the vertical line. For case 2 (*middle*), "S_DA_Fail" is displayed to the *left* and "P_NN_Fail" to the *right*. In both cases, the two groups are partially separated by an SNR threshold of about 2 (horizontal line). Arrivals with $SNR < 2$ are usually P, while arrivals with $SNR > 2$ are usually S, although there are some outliers. Unfortunately, as mentioned above, the S-phase data set is contaminated by apparently incorrect polarization measurements for the period from August 22 to September 3, 1990, corresponding to the start of signal-processing operation at NORSAR. This affects, in particular, the distribution of "S_DA_Fail", as illustrated at the *bottom* of Figure 13 that shows the tangent of incidence angle for case 2. Note the anomaly between arrival number 79 and 188 corresponding to this time period. Similar results are obtained at NORESS (Figure 14).

Measurements from the ARRIVAL IMS database table can further help separate the two groups in each case. This is illustrated in Figure 15 that shows boxplots of the distributions for the detection frequency (*left*) and the detection SNR (*right*) for the four groups. It shows that misidentified P arrivals tend to have higher detection frequency and higher detection SNR (> 4.5) than misidentified S. Also, 97% (94%) of P misidentified by NN and 97% (100%) of P misidentified by DA are detected on a vertical beam, compared to only 79% (91%) of S misidentified by NN and 69% (80%) of S misidentified by DA, at ARCESS and NORESS, respectively.

Finally, the geographical distribution of events associated to the various failure subsets was studied and the results are displayed in Figure 16 for ARCESS and Figure 17 for NORESS. The "bad" data have been removed, since they correspond to a particular time period rather than location. Although no strong separation exists between the various groups, the following observations can be made:

- At ARCESS, the S misidentified by NN tend to be from near-regional events (in the Kola Peninsula and Northern Sweden). The P misidentified by DA are much more dispersed.
- At ARCESS, the P misidentified by NN are again mostly from near-regional events. The S misidentified by DA are more dispersed, and a trend along a N-S azimuth is observed, suggesting a possible azimuthal dependence.
- At NORESS, much dispersion is observed for both "P_DA_Fail" and "S_NN_Fail". NN tends to fail for underwater explosions, especially in the Baltic Sea, and for Estonia mines. DA tends to fail for events from Western Norway, the Kola Peninsula, Finland, and Estonia.

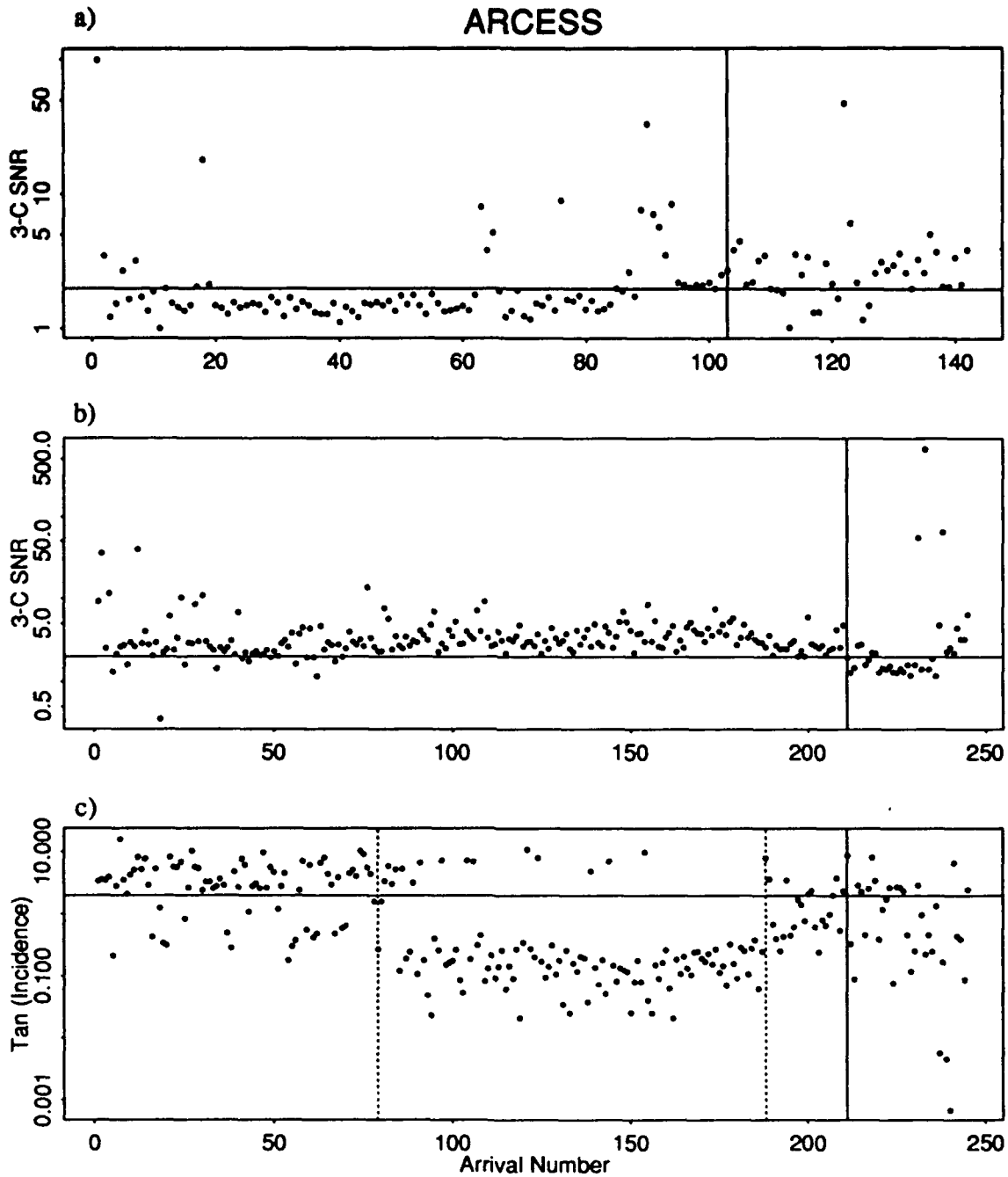


Figure 13: a): the 3-component SNR is plotted for the subsets "P_DA_Fail" and "S_NN_Fail" at ARCESS (*left* and *right* of the solid vertical line, respectively); b) same as a), but for the subsets "S_DA_Fail" (*left*) and "P_NN_Fail" (*right*); c): the tangent of incidence angle is plotted for the subsets "S_DA_Fail" (*left*) and "P_NN_Fail" (*right*); note the anomalous distribu-

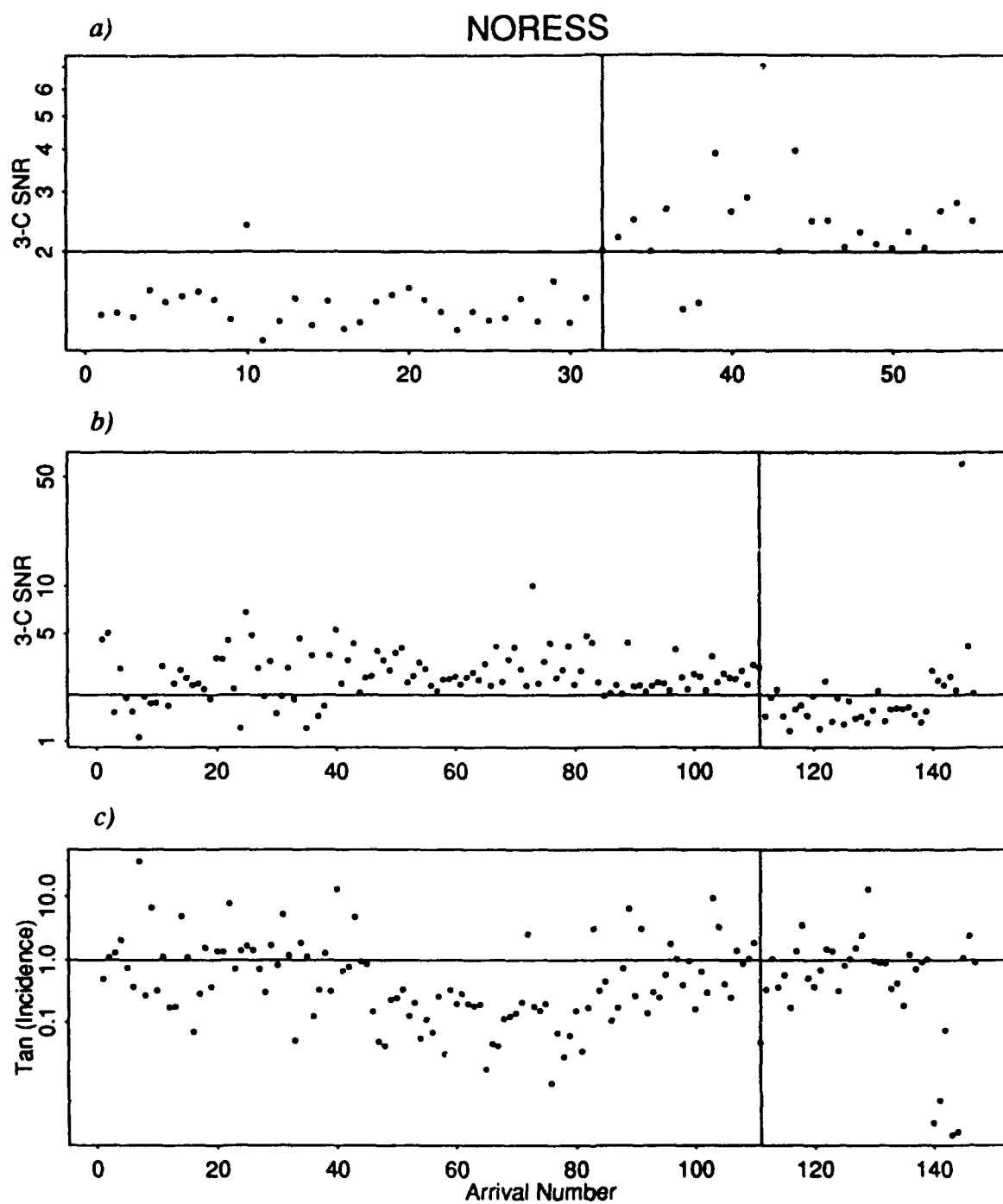


Figure 14: a): the 3-component SNR is plotted for the subsets "P_DA_Fail" and "S_NN_Fail" at NORESS (*left* and *right* of the solid vertical line, respectively); b) same as a), but for the subsets "S_DA_Fail" (*left*) and "P_NN_Fail" (*right*); c): the tangent of incidence angle is plotted for the subsets "S_DA_Fail" (*left*) and "P_NN_Fail" (*right*).

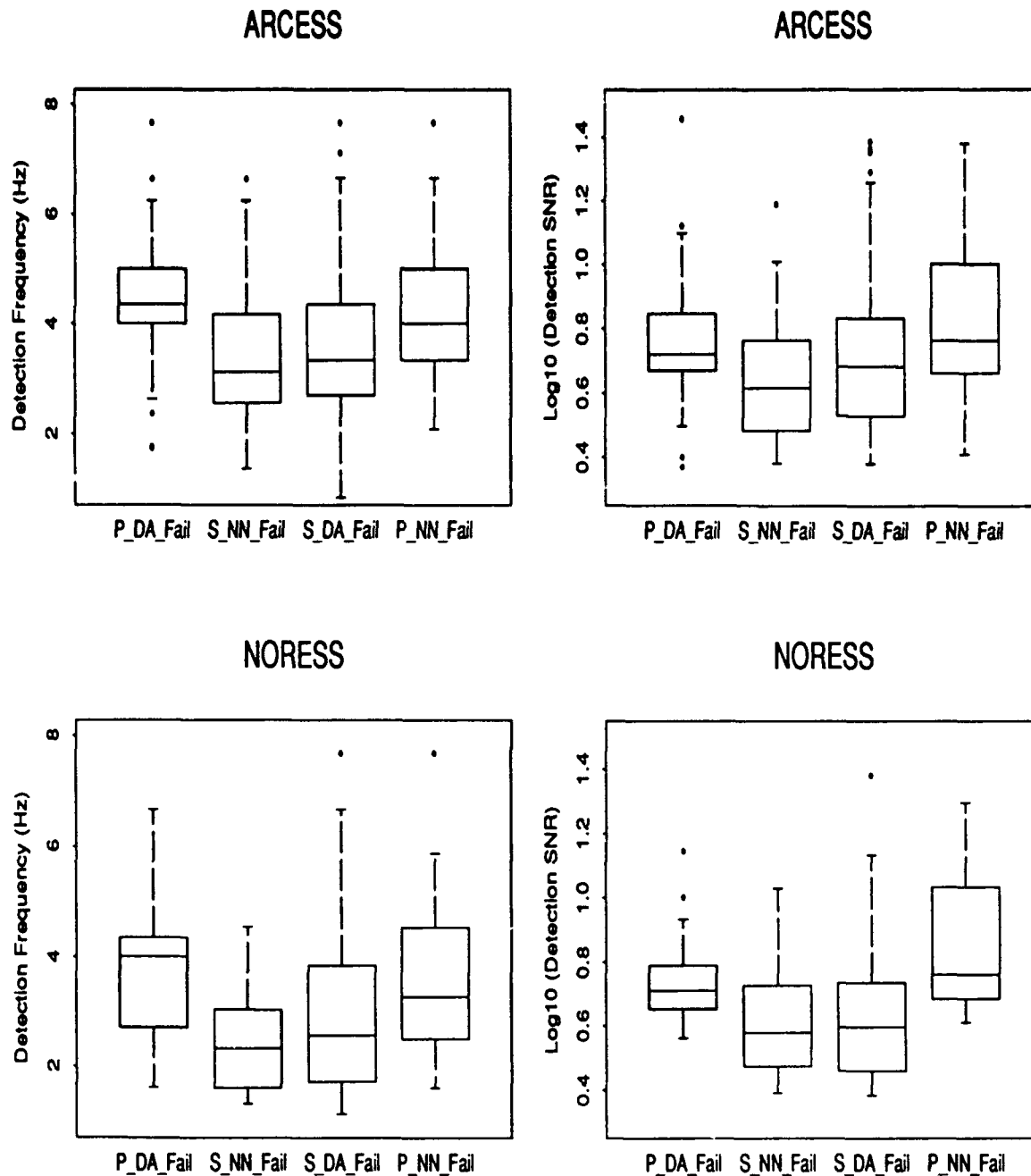


Figure 15: Boxplots show the distributions of dominant frequency (*left*) and SNR (*right*) of the “best” detection beam for the four data subsets where initial phase identification from Discriminant Analysis (DA) and Neural Network (NN) differ.

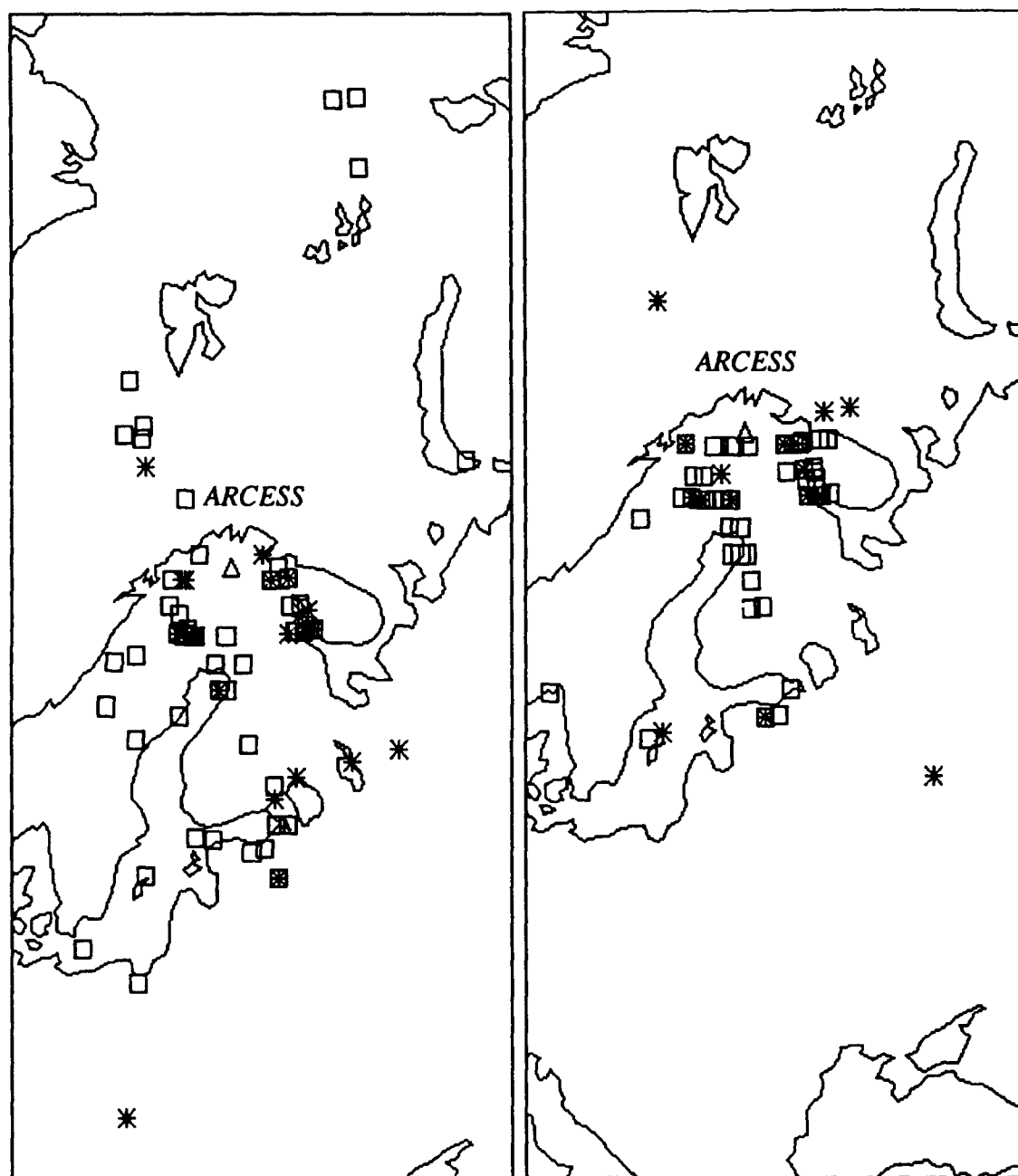


Figure 16: Maps show the locations of the events corresponding to various failure subsets at ARCESS. A triangle indicates the station location. *Left*: actual P misidentified by DA ("P_DA_Fail", *squares*) and actual S misidentified by NN ("S_NN_Fail", *asterisks*). *Right*: actual S misidentified by DA ("S_DA_Fail", *squares*) and actual P misidentified by NN ("P_NN_Fail", *asterisks*).

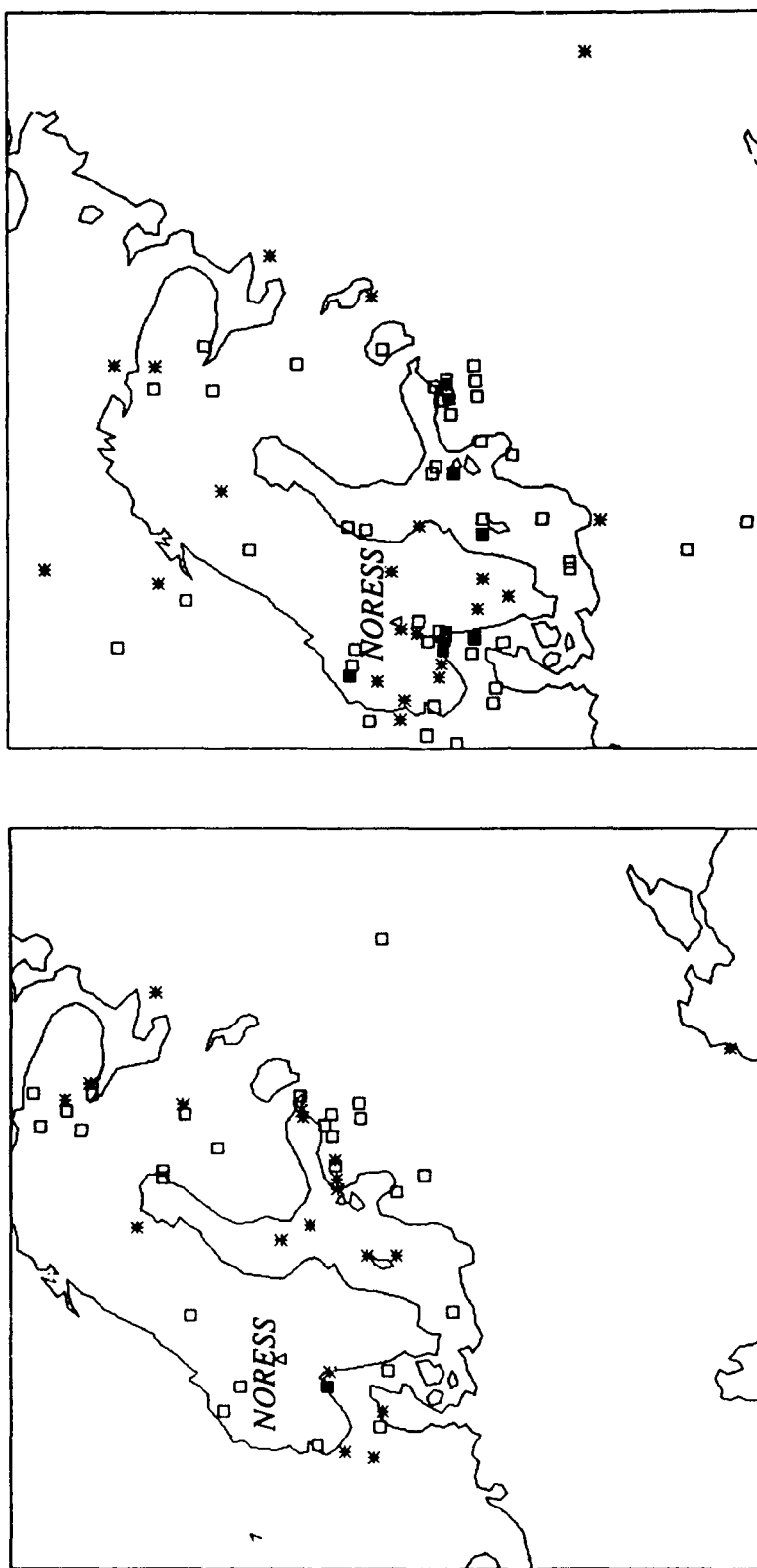


Figure 17: Maps show the locations of the events corresponding to various failure subsets at NORESS. A triangle indicates the station location. *Left*: actual P misidentified by DA ("P_DA_Fail", squares) and actual S misidentified by NN ("S_NN_Fail", asterisks). *Right*: actual S misidentified by DA ("S_DA_Fail", squares) and actual P misidentified by NN ("P_NN_Fail", asterisks).

- At NORESS, S misidentified by DA are mostly from offshore events and from Estonia mines. P misidentified by NN are concentrated in Western and Southern Norway.

In summary,

- The amount of overlap between the NN and DA failure sets is 56% for P and 22% for S at ARCESS, and 62% for P and 21% for S at NORESS. Since the failure sets do not completely overlap, combining results from both methods may increase the success rate.
- Investigation of the cases where NN and DA conflict in their identification indicates that additional information, such as 3-C SNR, and detection frequency, beam type and SNR (from the ARRIVAL table) could further help separate actual P from actual S arrivals.
- Thirteen days of spurious data contaminate the set of S arrivals. Their polarization attributes are such that DA identifies them as P. This results in poorer performance of S-phase identification from DA, and smaller overlap between the NN and DA failure sets for S than for P.
- The departure from normality due to the inclusion of these "bad data" has a more negative effect on the DA than on the NN performance.
- The geographical distributions of the various failure subsets do not indicate any clear separation, although some trends can be observed.

Comparison of Discriminant and Neural-Network Confidence for Failures

Both the DA and NN techniques provide a measure of "confidence" on the identification of each arrival as a P or an S. For DA, this is the probability that an arrival is a P or an S, as described above. For NN, a confidence factor can be obtained empirically from the node activation value (Patnaik & Sereno, 1991). We compare the probability from DA and the confidence factor from NN for the failure sets that were studied in the previous subsection. The subsets of interest are those for which the identifications from NN and DA differ.

In Figure 18 the DA confidence is plotted against the NN confidence, for the subsets "P_DA_Fail", "S_NN_Fail", "S_DA_Fail", and "P_NN_Fail", at ARCESS and NORESS. Note that There are some striking differences in the distributions of NN confidence at ARCESS and NORESS (Patnaik & Sereno, 1991). One would expect the NN or DA confidence to be relatively high when the identification is correct, and low in the case of misidentification. However, inspection of the data indicates this is not necessarily so. At ARCESS, phases misidentified by DA tend to have low DA confidence, but not at NORESS. On the other hand, arrivals correctly identified by DA do not have particularly high

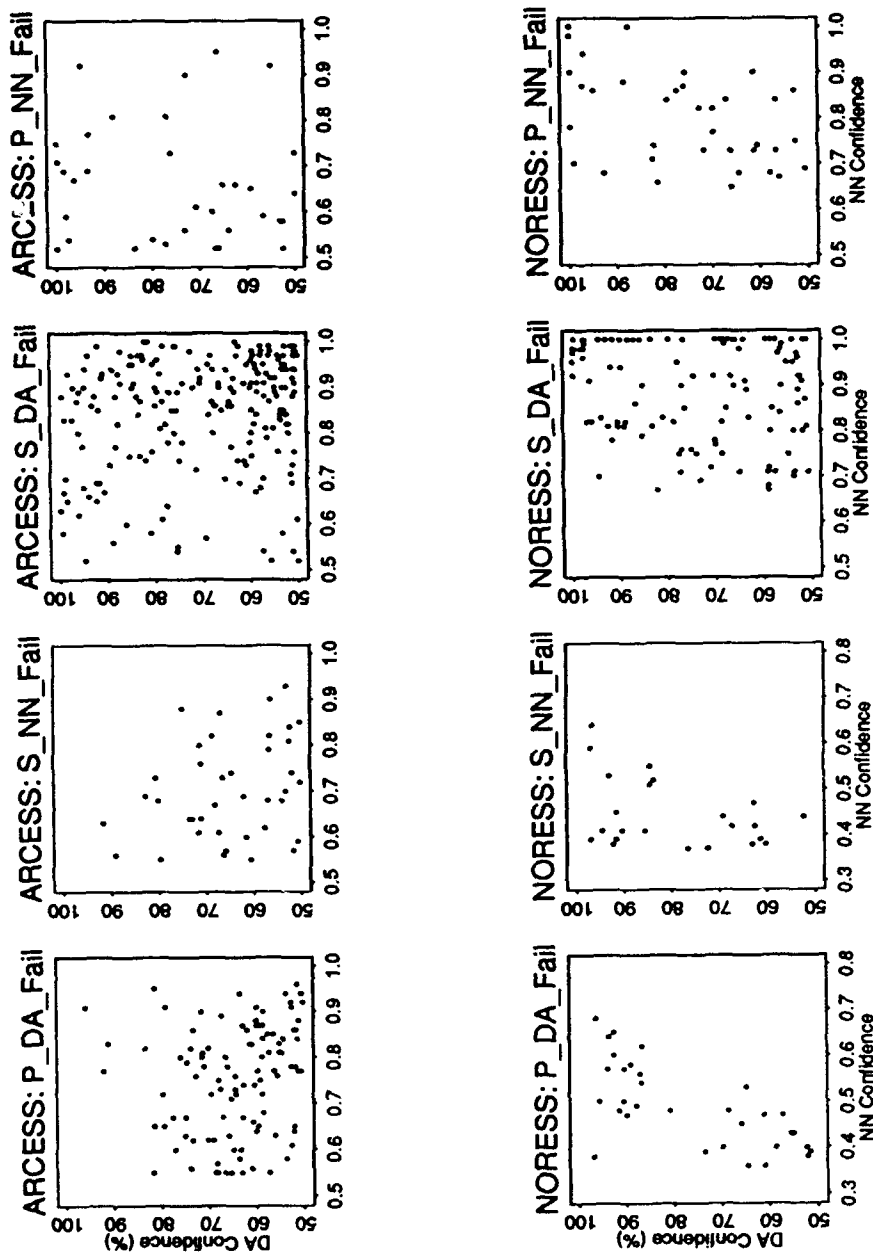


Figure 18: The confidence in the phase identification from Discriminant Analysis (DA) is plotted against the confidence from the Neural Network (NN) for the subsets of the data where one of the two methods failed (see text for details).

confidence. The NN confidence of arrivals correctly identified by NN tends to be high for S but not for P. The NN confidence of P misidentified by NN is low at ARCESS, but not at NORESS.

In a previous subsection we identified a time period (from August 22 to September 3, 1990) during which the polarization measurements appeared to be in error. This particularly affected the subsets of S arrivals misidentified by DA ("S_DA_Fail"). The effect of these bad data on the confidence distributions is shown in Figure 19 (where "good" refers to the subsets from which the bad data have been removed). At both arrays the NN confidence is high for all data, indicating the NN was confident in identifying these arrivals as S. The DA confidence tends to be low for the "good" subsets, as expected for failures, but is close to random for the bad data. Therefore, the bad data contaminate the distributions of DA confidence.

Figure 20 is similar to Figure 18, except the data from August 22 to September 3, 1990 have been removed. Some improvement is observed, especially at ARCESS, where "S_DA_Fail" now tends to have high NN and low DA confidence, as expected. However, there is still much scatter, caused by arrivals whose NN and/or DA confidence departs from what would be expected based on the identification results.

Conclusions and Discussion

This detailed comparison of the performance of Initial Phase Identification using a classical linear discriminant and a neural network indicates the following:

- There is not much overlap between the failure sets from the two methods: it is on the order of 60% for P and 20% for S. Their geographical distribution also differs.
- The small overlap for S is partly explained by an anomalous distribution of some of the S data, that apparently degrades the DA performance without significantly affecting the NN results. We propose to perform this comparison again on a dataset "cleaned" from the anomalous data.
- A detailed study of the failure sets indicates that their size could have been reduced if more measurements had been used, such as SNR or dominant frequency of the "best" detection beam. Patnaik & Sereno (1991) also show that "context information", such as relative arrival times of detections, contributes to improving the performance of Initial Phase Identification.
- A comparison of the DA and NN confidence for the various failure sets indicates in some cases a tendency for misidentified arrivals to have low confidence and for correctly identified arrivals to have high confidence. Such a property could be used to devise a "voting

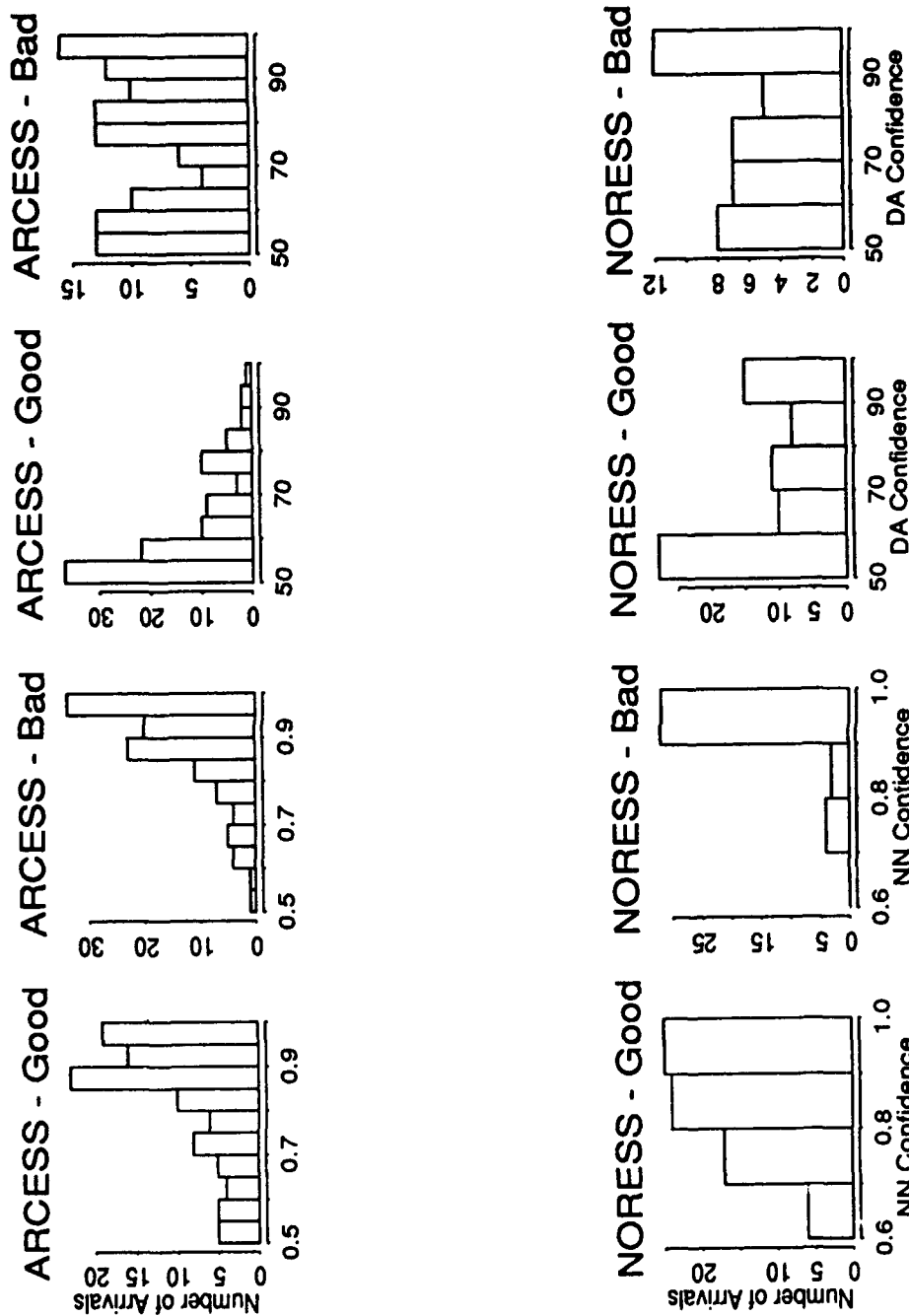


Figure 19: Histograms are plotted for the distributions of confidence from Discriminant Analysis (DA) and Neural Network (NN), for actual S-type phases misidentified by the DA method. "Bad" refers to the subsets of arrivals from the period August 22 to September 3, 1990, with anomalous polarization measurements. The remaining arrivals form the "good" subsets.

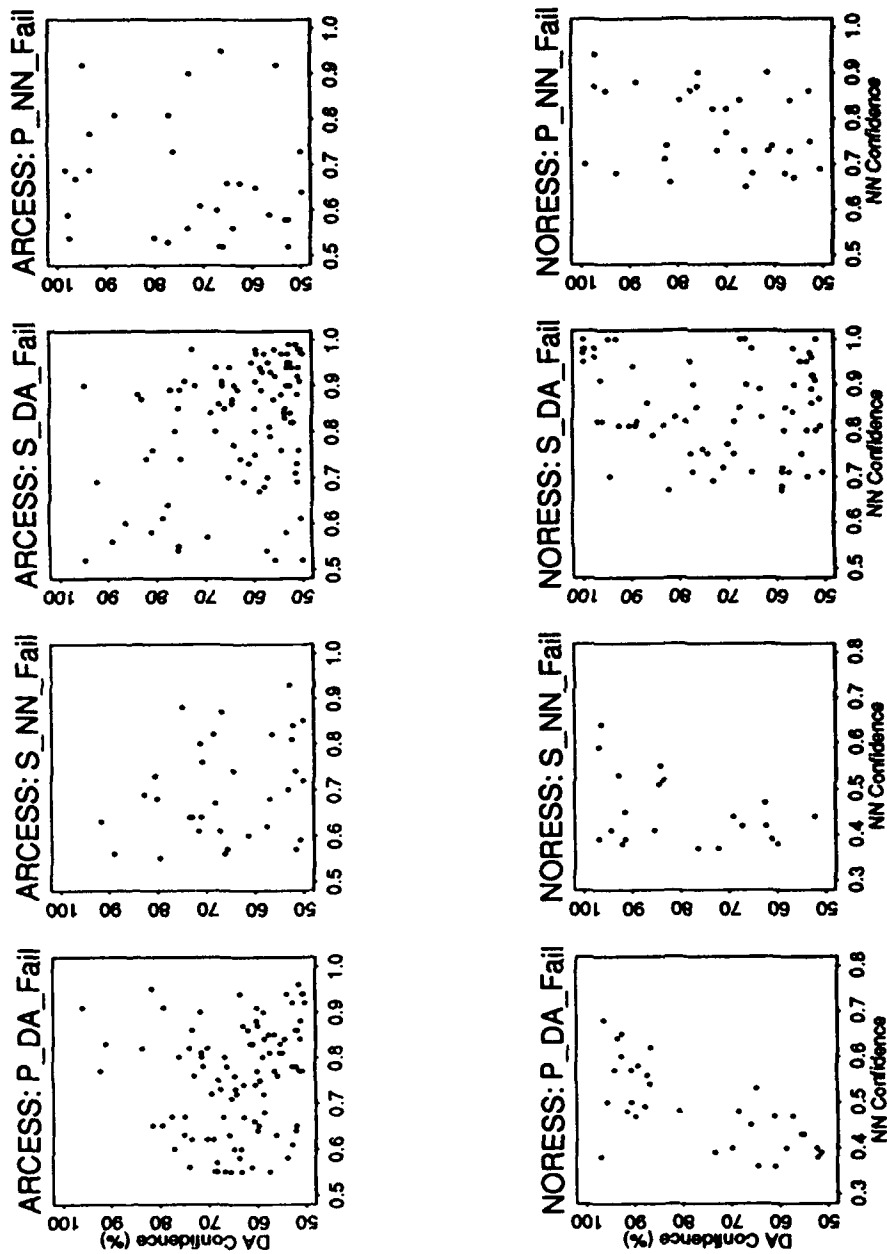


Figure 20: Same as Figure 18, except the "bad" data points have been removed.

scheme" that would help decide on the correct identification in the cases where the two methods conflict. An alternate approach would be to use the DA results as additional inputs to a neural network. More work is needed on a "clean" dataset to determine the usefulness of combining the two methods to achieve a higher performance.

References

- Bache, T. C., S. R. Bratt, J. Wang, R. M. Fung, C. Kobryn, and J. W. Given (1990). The Intelligent Monitoring System, *Bull. Seism. Soc. Am.* 80, Part B, 1833-1851.
- Patnaik, G. B., and T. J. Sereno (1991). A Neural Network Approach to Initial Phase Identification From Three-Component Polarization Measurements, *Proceedings of 13th Annual PL/DARPA Seismic Research Symposium*, 8-10 October 1991, Keystone, Colorado. PL-TR-91-2208, ADA241325.
- Riviere-Barbier, F., A. Suteau-Henson, V. Z. Ryaboy, and J. A. Carter (1991). Analysis of 3-Component Data From IRIS Stations in the USSR, *Bull. Seism. Soc. Am.*, in press.
- Suteau-Henson, A. (1991). Three-Component Analysis of Regional Phases at NORESS and ARCESS: Polarization and Phase Identification, *Bull. Seism. Soc. Am.*, in press.

Implications of DSS Observations within Scandinavia and Northwestern Russia for IMS Data Processing

Vladislav Ryaboy

Abstract

An analysis of available deep seismic sounding (DSS) profile observations for Scandinavia and north-western Russia is presented. A new P_n -wave reference travel-time curve based on DSS data and recordings by seismological networks of chemical explosions with exact location and origin time was constructed for distances up to 1400 km from statistical smoothing of P_n travel-time measurements. Beyond 800-850 km there is a break and 1.0-1.5 sec shift in the travel-time curve caused by a low-velocity layer in the upper mantle at depths of approximately 100-130 km. Discrepancies of up to 2-3 sec at distances greater than 800-1000 km were observed between DSS data and the P_n reference travel-time curves used to locate events for the IMS and Helsinki University seismological bulletins. This study yielded pronounced variations of P_n -wave propagation parameters caused by lateral structural inhomogeneities of the earth crust and upper mantle. P_n arrival times in southern Norway and Sweden at distances from 200 to 500 km are approximately 2-3 sec earlier than in southern Finland; similarly, P_n - P_g cross-over distance varies from 130 km to 270 km between these two regions.

Travel-time tables applied for location of seismic events usually do not take into consideration such path effects. The influence of path-calibrated travel-time corrections on regional event locations was tested. For the NORESS, ARCESS, and FINESA arrays we developed a set of P_n travel-time tables, calculated from interpolations and extrapolations of DSS travel-time measurements. S_n travel-times were calculated with the assumption that the Poisson's ratio is 0.25. We applied the new P_n , and the new P_n and S_n curves based on DSS observations in conjunction with travel-time tables of the IMS for P_g and L_g waves to relocate 111 regional events originally located by the IMS in different regions of Scandinavia and north-western Russia. Comparison of the IMS locations with those determined using path-dependent travel-time curves showed significant differences depending on region, number of stations and designated phases, and magnitude. The distance between relocated events and those listed in the IMS bulletin and the difference in origin time can reach 20 km and ± 1.5 sec, respectively.

The results of this study show that DSS data can be used to improve regional event locations within Scandinavia and north-western Russia, and that the derivation of similar curves and corrections for other regional phases is warranted.

Introduction

Evaluating the performance of the Intelligent Monitoring System (IMS) to improve its monitoring capabilities is an important and complicated technical and scientific problem. The system operates mainly within Scandinavia and western Russia and within these regions includes three regional arrays, NORESS, ARCESS, and FINESA, installed in southern and northern Norway, and southern Finland, respectively (Bache *et al.*, 1990). Distance between these arrays varies from approximately 800 to 1200 km. IMS also includes GERESS and two stations in Poland. The main aim of IMS is to detect, locate, and identify low-magnitude local, regional, and far-regional events for the purpose of verifying compliance with nuclear testing treaties. IMS results are critically dependent on the accuracy of event locations.

Analyses of regional event location capabilities using one-, two-, and three-array data have three main sources of error: azimuth estimation, phase misidentification, and errors in travel-time tables (Bratt and Bache, 1988; Mykkeltveit *et al.*, 1990; Vogfjord and Langston, 1990). Phase misidentifications and large azimuth errors (up to 5-10° and more) can cause errors in event locations at regional and far-regional distances of 100-200 km and more. The error will be larger for one- or two-array locations than in the three-array case. As a rule, an error of 1 sec in the travel-time difference between S and P phases results in an error of 6 km in the epicentral distance for one-array locations. As far as we know, the influence of travel-time errors on two- and three-array locations has not been analyzed.

A key to further progress in seismic monitoring is the development and application of *regional seismic knowledge*, for the purpose of detection, location, depth estimation, and source characterization (Mykkeltveit *et al.*, 1990). This requires studying regional variations in parameters of seismic wave propagation, and applying this knowledge to IMS data processing.

Direct utilization of the IMS database to collect information on regional seismic phases has important limitations. A one-dimensional plane-layered velocity model, consisting of two crustal and two upper mantle homogeneous layers, is applied to compute IMS locations (Bache *et al.*, 1990; Bratt *et al.*, 1990). The crustal thickness for this model is 40 km, and the Moho depth and the layer velocities fit the region under consideration only on average. According to detailed DSS observations, Moho depth varies from approximately 30 km in southern Norway and southern Sweden up to 60 km in southern Finland (Luosto, 1991; Sharov, 1991; Ryaboy, 1990; Kinck *et al.*, 1990). A layer with P-wave velocity of 7.3-7.4 km/sec in the lower crust was detected within areas of crustal thickening (Korhonen *et al.*, 1990). Travel-time tables used for event locations usually do not take into consideration such path effects, and the IMS database should have an area dependent bias.

Travel-time table corrections will help eliminate this bias.

Much of the necessary and reliable information on regional seismic wave propagation parameters can be obtained through DSS observations. Scandinavia and north-western Russia are covered with a dense network of DSS profiles crossing this region in different directions. The length of each DSS profile varies from 200 to 2000 km. Chemical explosions with exact locations and timing and some DSS explosions were also recorded by seismological networks to distances beyond 1000 km (Dahlman, 1967; Porkka *et al.*, 1972; Sellevoll and Pomeroy, 1968; Mereu *et al.*, 1983; Bath, 1981). These data can be used to measure propagation parameters of major regional phases (Pg , Pn , Sg , Sn , and maybe Lg) for different areas. Results of the measurements can help improve IMS data processing.

This study analyzes Pn travel-times, constructs a new reference travel-time curve for this wave based on DSS data and explosion seismology observations with controlled sources, and estimates Pn travel-time regional variations. We also tested the influence of path-calibrated travel-time corrections on two- and three-array locations. For the NORESS, ARCESS, and FINESA arrays, we developed a set of Pn travel-time tables, obtained from interpolations and extrapolations of DSS data and recordings of explosions with controlled sources. Sn travel-times were calculated with the assumption that the Poisson's ratio is 0.25 (P - to S -wave velocity ratio is 1.73). We applied the new Pn , and the new Pn and Sn tables in conjunction with IMS travel-time tables for Pg and Lg waves to relocate 111 regional events originally located by the IMS in different regions of Scandinavia and north-western Russia. Comparison of the original IMS locations with those determined using path-dependent travel-time curves showed significant differences depending on region, number of stations and designated phases, and event magnitude.

Finally, the results of this study are discussed, and some perspectives on the application of DSS observations to IMS data processing are given.

Pn Wave Analysis

Data

Scandinavia and north-western Russia are covered with a dense network of DSS profile observations (Figure 21). The results of these studies were published in numerous papers, monographs, and dissertations (e.g. Proceedings..., 1971, 1990; EUGENO-S..., 1988; Guggisberg, 1986; Stangl, 1990; Study of the deep structure..., 1986; Ryaboy, 1989; Structure..., 1991; Imaging and..., 1991; The European..., 1989; Luosto *et al.*, 1984, 1990; Korhonen *et al.*, 1990). The length of the DSS profiles vary from 200 to 2000 km for the FENNOLORA profile (see Figure 21, profile 1). Field observations were usually carried

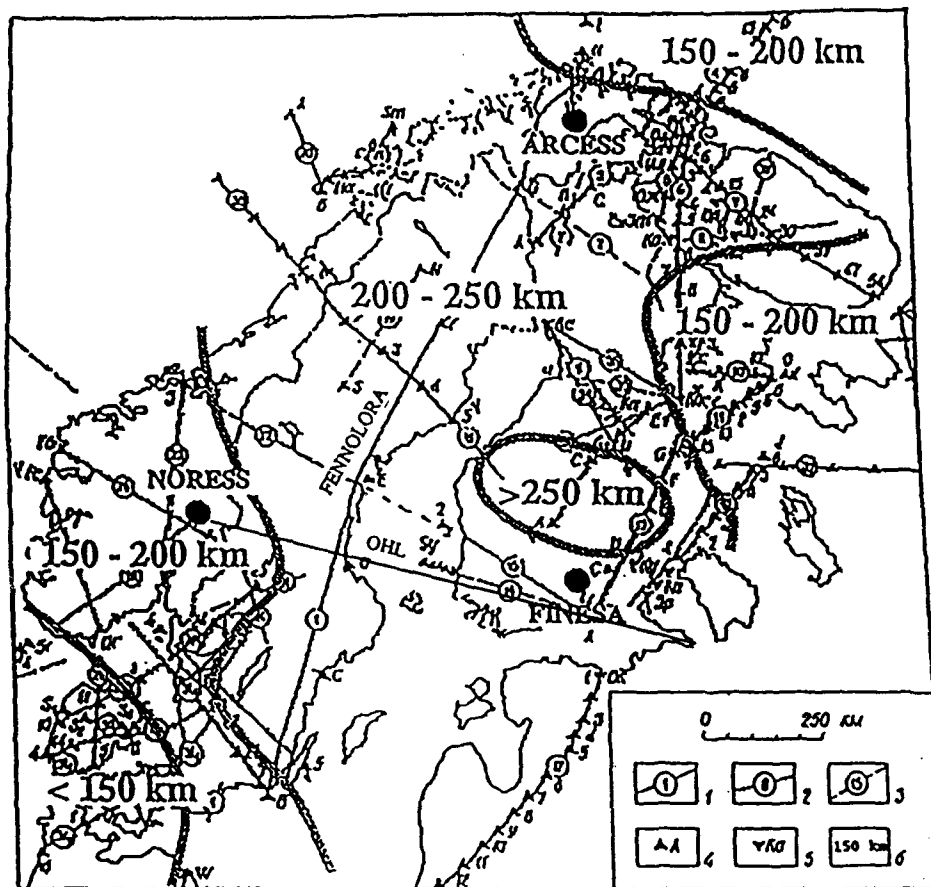


Figure 21: A map of DSS profile locations and P_g/P_n cross-over distance. 1 - 3 - DSS profiles with different methods of field observations, 4-5 - main shot points, 6 - P_g/P_n cross-over distance. DSS profile locations adapted from a paper (Sharov, 1991).

out along reversed and overlapping lines. Seismic signals were recorded in the frequency range from 1-2 Hz up to 20-25 Hz by vertical and, recently, horizontal sensors. *P*- and *S*-refracted and reflected waves from crustal and upper mantle boundaries were detected along the DSS profiles.

With the goal of constructing a new *Pn* reference travel-time curve based on the most accurate observations, we collected and analyzed available *Pn*-wave record sections and travel-time curves inferred from DSS observations and from recordings of chemical explosions with well known location and origin time at seismological networks (Dahlman, 1967; Sellevoll and Pomeroy, 1968; Porkka *et al.*, 1972; Bath, 1981) and seismic arrays (Cassell *et al.*, 1983; Mereu *et al.*, 1983).

A number of shots detonated during the 1979 FENNOLORA DSS project from nine major shot points were recorded by the NORSAR array at regional distances. We constructed and analyzed record sections for all of these shot points, using filtered beams at each of the seven NORSAR sub-arrays (Ryaboy, 1990). This enabled us to obtain a better signal to noise ratio (SNR) than with beams constructed for a group of NORSAR sub-arrays (Mereu *et al.*, 1983) because of better coherency. Sometimes, the SNR before beamforming was good, and we also included filtered single-sensor traces in record sections. Examples of the data are shown in Figures 22 through 26 (record sections from shot points D, E, C, B, H and I of the FENNOLORA experiment). We also analyzed NORESS recordings of shots detonated along the POLAR DSS profile in northern Norway and Finland south of ARCESS (The European Geotraverse, 1989). They had poor SNR, and beams constructed for different explosions did not indicate marked improvement in SNR. We were able to improve SNR significantly and correlate the *Pn*-wave only after stacking beams for several explosions detonated at the same shot point (Figure 27).

Analysis of *Pn* waveforms showed that this group of waves has a very complicated structure at distances greater than 300 km. This is observed most clearly when conducting detailed observations along reversed and overlapping lines. The emergence of *Pn* waves as the first arrivals is typically accompanied by an increase in apparent velocities from 6-7 km/sec (*Pg* wave) to 7.5 km/sec or higher. Travel-time curves of *Pn* first arrivals are not linear, and there is a tendency toward a gradual rise in the apparent velocities with increasing distance, from approximately 8.0 to 9.0 km/sec and more at ranges 1000 to 1500 km. Strong arrivals with high apparent velocities are often detected as later phases in the *Pn* wave group. The interval over which they can be correlated fluctuates from tens to hundreds of km. Large later arrivals, as a rule, are characterized by a lower frequency than the low-amplitude waves recorded as first arrivals. Figures 22 through 26 show *Pn* first arrivals and strong later waves recorded at the NORSAR array from FENNOLORA DSS profile explosions.

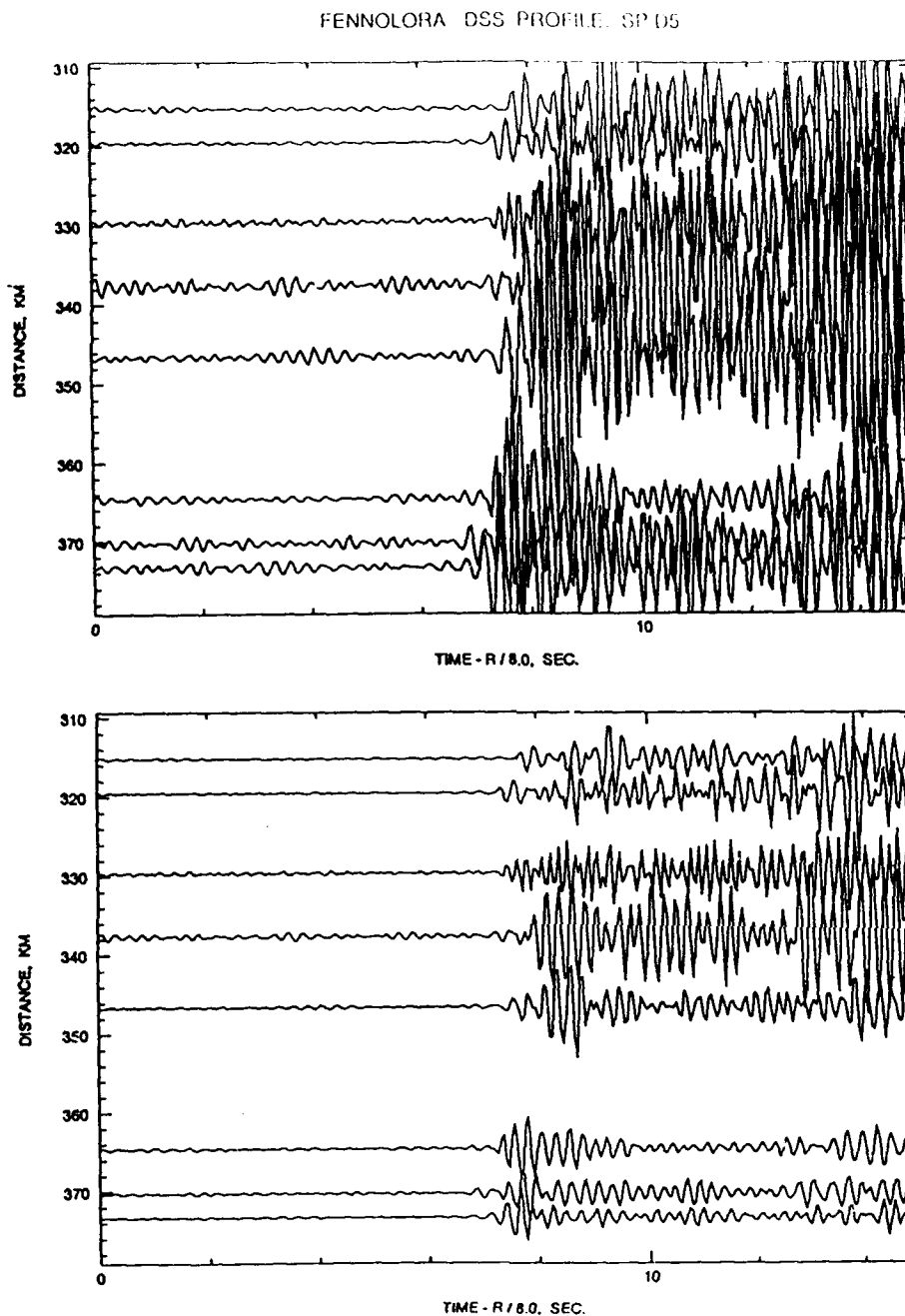


Figure 22: Trace-normalized record sections from shot point (SP) D5 (FENNOLORA DSS profile) recorded at the NORSAR array (filter: 2 to 8 Hz). Azimuth from NORESS to SP D is 85.92° . Seismic wave amplitudes for top record section were increased relative to bottom one to search for low amplitude arrivals. One can see that the first arrivals of the P_n wave have small amplitudes, and later arrivals are stronger and usually have lower frequencies.

FENNOLORA DSS PROFILE. SP E4

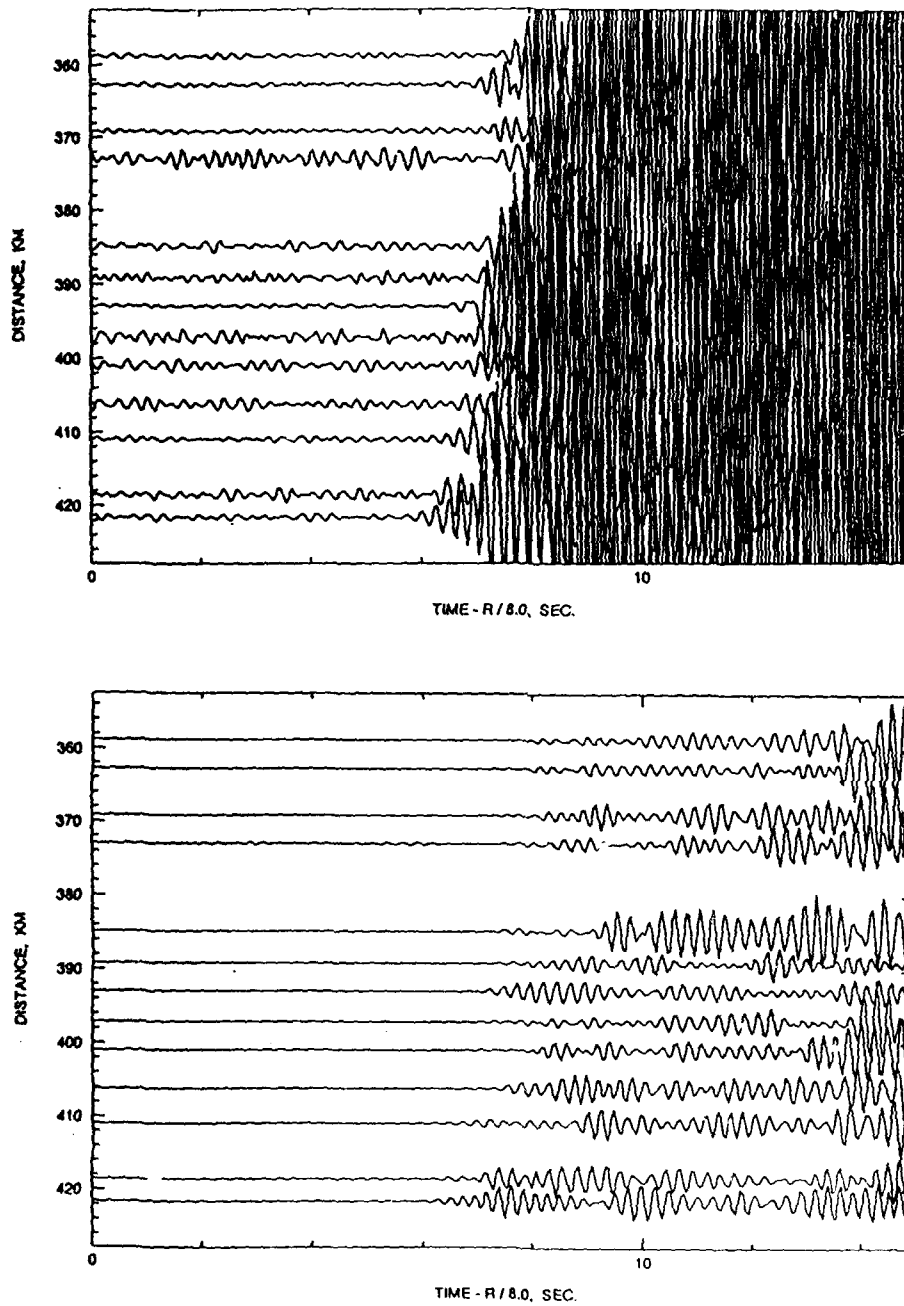


Figure 23: Same as Figure 22 but for SP E4. Azimuth from NORESS array to SP E is 58.82° .

FENNOLORA DSS PROFILE. SP C1

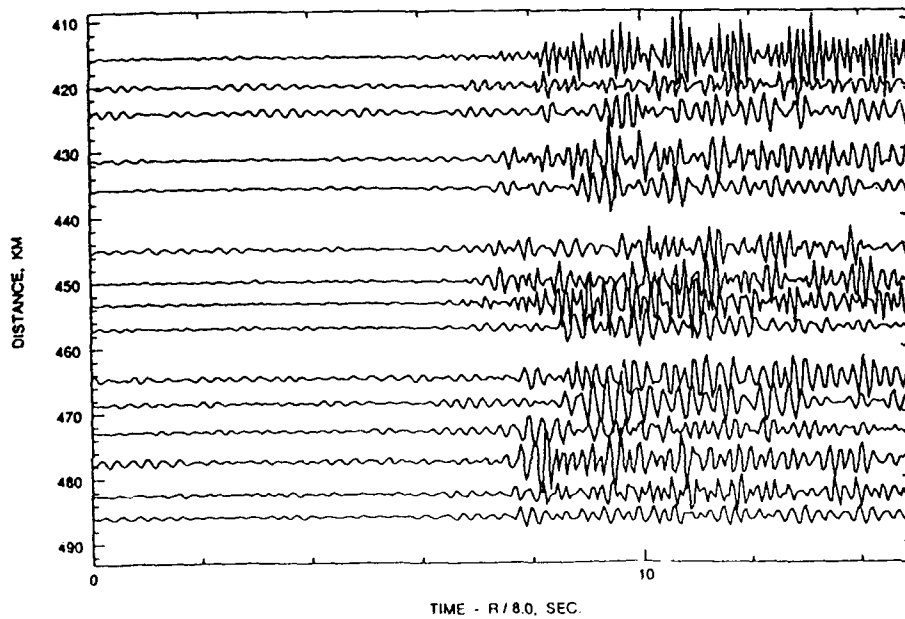
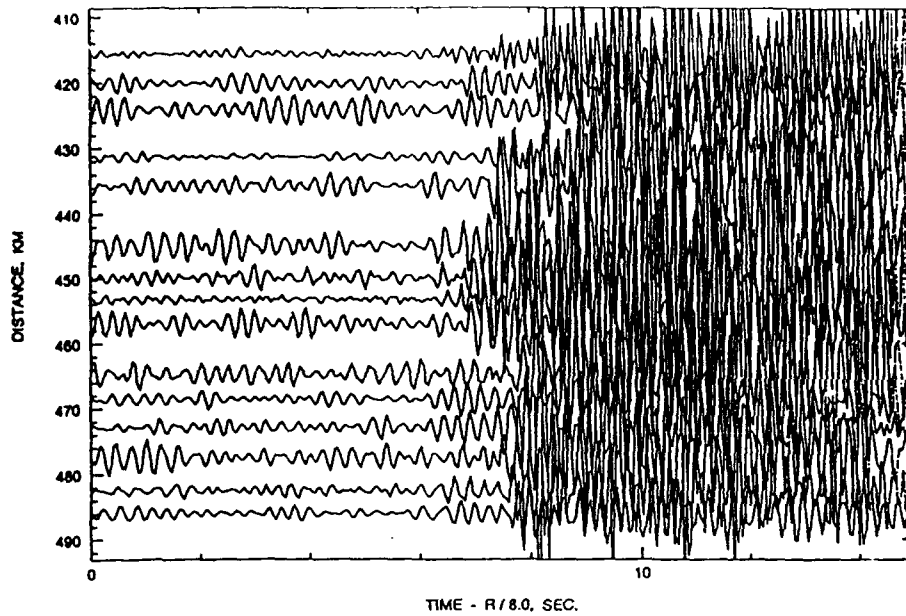


Figure 24: Same as Figure 22 but for SP C1. Azimuth from NORESS array to SP C is 124.90°.

FENNOLORA DSS PROFILE. SP B4

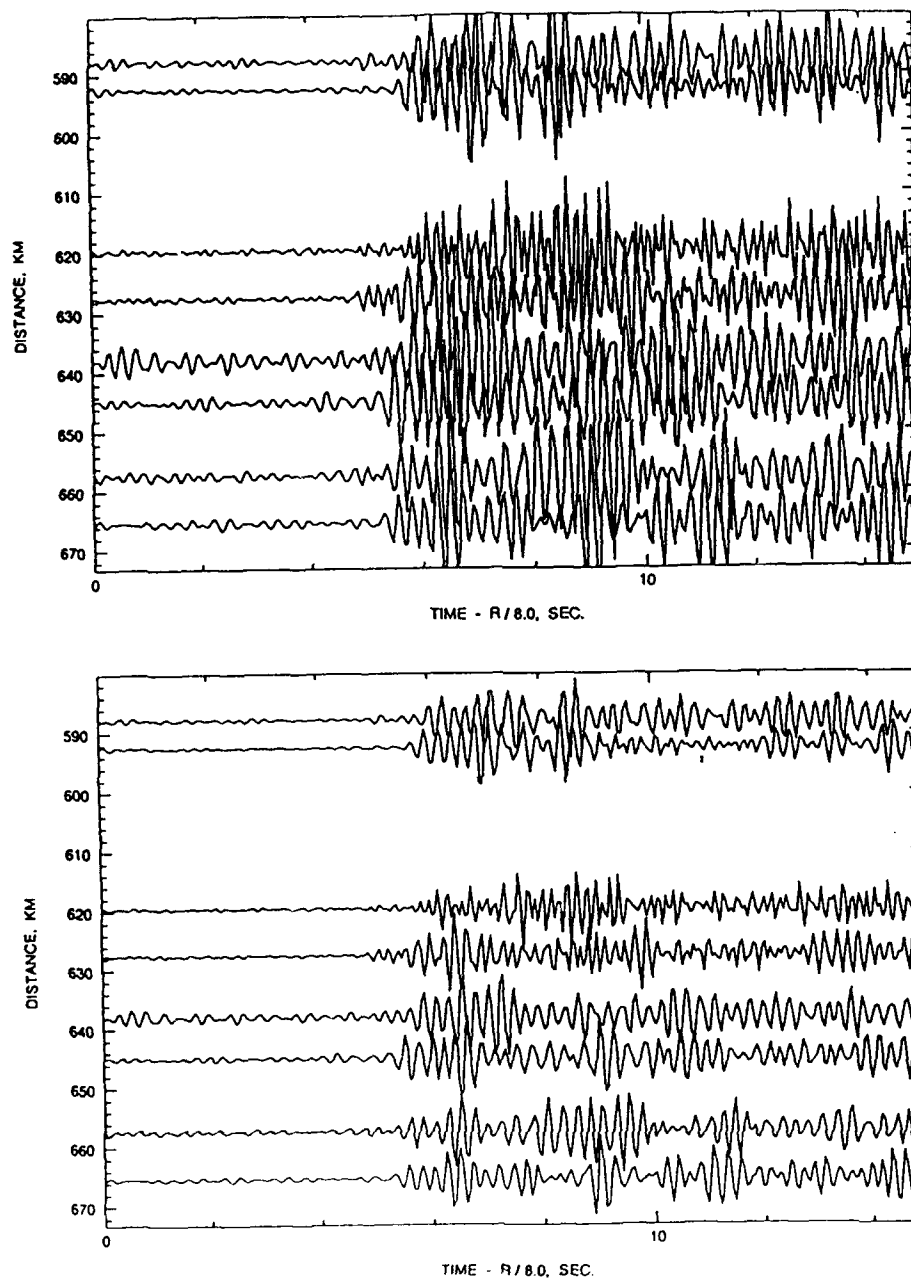


Figure 25: Same as Figure 22 but for SP B4. Azimuth from NORESS array to SP B is 152.95° .

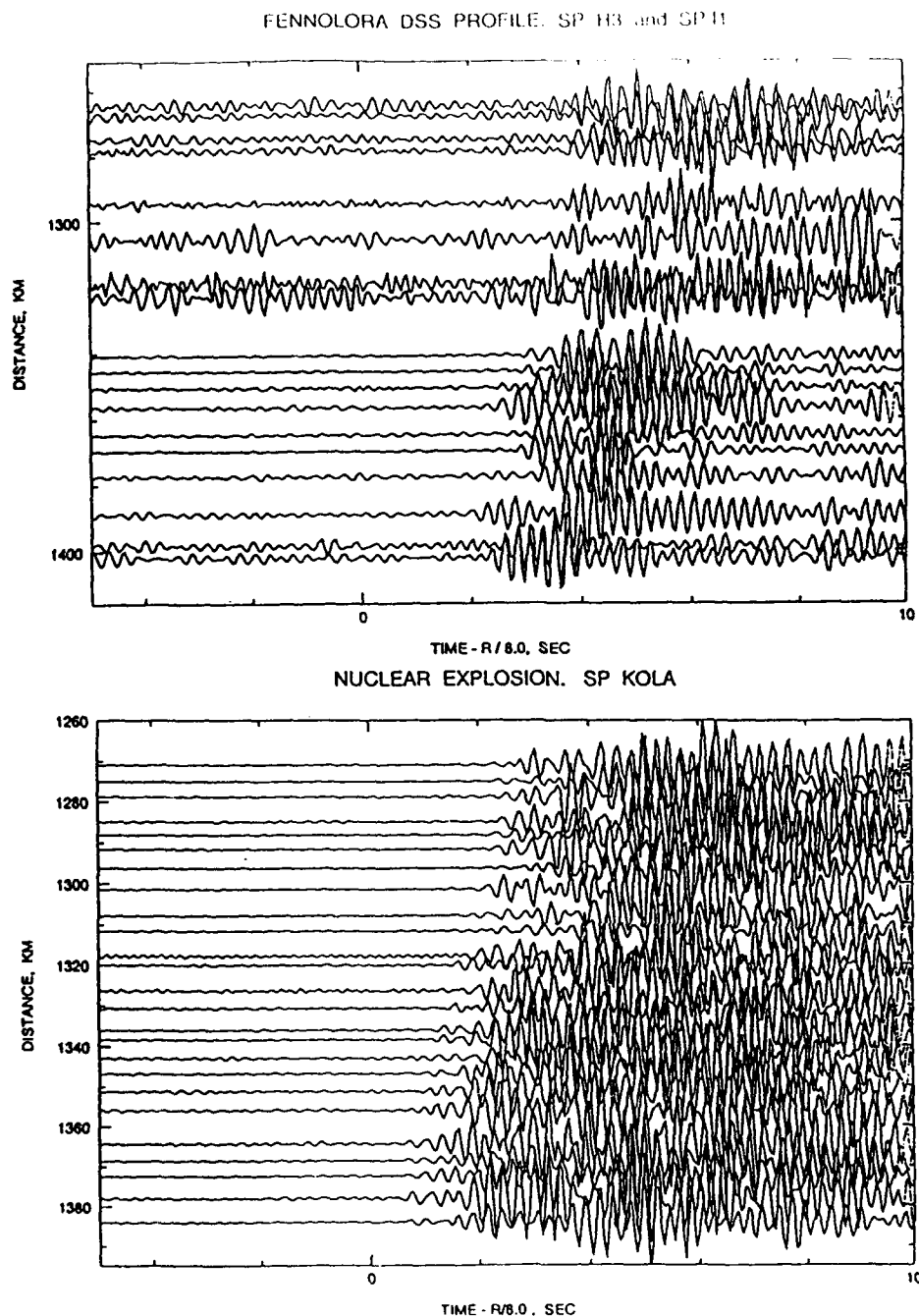


Figure 26: Top: same as Figure 22 but for SP H3 and SP I1. Azimuths from the NOR-ESS array to SP H3 and SP I1 are 22.53° and 20.78° , respectively. Bottom: record section constructed from NORSAR recordings of a nuclear shot on 4 September 1972 (SP Kola) in the southwestern part of the Kola peninsula (Apatity area). Origin time and location of SP Kola are based on relocation results (Shore, 1982). Azimuth from NORESS array to SP Kola is 44.13° .

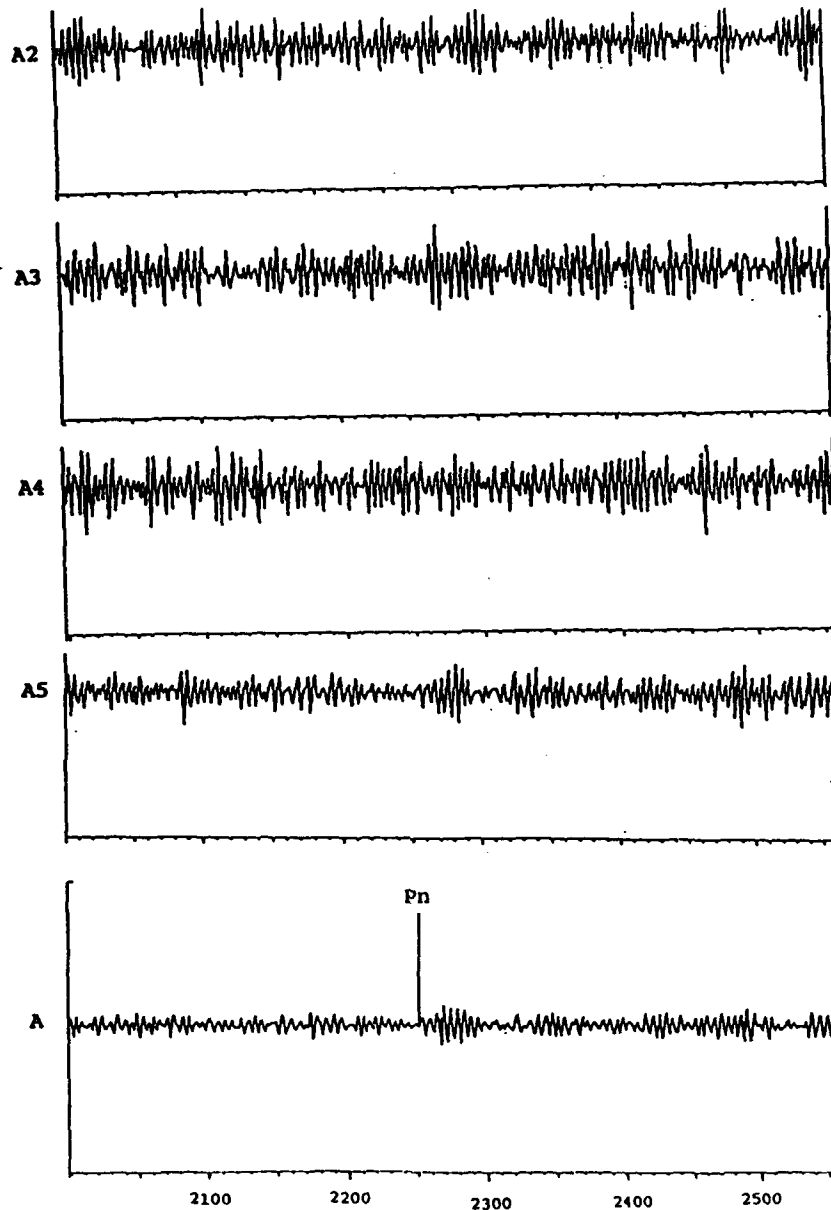


Figure 27: NORESS recordings at a distance of 963.5 km from SP A (POLAR DSS profile in northern Norway and Finland). A2 - A5 are beams constructed with a velocity of 8.0 km/sec (filter: 2 to 8 Hz) for four different shots with charge 960 , 960, 1680, and 1680 kg, from top to bottom. A is a coherent stack of the four beams A2 - A5. One can see an improvement in SNR for the *Pn* wave after stacking the beams.

Analysis of record sections constructed for the FENNOLORA profile (Guggisberg, 1986; Hauser and Stangl, 1990) showed that beyond 800-900 km there is a shift of 1.5 - 2.5 sec in the travel-time curve, with the first arrival decaying and a later phase appearing as the first arrival. At greater distances there is an increase in apparent velocity of the first arrivals (up to 8.6-8.8 km/sec) and often a decrease in frequency. For example, Figure 28 shows a record section constructed for the FENNOLORA DSS profile from shot point I (Hauser and Stangl, 1990). A similar break in the Pn travel-time curve and an offset to later time was observed on record sections constructed from NORESS recordings of mine explosions for southern areas of the Baltic shield (Figure 29), and for central and northern regions of the Russian platform plate (Ryaboy, 1989). The distance for which these breaks occur and the offset magnitude varies in different areas. Attenuation of Pn first arrivals and 0.5 sec offset were also observed at distances less than 800 km for several DSS profiles within Scandinavia (Lund, 1979; Proceedings..., 1990). These offsets were influenced by SNR, occurred at different distances, and could not be reliably correlated along DSS profiles. They probably are caused by local small-scale inhomogeneities of the earth crust and upper mantle.

Pn -wave propagation parameters such as travel-time, cross-over distance, amplitudes, frequencies, and polarization characteristics (Suteau-Henson, 1991) vary in different regions of Scandinavia. For example, we compare two DSS record sections; a North Sea - southern Norway profile (Figure 30) and the SVEKA (Figure 31) profile. The latter was observed in central and southern areas of Finland. The DSS profile in southern Norway was based on land recordings of offshore explosions. The waveforms beyond 450 km for the northern end of the record section in Figure 30 were recorded at the NORSAR array. There are very important difference between these two record sections. The Pg / Pn cross-over point is located at a distance of 150 and 270 km in southern Norway and southern Finland, respectively. One can see that the first arrivals on the record section for the SVEKA profile at a distance range from 150 to 270 km are refracted waves with apparent velocities 6.5 and 7.35 km/sec, caused by layers in the middle and lower crust. Waves with similar apparent velocities were not recorded in southern Norway. Figure 21 shows a map of Pg / Pn cross-over distance variations constructed from DSS profile observations. The distance varies within Scandinavia and northwestern Russia from 130 to 270 km. Maps of this type can be very helpful for Pg and Pn phase identification in different regions during IMS data processing.

Secondary Arrivals

The record sections in Figures 22 through 26 and Figure 30 show a set of Pn waveforms from DSS explosions recorded at NORSAR at azimuths ranging from 20 to 225° and at

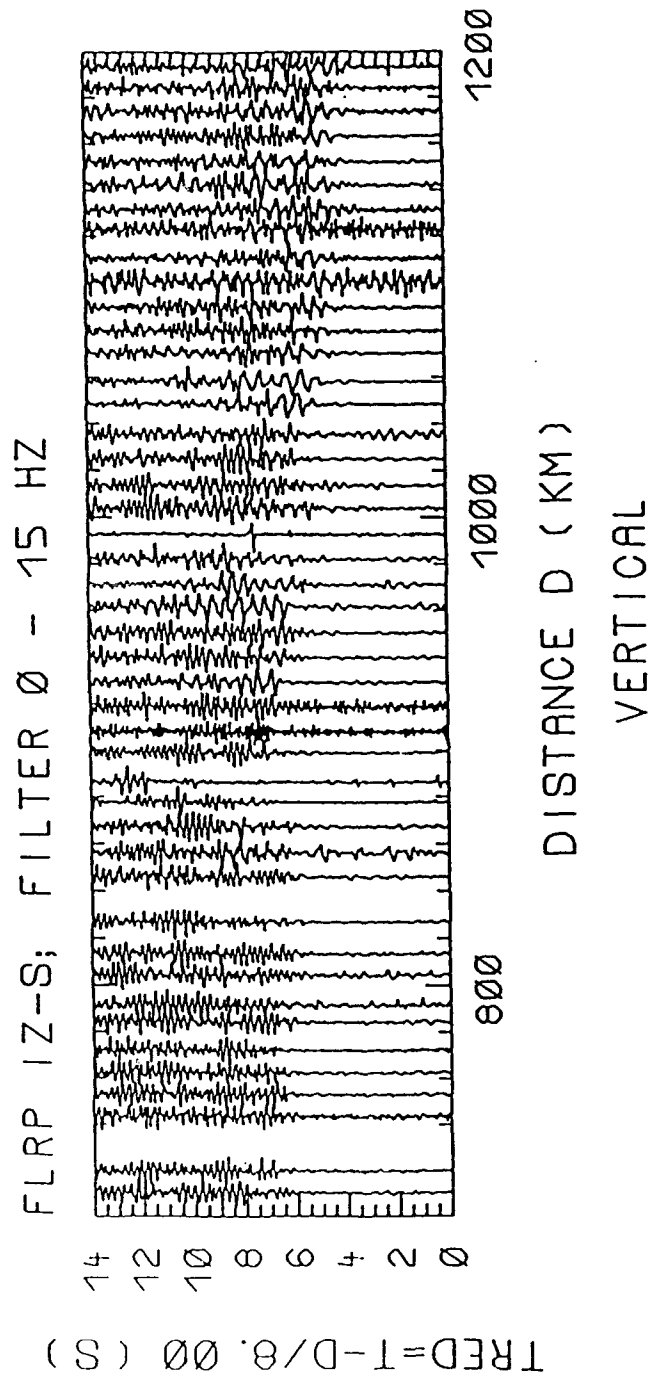


Figure 28: Record section for the FENNOLOGRA DSS profile from SP I to the south (adapted from Hauser and Stangl, 1990). Note the delayed travel-time branch beyond 850-900 km, followed by an increased apparent velocity and frequency drop.

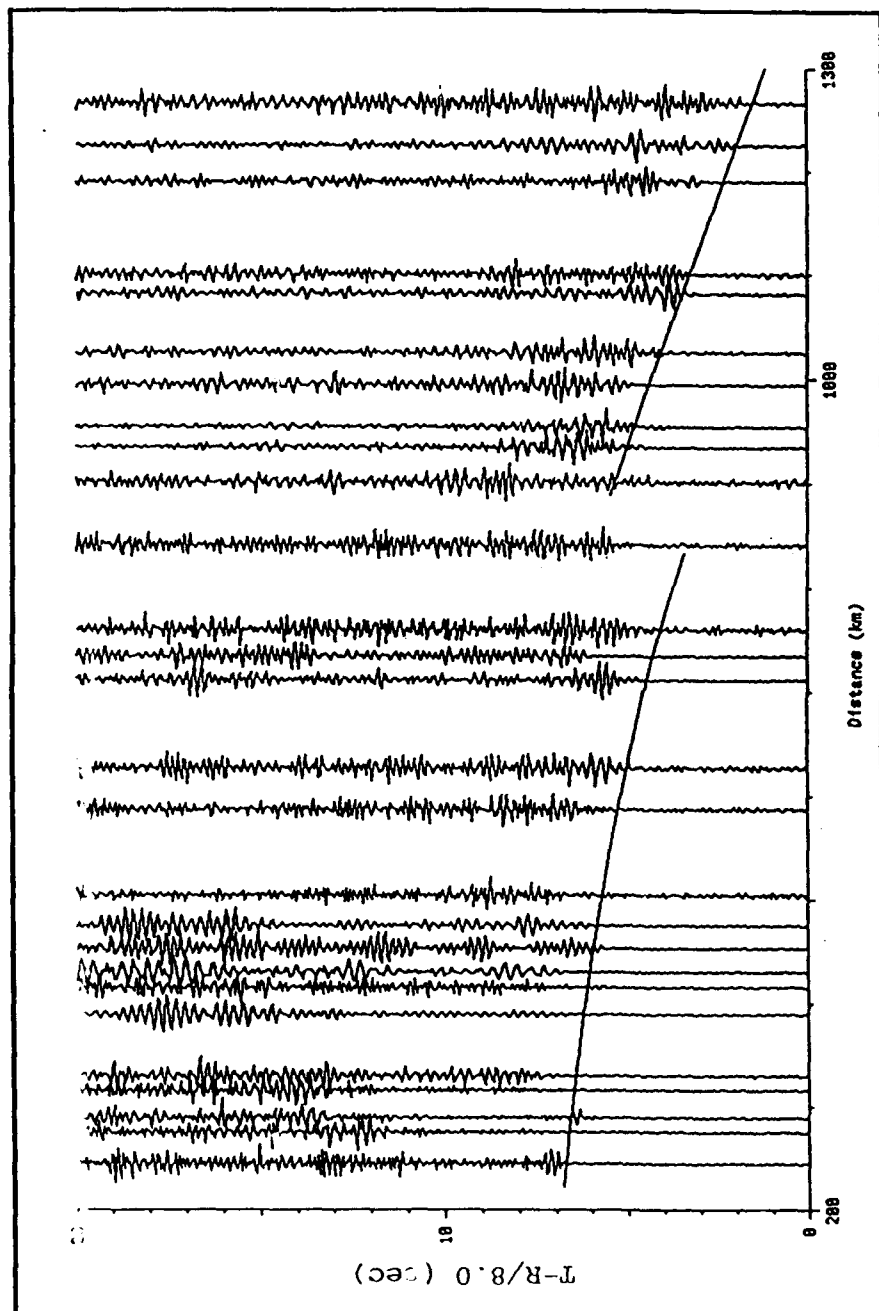


Figure 29: Record section for the Oslo-Helsinki-Leningrad profile overlain by theoretical travel-time curves of waves refracted in two upper mantle layers separated by a low-velocity zone from approximately 105 to 135 km depth (adapted from Ryaboy, 1990). This record section was constructed mainly for mine explosions recorded at NOR-ESS array. One can see that the first arrivals can be traced continuously to a distance of 800-850 km, where there is a break and shift of approximately 2.0 sec in the travel-time curve and an increase of apparent velocity.

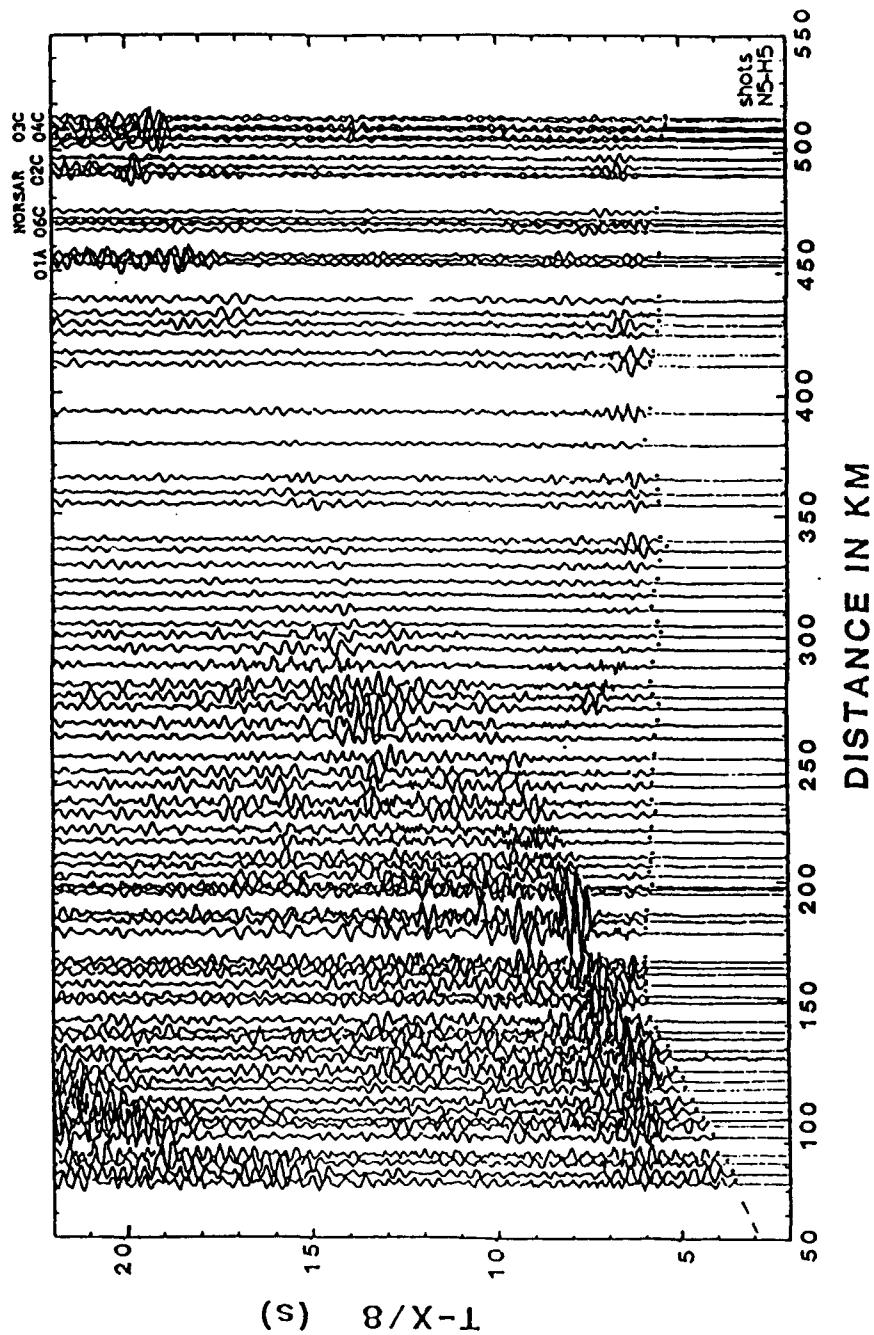


Figure 30: Record section for a North Sea - southern Norway DSS profile (adapted from Cassell *et al.*, 1983). Shots were detonated in the North Sea and seismic waves were recorded within southern areas of the Baltic shield. The records beyond 450 km were recorded by the NORSAR array. The azimuth from NORESS is 224.75° . The Pg/Pn cross-over distance is 150 km.

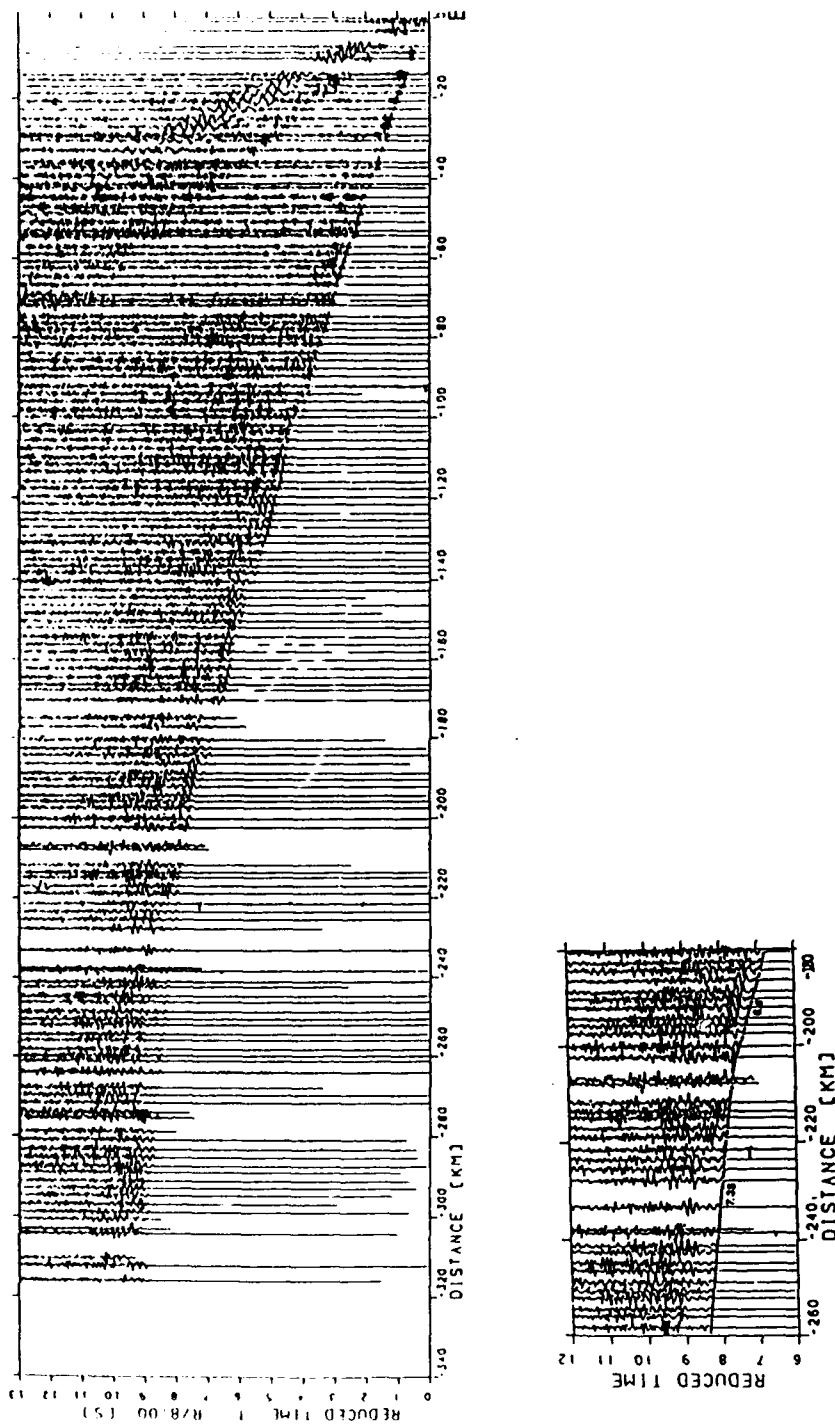


Figure 31: Top: record section for the SVEKA DSS profile in central Finland from shot point E (adapted from Luosto *et al.*, 1984). Bottom: the record section is shown on an enlarged scale for the distance range of 180-260 km. The P_g/P_n cross-over distance is approximately 270 km. A wave refracted in the lower crust with apparent velocity 7.35 km/sec was recorded within the distance range 210-270 km.

distances from approximately 300 to 1400 km. Analyses of these record sections showed that P_n first arrivals usually have smaller amplitudes and higher frequencies than later arrivals. Especially clear is the complicated structure of the group of P_n waves on the record section constructed from a nuclear shot detonated on 4 September 1972 in the Apatity region of the Kola peninsula (Figure 26, bottom). Apparent velocities, amplitudes, number of later arrivals, and travel-time differences between later arrivals and the first arrivals are dependent on distance and azimuth. These high amplitude later arrivals are the subjects of careful DSS studies because they are very informative for constructing detailed two-dimensional upper mantle velocity sections. Many published papers have been devoted to the interpretation of these waves. High amplitude secondary arrivals recorded at regional and far-regional distances are mainly reflected waves from sub-horizontal and dipping reflectors of different lengths. Intensive converted and scattered waves of different types generated by small-scale lateral inhomogeneities near the source and receiver can also be recorded as later arrivals at these distances. All these waves are different in physical nature and ray paths from P_n refracted waves recorded as first arrivals, and can influence magnitude estimation, azimuth and slowness measurements, and phase identification of the major regional phases, P_n , S_n , P_g , and L_g , used for event location.

The effects of dipping reflectors on later arrivals have been observed in modelling experiments. Figures 32A and B show examples of ultrasonic modelling of waves generated in media with horizontal and dipping boundaries (Berzon, 1977). The record section from the modelling experiment (Figure 32 B) shows a refracted P wave as a first arrival, and (PP)1 and (PP)2 as waves reflected from the dipping and horizontal boundaries 1 and 2 (Figure 32 A), respectively. In this model the reflected wave (PP)1 is only observed in the direction of decreasing depth for dipping reflectors, and was not recorded for source S-2 (Figure 32 B). Figure 32 C shows a record section constructed for a refraction profile in the Altay region. The strong P1 phase recorded as a later arrival was identified as a wave reflected from an overthrust. The P_g phase recorded as a first arrival is a wave refracted in the upper crust. The record sections in Figures 32 B and C are qualitatively similar to P_n record sections constructed at regional distances, but P_n first arrivals typically have small amplitudes (Figures 22 through 26) because of small velocity gradients in the upper mantle. Results from modelling waves recorded at regional and far-regional distances in Scandinavia were published in many papers (Lund, 1979; Guggisberg, 1986; Stangl, 1990; Ryaboy, 1990).

With the IMS data processing procedure, the location of regional events is critically dependent on the azimuth and slowness of the detected signals (Mykkeltveit *et al.*, 1990). These parameters are estimated from f - k analysis using a 3 sec time window (Bache *et al.*, 1990). The intensive waves in later arrivals are observed in this window and affect the

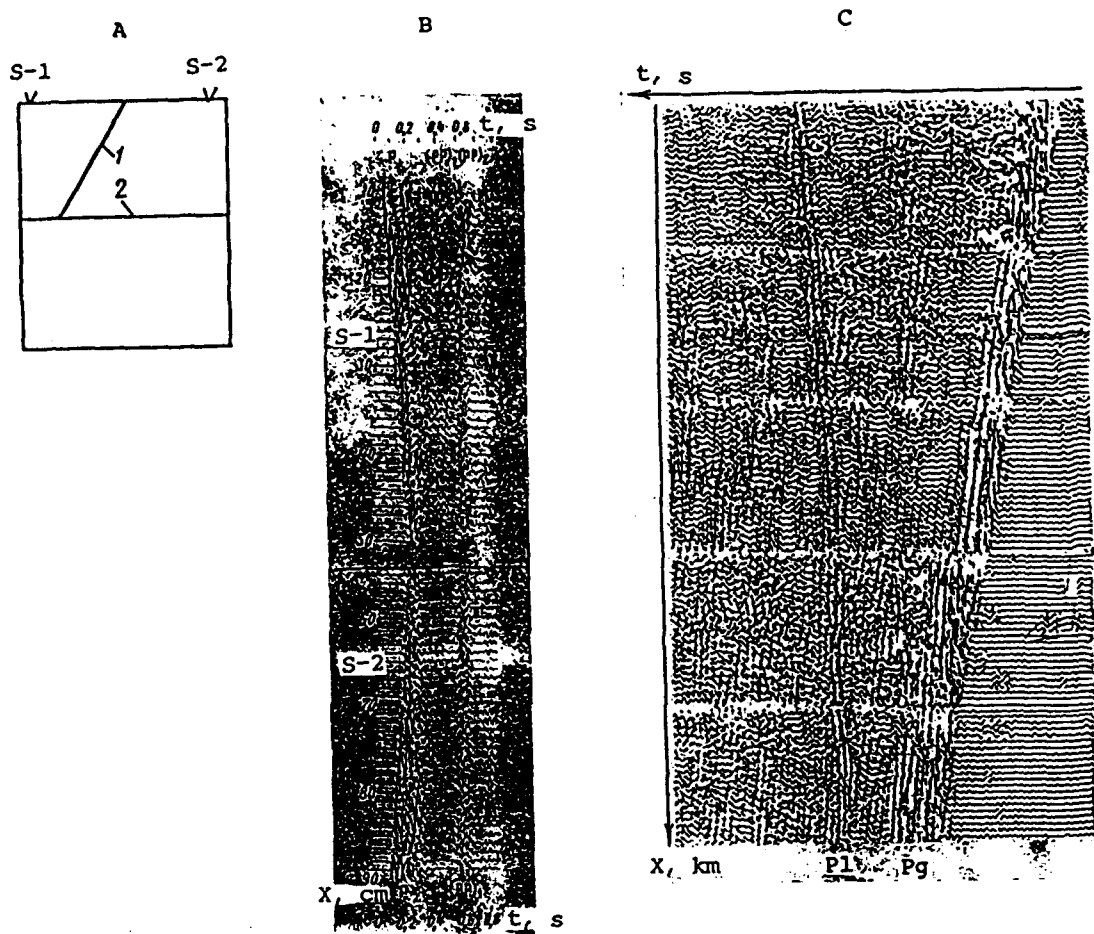


Figure 32: Results from ultrasonic modelling (A and B) and record section (C) of waves generated in media with a dipping interface (adapted from Berzon, 1977). A - physical model of the medium (S-1 and S-2 are sources of vibration; velocities and densities vary on boundaries 1 and 2). B - record section constructed for source of vibration S-1 (P - refracted wave, (PP)1 - wave reflected from dipping interface 1, (PP)2 - wave reflected from horizontal interface 2; (PP)1 wave was not recorded for source of vibration S-2). C - example of record section constructed for refraction profile in Altay region crossing a dipping overthrust (Pg - wave refracted in the basement, P1 - wave reflected from the overthrust).

results. This influence depends on distance, azimuth, SNR, and may contribute to the large scatter of azimuth measurements (A. Suteau-Henson, this Report). Further studies of the influence of intensive waves recorded as later arrivals on f - k computations and amplitude measurements will help us improve azimuth, slowness, and magnitude estimations. Poor SNR causes misidentification of intensive waves in later arrivals as P_n (Vogfjord and Langston, 1990; Ryaboy, 1990). The development of methods eliminating the influence of emergent later arrivals is a very important task for improving regional event locations.

Reference Travel-Time Curves

Significant variations of P_n travel-times were observed in different regions. For example, at a distance of 300 km P_n travel-times were 3.3 seconds different for southern Norway and southern Finland (Figures 30 and 31). We collected and analyzed all available P_n -wave record sections and travel-time curves constructed for DSS profiles to correlate and measure travel-times of P_n first arrivals. We also utilized record sections constructed from NORSAR / NORESS recordings of DSS explosions, and P_n travel-times from explosions with well known locations and origin times. Observations were carried out for the FEN-NOLORA DSS profile up to a distance of 2000 km, but first arrivals could be reliably picked up to distances of 1300-1400 km. Waves recorded as first arrivals at larger distances are probably intensive reflected waves from boundaries in the upper mantle, and refracted P_n first arrivals cannot be correlated because of poor SNR.

To construct a reference travel-time curve, we applied statistical least-square smoothing to all P_n first arrival travel-times in our data set (1420 measurements), and to two subsets corresponding to distances of less than 850 km (1200) and 850-1400 km (220) (Figure 33). The measurements were made from the P_n record sections and published travel-time curves (measured at ten km spacing). P_n travel-times from explosions with controlled sources recorded in seismological networks were also used. Figure 34 shows a density plot of residuals from the continuous P_n reference travel-time curve derived here. The residuals vary from about -2.0 to 2.5 sec and the root-mean-square value of residuals is ± 0.65 sec. Variations in the residuals are at least ten times larger than the observational error. Thus, the residuals are mainly caused by regular factors such as lateral structural variations of the earth crust and upper mantle.

Beyond 850 km there appears to be a break and shift of approximately 1.0-1.5 sec in the travel-time curve, and P_n apparent velocity at distances greater than 850 km rises to 8.6-8.8 km/sec. The curve consisting of two branches in Figure 33 fits the P_n wave record sections (Figures 28 and 29) better than the other curves. The 95% confidence interval of the reference travel-time curve is estimated to be ± 0.2 sec, lending support to the significance of the break in the travel-time curves at 850 km. Discrepancies of up to 2-3 sec at dis-

P_n TRAVEL-TIMES FOR SCANDINAVIA

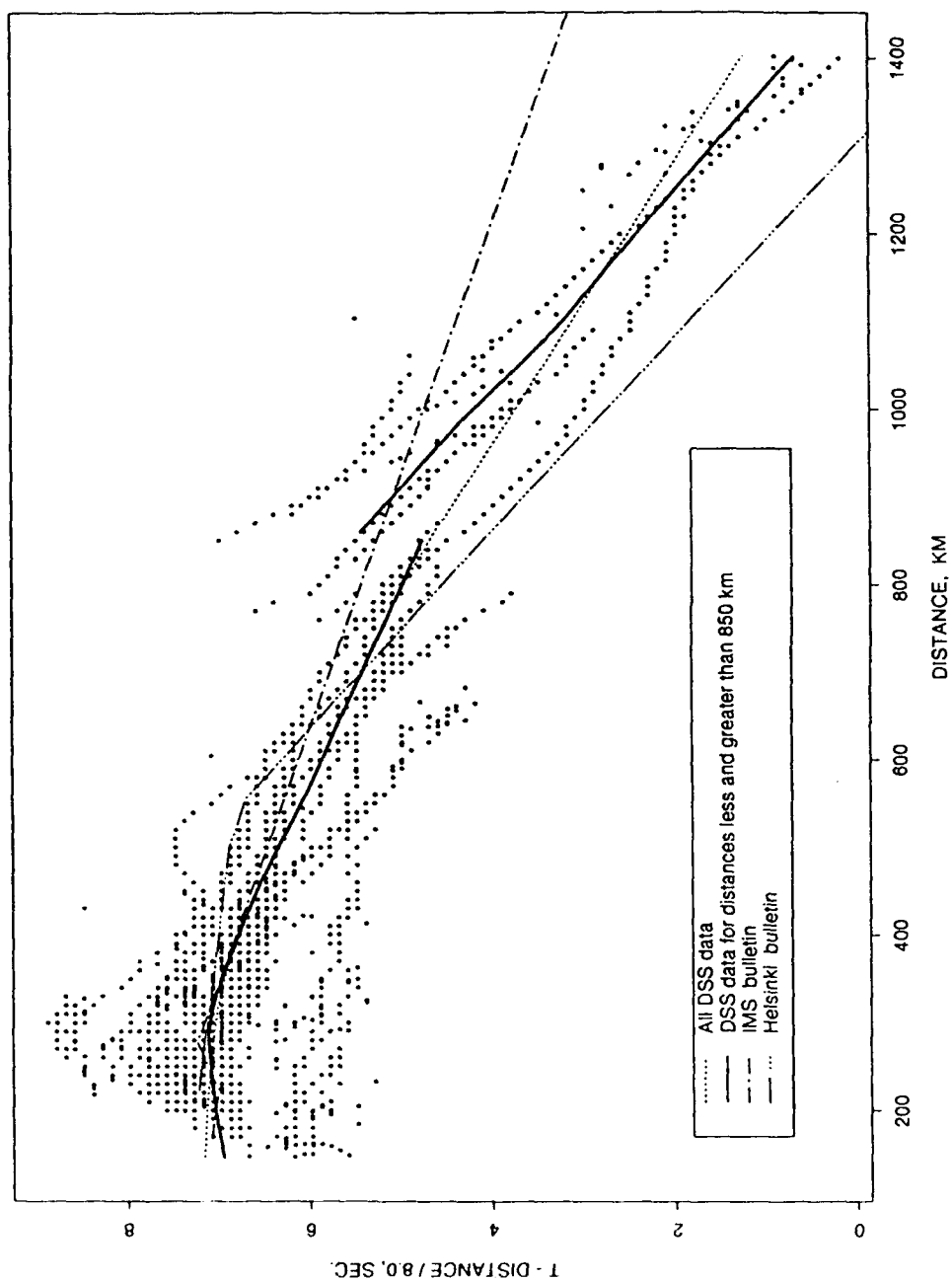


Figure 33: P_n -wave travel-times for Scandinavia and northern Russia. One can see a large scatter in P_n travel-times and discrepancies of up to 2-3 sec at distances greater than 500-600 km between DSS data and P_n travel-time curves used to locate events for the IMS and Helsinki University seismological bulletins.

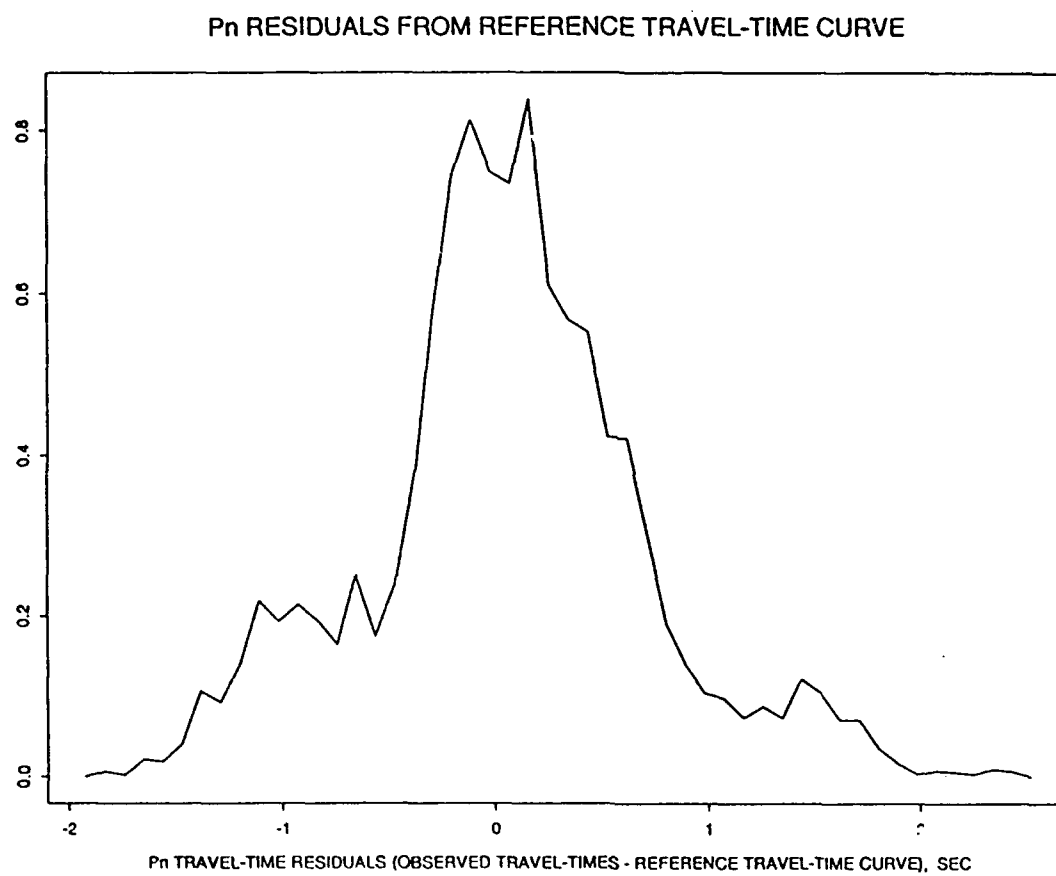


Figure 34: Density plot of Pn travel-time residuals.

tances greater than 800-1000 km were observed between DSS data and the P_n reference travel-time curves used to locate events for the IMS and Helsinki University seismological bulletins (Figure 33).

Travel-Time Anomalies

Pronounced P_n travel-time anomalies were detected in Scandinavia. For distances less than 400-500 km we have enough DSS observations to construct a map of average residuals from the reference travel-time curve (Figure 35) and analyze P_n travel-time variations in different areas. In southern Norway and southern Sweden the P_n -wave is recorded 1.0-1.5 sec early, and in southern Finland 1.0-1.5 sec late relative to our P_n reference travel-time curve based on DSS data. The smallest P_n travel-times were observed within a narrow zone of the Oslo graben 50-100 km wide, south of the NORSAR / NORESS arrays. In the southern part of the FENNOLORA profile at distances of 800-1000 km the P_n -wave is recorded 1.5-2.0 sec earlier (shot point B) than in the northern part of the profile (shot points I and H). So large a difference in travel-times cannot be explained by variations of crustal structure along the profile, and probably indicates a zone of increased velocity in the lower lithosphere beneath southern Sweden. This zone was detected in a joint interpretation of seismic and gravity observations for the Oslo-Helsinki-Leningrad profile (Ryaboy, 1990), and it also agrees with observations of teleseismic data (Husebye *et al.*, 1986).

The observed variations of P_n -wave propagation parameters are caused by pronounced crustal and upper mantle lateral inhomogeneities in Scandinavia and north-western Russia. Travel-time tables applied for the location of seismic events usually do not take into consideration such path effects. In the next section the influence of travel-time corrections, path-calibrated by DSS data, on regional event locations is investigated.

Relocation of Seismic Events Originally Located by the IMS

Azimuthal corrections in the IMS P_n travel-time tables were developed for NORESS, ARCESS, and FINESA regional seismic arrays based on DSS observations to test the influence of path-calibrated travel-time corrections on regional event locations. Azimuthal zones with constant P_n travel-time curves were selected for each array. The azimuths corresponding to the boundaries between these zones and their P_n travel-time tables were obtained from interpolations and extrapolations of DSS travel-time measurements, as described in the previous section. We developed a set of eight different P_n travel-time tables including the new P_n reference table (NEW). NEW was used for areas where pronounced residuals from P_n reference travel-time curve were not observed (for example, see the zone to the north of NORESS in Figures 35 and 36). Figures 36 and 37 show the

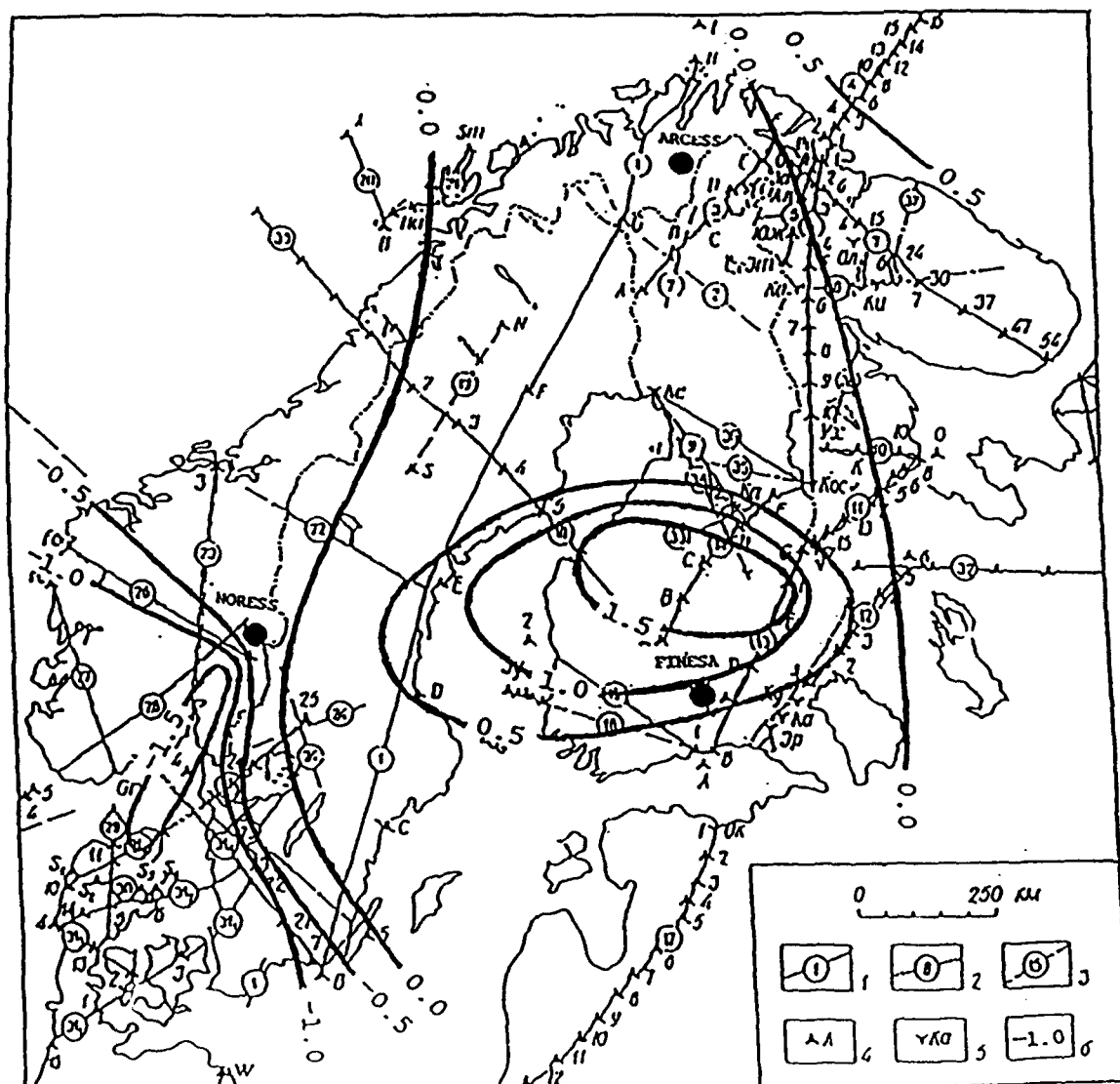


Figure 35: A map of *Pn*-wave travel-time residuals for the distance range from the *Pg* / *Pn* cross-over point to 400 km. 1-3 - DSS profiles with different methods of field observations, 4-5 - main shot points, 6 - isolines of *Pn* travel-time residuals in sec. The DSS profile locations are adapted from Sharov (1991).

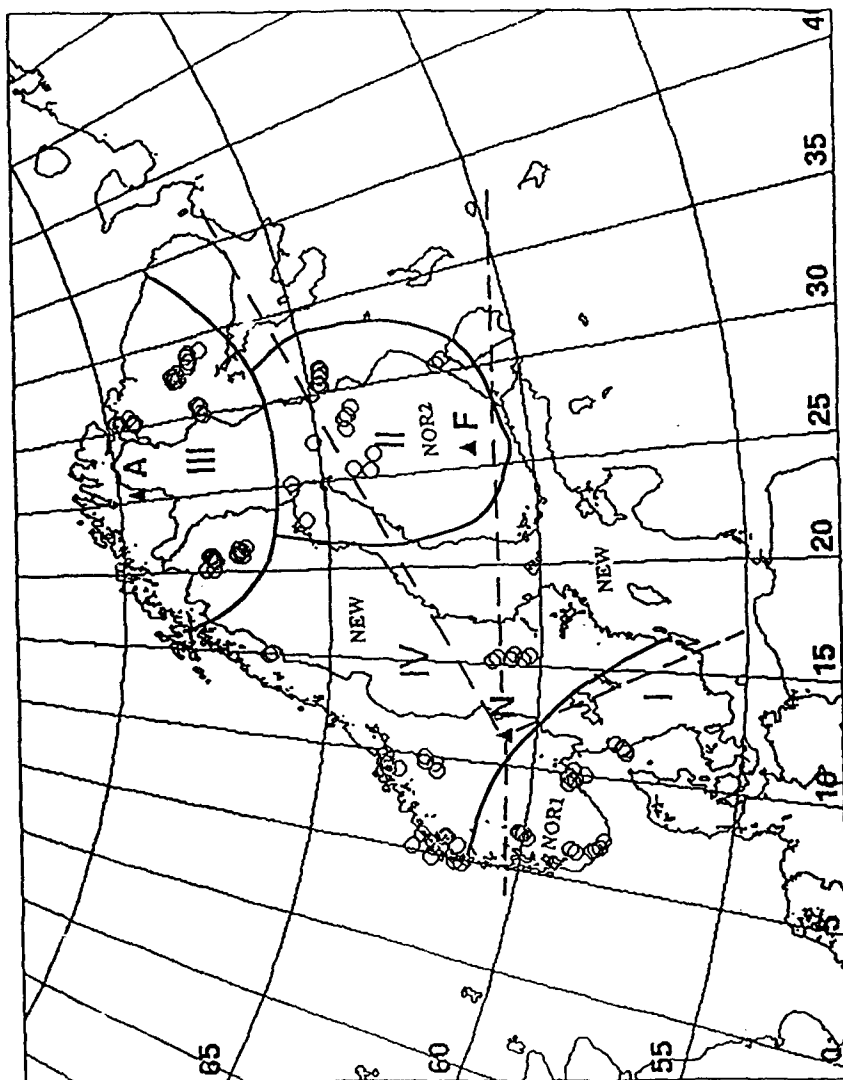


Figure 36: A map of locations of selected events and regional seismic arrays. I, II, III, and IV are groups of events selected for testing. Solid lines are boundaries between the event groups. NEW, NOR1, and NOR2 are zones with different P_n travel-time curves around the NORESS array. Dashed lines are boundaries between azimuth zones with constant P_n travel-time curves. The zones and their travel-time curves have the same designations (see Figure 37).

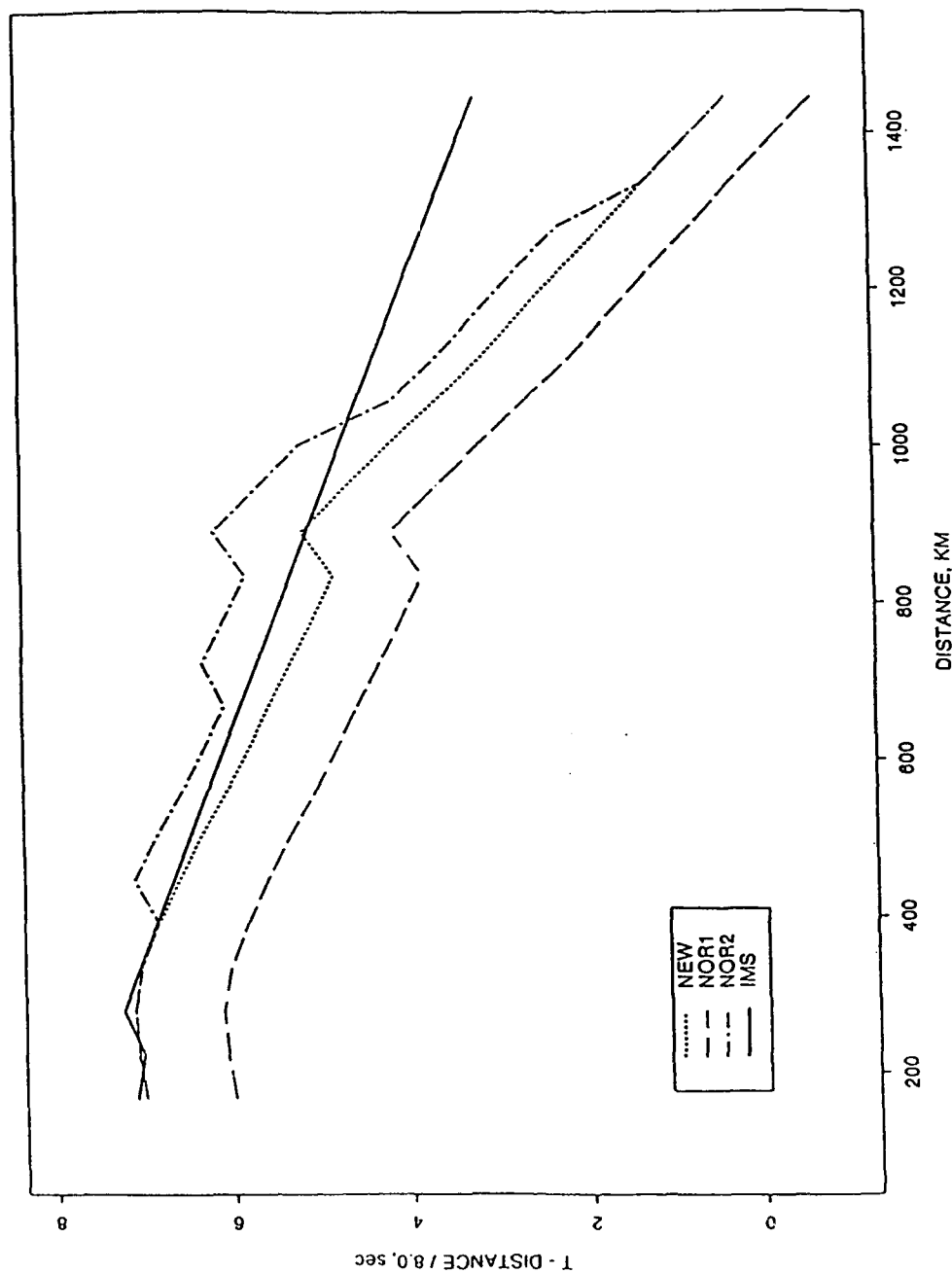


Figure 37: P_n travel-time curves developed for NORESS array. NOR1 and NOR2 are travel-time curves constructed for zones to south and east from NORESS array (see Figure 36). NEW is the new P_n reference travel-time curve used for areas without pronounced residuals from the reference travel-time curve. As comparison, P_n travel-time curve (IMS) used for location events by the IMS system is also shown.

zones and the set of P_n travel-time curves developed for the NORESS array. The zones and their travel-time curves have the same designations (NEW for the reference travel-time curve, NOR1 and NOR2 for zones to the south and east of NORESS, respectively). Similar zones and travel-time curves were constructed for the ARCESS and FINESA arrays.

S_n travel-times were calculated assuming the Poisson's ratio of 0.25. We applied the new P_n and S_n curves based on DSS observations in conjunction with the IMS travel-time tables for P_g and L_g waves to relocate 111 events originally located by the IMS in different areas of Scandinavia and northwestern Russia, at regional and far-regional distances. According to the IMS bulletin, these events were mine explosions.

The IMS algorithm for event locations is described in Bratt and Bache, (1988). The program solves a system of linear equations to minimize a linear approximation of residuals between weighted observed data (P_g , P_n , S_n , and L_g arrival times and azimuths obtained from *f-k analysis* for the NORESS, ARCESS, and FINESA arrays) and estimates computed from a trial hypocenter. The program iterates until convergence criteria are met. Both *a priori* and *a posteriori* information about the data are also used to derive the location confidence bounds.

Figure 36 shows a location map of the events selected for this test. To analyze the results of relocation, we divided the events into four groups. The events in the first and second groups were located in areas of decreased and increased P_n and S_n travel-times, respectively (Figure 35). The events in the third group were located at distances larger than 500-600 km from the NORESS and FINESA arrays. At such distances, the IMS P_n travel-time table is characterized by substantially larger travel-times than DSS data (Figure 33). The events in the fourth (control) group were located at distances less than 500-600 km from all arrays, in a region where the IMS and the new P_n travel-time curves have differences within ± 0.5 sec. We did not anticipate large discrepancies between the IMS original locations and the new ones for events in this area.

The main results of the test are demonstrated in Table 9 and Figure 38. Comparison of the original IMS locations with those determined using path-dependent travel-time curves calibrated by DSS data showed significant differences depending on region, number of stations and designated phases, and event magnitude. The distance between relocated events and those listed in the IMS bulletin and the difference in origin time can be as large as 20 km and ± 3.0 sec, respectively. After relocation, events in areas 1 and 2 were moved mainly to the northeast and the southeast with respect to the IMS locations (Figure 39). Differences between origin times of relocated events and events listed in the IMS bulletin vary mainly within the 1-2 sec and 0.5 -1.3 sec ranges for areas 1 and 2, respectively. As

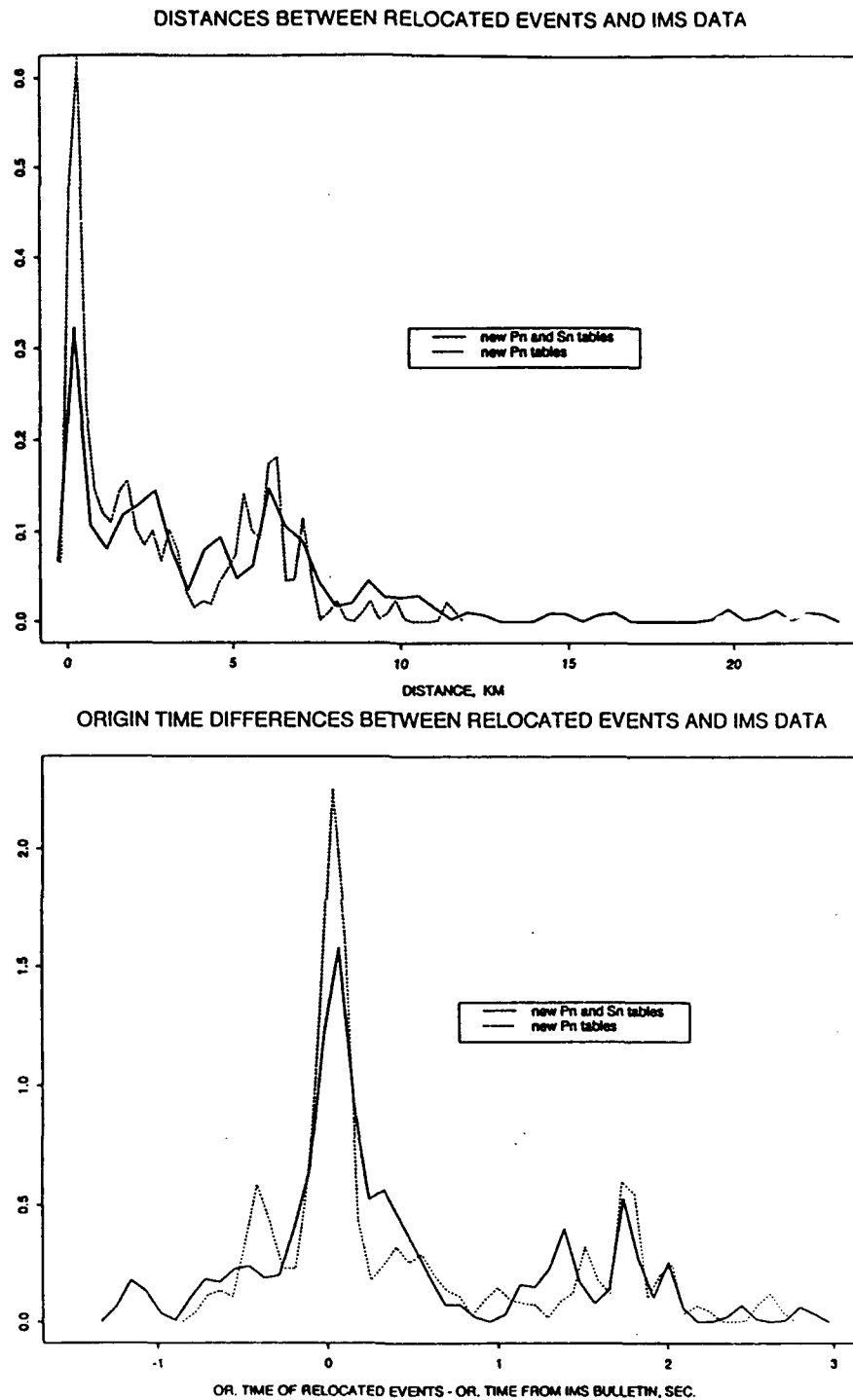


Figure 38: Density plots of distance (top) and origin time differences (bottom) between relocated events and the IMS bulletin for new P_n and S_n (solid lines) and new P_n (dotted lines) travel-time tables inferred from DSS data.

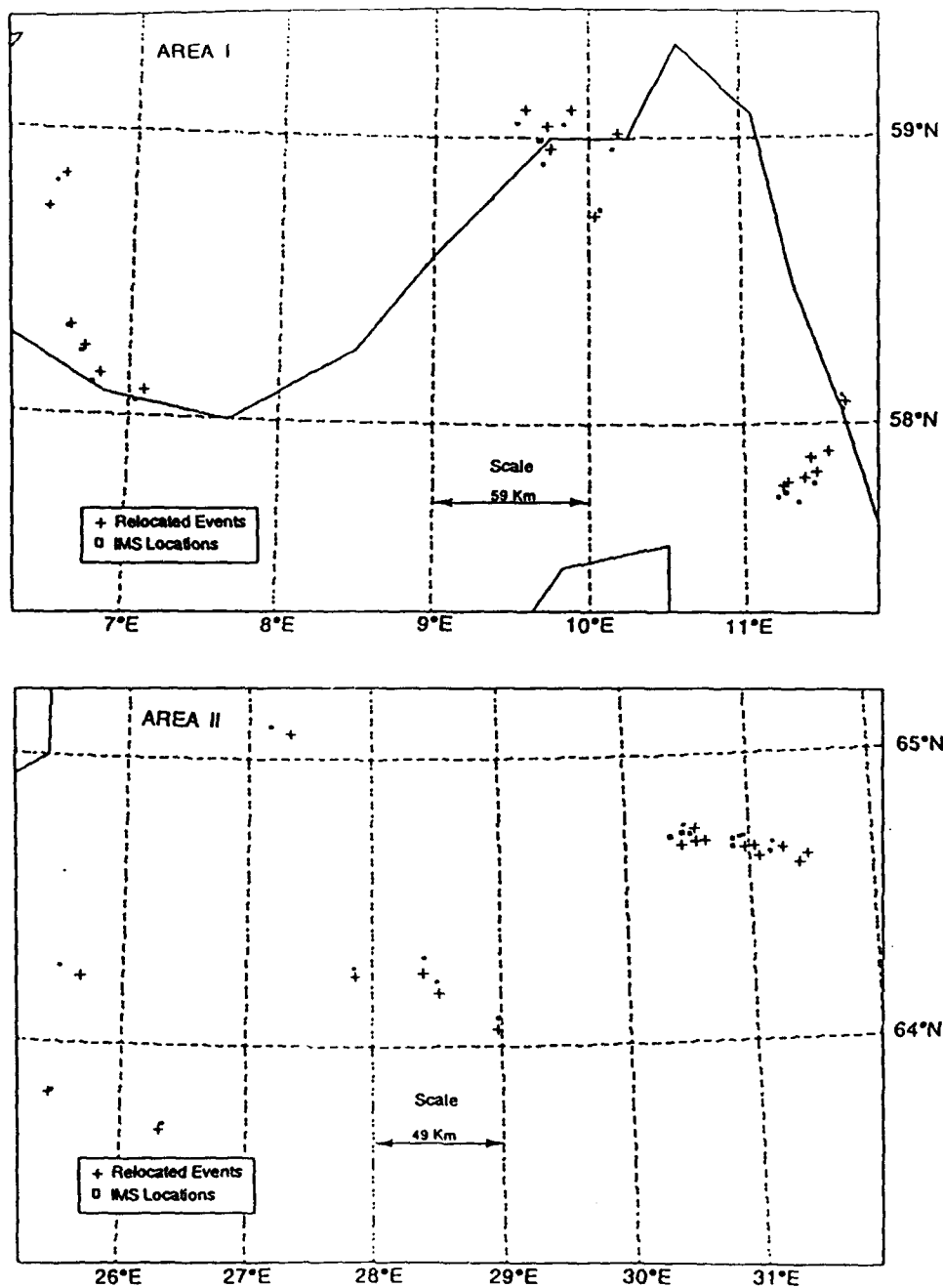


Figure 39: Comparison of locations of relocated events (crosses) and events listed in the IMS bulletin (small squares) for area 1 (top) and area 2 (bottom).

we anticipated, parameters of event locations for the fourth area did not change. The difference between locations and origin times of relocated events and IMS data decreased when we used only the new Pn travel-time table, instead of applying both the new Pn and Sn tables (Figure 38).

For both the IMS event locations and the relocated events we analyzed the semi-minor and semi-major axes of the error ellipse, and the time residuals between the observed and reference travel-times. The dimensions of the confidence ellipsoid depend on both the solution residuals and the *a priori* assumptions about the data variances (Bratt and Bache, 1988). We found that the lengths of axes of the error ellipse were not significantly changed after relocation. Changing Pn and Sn travel-time tables influenced the residuals of Pn , Sn and other regional phases (Pg and Lg). Pn , Pg , and Lg residuals for relocated events in areas 1, 2, and 3, tend to be smaller, while Sn -wave residuals are 2-3 times larger than those of the Pn , Pg , and Lg phases. This could be due to our assumption of a constant value of 0.25 for the Poisson's ratio used for calculating the Sn travel-time tables.

A change in event location is expected when new travel-time curves are applied. We now address the question of whether or not the new locations are closer to the true locations of the events. Because of the lack of master-events with exact location and origin time, we used events listed in the IMS bulletin and located by three arrays as a source of more reliable information. Thirty-one events in the northern part of Scandinavia were relocated with the two arrays NORESS and FINESA, using the IMS travel-time tables for one location and the new Pn tables in conjunction with the IMS travel-time tables for Pg , Sn , and Lg waves for a new location. We compared the distances between the original three-array locations and the two-array locations.

Relocation of events with two arrays created an azimuth bias relative to the original IMS locations. The bias magnitude for the events tested was usually larger for FINESA than for NORESS. Approximately 30% of the selected events had a large azimuth bias (from 2 to 8.5 °; Table 10). The new Pn travel-time table did not improve the locations of these events. However, for azimuth bias within the range of ± 2.0 °, we observed a closer fit to the three-array locations for the two-array locations based on the new Pn travel-time table than with the two-array locations based on the IMS travel-time tables. These events are characterized by negative numbers in the last column of Table 10.

The results of these tests show that the new Pn travel-time tables may improve event locations, but probably cannot compensate for large azimuth estimation errors and phase misidentifications. As a result, we assume that IMS locations based on three-array recordings with reliable azimuth measurements can be improved using path-dependent travel-time curves calibrated by DSS data.

Discussion and Conclusions.

Many factors influence the results of the IMS event locations. Errors originating from random factors (for example, signal to noise ratio and accuracy of measurements) can be eliminated to some extent by statistical methods. Regional variations of seismic signal characteristics such as travel-times and waveform shape, especially the presence of intensive emergent phases in later arrivals, can create a bias in event location which is dependent on ray path. In the codas of the major phases (*Pg*, *Pn*, *Sn*, *Lg*, and *Rg*) used for event location, many large amplitude emergent arrivals (reflected, converted, diffracted and other waves) can be recorded at regional and far-regional distances, and influence phase identification and azimuth estimation. It is well known that these emergent arrivals are related to structural inhomogeneities of the earth crust and upper mantle along the propagation paths, and they contain important information for deep seismic studies. DSS profile observations can help identify the major and emergent phases recorded at arrays, and improve phase identification and azimuth estimation for event location.

This study was directed at the analysis of travel-time anomalies that are usually stable in specific regions. As a first step, we studied regional variations of *Pn*-wave travel-times. It was very important to use reliable data, independent from IMS observations. IMS operates mainly within Scandinavia and northwestern Russia. This territory is covered by a dense network of overlapping and reversed DSS lines. We measured *Pn* first arrival travel-times along all available DSS profiles and constructed a new *Pn* reference travel-time curve from statistical smoothing of the measured travel-times. We also used travel-times of *Pn*-waves recorded by seismological networks up to distances of 1200 km from chemical explosions with exact locations and origin times.

Discrepancies of up to 3 sec at distances greater than 500-600 km were observed between DSS data and reference *Pn* travel-time curves used to locate events for the IMS and Helsinki University seismological bulletins. It is also worth stressing that pronounced *Pn* travel-time anomalies were detected in the Baltic shield. For example, *Pn* first arrival times in southern Norway and Sweden are 2-3 sec earlier at distances of 400-500 km than in southern Finland. Similarly, *Pn-Pg* cross-over distance varies from 130 to 270 km between these two regions. One can anticipate more pronounced *Pn* travel-time variations within the tectonically active regions of Northern Eurasia. The observed *Pn* propagation parameter variations are caused by crustal and upper mantle lateral inhomogeneities. Travel-time tables used for location of seismic events usually do not take into consideration such path effects.

This study investigated the influence of path-calibrated travel-time corrections on regional event locations. With this aim, we developed for the NORESS, ARCESS, and FINESA

arrays a set of Pn travel-time tables, obtained from interpolations and extrapolations of DSS data. Sn travel-times were calculated assuming a Poisson's ratio of 0.25. We used the new Pn , and new Pn and Sn curves, based on DSS observations in conjunction with IMS travel-time tables for Pg and Lg waves to relocate 111 regional events originally located by the IMS in different areas of Scandinavia and northwestern Russia. We also relocated 31 events in northern Scandinavia using two arrays (NORESS and FINESA) and applying new Pn travel-time tables in conjunction with the IMS tables. For this test, the IMS bulletin based on three-array locations was considered a source of more accurate information. Comparison of the original IMS locations with those determined using path-dependent travel-time curves showed significant differences depending on region, number of stations and designated phases, and magnitude. The distance and origin time differences between relocated events and those listed in the IMS bulletin reached 20 km and ± 1.5 sec, respectively. The results of these tests also showed that path-dependent travel-time tables could improve event locations if azimuth estimation and phase identification are sufficiently accurate. In other words, location errors caused by phase misidentification and large errors in azimuth estimation (up to $5-10^\circ$) were not compensated for by the improvement of the travel-time tables.

DSS observations within Scandinavia can also be used to improve reference travel-time curves for Pg -, Sn -, and maybe Lg - waves. Applying new reference travel-time tables in IMS data processing could decrease the bias in event locations and origin times. Then, the IMS data base could be used for further improvement of azimuthal travel-time corrections. A feed-back process could be created between observations and IMS event locations. DSS data can also help improve azimuth estimation and phase identification by contributing to the knowledge base. The results of this study for the Pn -wave show that DSS data can be applied to improve regional event locations and that the derivation of similar corrections for other major regional phases is warranted.

Acknowledgments

The author is grateful to Jerry Carter and Steven Bratt for encouragement and many helpful discussions. Richard Stead and Lori Grant helped test the relocation of events originally located by the IMS, and their contribution to this study is gratefully acknowledged. Anne Suteau-Henson made a valuable contribution in editing the manuscript.

Table 9: Comparison of IMS Locations and Locations Using New P_n and S_n Tables

No.	IMS latitude (°N)	IMS longitude (°E)	New latitude (°N)	New longitude (°E)	Distance between new and IMS solution (km)	Differ. in origin time between new and IMS
1	68.0934	32.5025	68.1543	32.6409	8.92021	0.216
2	69.6288	30.6558	69.6357	30.6237	1.46845	0.343
3	65.1126	27.1754	65.0890	27.3384	8.11337	-0.361
4	67.1370	21.1831	67.1353	21.2347	2.25004	0.161
5	62.2282	9.4066	62.2285	9.4069	0.03692	0.0
6	57.8843	11.4548	57.8822	11.4338	1.2693	0.483
7	58.0966	11.6485	57.9016	11.5518	22.4882	-1.182
8	58.8092	6.4591	58.8341	6.5178	4.3871	1.777
9	61.9222	30.4393	61.8996	30.5005	4.09121	-0.771
10	66.3572	15.1024	66.3610	15.0899	0.70309	0.331
11	67.1863	21.1035	67.1937	21.1446	1.96427	0.354
12	61.7910	6.0582	61.7904	6.0639	0.30857	0.083
13	64.7161	30.3620	64.6864	30.4528	5.46081	-0.396
14	64.0977	28.9755	64.0587	28.9702	4.36242	0.295
15	68.1241	32.7919	68.1875	32.9142	8.72295	0.165
16	67.1515	21.4513	67.1467	21.4954	1.98884	0.125
17	58.9623	10.1540	59.0152	10.1933	6.31968	1.762
18	60.4271	15.4105	60.4270	15.4150	0.24841	-0.065
19	67.0755	21.3497	67.0627	21.3228	1.84896	0.042
20	67.1949	21.0817	67.1912	21.1098	1.28631	0.45
21	64.7310	30.4597	64.6973	30.5713	6.5245	-0.484
22	64.7132	30.9240	64.6769	31.0406	6.89089	-0.486

Table 9: Comparison of IMS Locations and Locations Using New P_n and S_n Tables

No.	IMS latitude (°N)	IMS longitude (°E)	New latitude (°N)	New longitude (°E)	Distance between new and IMS solution (km)	Differ. in origin time between new and IMS
23	67.5718	30.1084	67.5848	30.1093	1.45299	0.307
24	67.6350	33.9390	67.6882	34.1329	10.1619	0.2
25	61.7527	6.0147	61.7522	6.0203	0.30145	0.081
26	64.7149	30.9548	64.6659	31.2733	16.1776	-1.176
27	64.6787	30.8695	64.6372	31.0780	11.0018	-0.708
28	60.7126	15.3269	60.7129	15.3287	0.10397	-0.02
29	58.9926	9.6843	59.0416	9.7337	6.16034	1.719
30	62.0699	4.8483	62.0698	4.8515	0.16791	0.035
31	65.7624	25.0912	65.7551	25.1433	2.52714	0.037
32	60.2582	15.5114	60.2577	15.5181	0.37562	-0.101
33	58.0513	7.0446	58.0925	7.1066	5.87657	1.568
34	58.7170	6.4150	58.7170	6.4150	0.0	0.0
35	62.2357	9.2752	62.2360	9.2756	0.03936	0.0
36	64.2675	25.4736	64.2333	25.6466	9.23	-0.211
37	67.3998	34.0420	67.4087	34.0981	2.60775	0.141
38	69.3242	30.4146	69.3277	30.3644	2.02064	0.553
39	63.3944	9.3902	63.3923	9.3928	0.26820	0.082
40	62.5595	5.2670	62.5592	5.2696	0.13811	0.033
41	62.3782	5.9031	62.3777	5.9051	0.11776	0.036
42	58.9919	9.6734	59.0408	9.7230	6.156	1.718
43	62.5527	10.0009	62.5555	9.9990	0.32747	-0.084
44	61.8459	5.9770	61.8451	5.9813	0.24374	0.068

Table 9: Comparison of IMS Locations and Locations Using New P_n and S_n Tables

No.	IMS latitude (°N)	IMS longitude (°E)	New latitude (°N)	New longitude (°E)	Distance between new and IMS solution (km)	Differ. in origin time between new and IMS
45	59.9816	6.7664	60.0034	6.8879	7.21325	2.022
46	61.0256	15.4144	61.0258	15.4179	0.19081	-0.053
47	60.0782	6.7152	60.0975	6.8384	7.1959	2.017
48	58.9098	9.7033	58.9594	9.7504	6.16301	1.731
49	59.0510	9.5357	59.0987	9.5894	6.15	1.728
50	64.2250	28.5060	64.1833	28.5204	4.70868	-0.084
51	64.7254	30.5257	64.7014	30.6442	6.26208	-0.2
52	62.5322	9.7730	62.5350	9.7701	0.34637	-0.099
53	63.3740	9.0875	63.3719	9.0896	0.25697	0.072
54	61.4889	5.7356	61.4884	5.7398	0.23095	0.066
55	60.1279	6.7992	60.1459	6.9207	7.05324	1.978
56	63.4953	9.3970	63.4936	9.3985	0.20393	0.058
57	69.2116	30.3971	69.2696	30.3918	6.48536	0.608
58	59.0487	9.8358	59.0994	9.8844	6.30667	1.77
59	63.4856	9.8652	63.4832	9.8667	0.27832	0.078
60	60.6127	15.5897	60.6124	15.5962	0.35805	-0.101
61	61.1366	15.2442	61.1367	15.2452	0.05504	-0.015
62	67.6512	33.8547	67.7424	33.8741	10.223	1.184
63	62.3667	9.6220	62.2941	9.7031	9.13192	2.819
64	61.4995	4.6911	61.4898	4.8099	6.42898	1.798
65	63.0640	8.8438	63.1487	9.2187	21.1852	0.108
66	57.7467	11.2193	57.7843	11.2535	4.66209	1.43

Table 9: Comparison of IMS Locations and Locations Using New P_n and S_n Tables

No.	IMS latitude (°N)	IMS longitude (°E)	New latitude (°N)	New longitude (°E)	Distance between new and IMS solution (km)	Differ. in origin value between new and IMS
67	57.7629	11.2689	57.7991	11.2851	4.15059	1.446
68	57.7941	11.4519	57.8340	11.4673	4.54289	1.39
69	61.8100	30.6573	61.7911	30.7275	4.26601	-0.745
70	64.2717	27.8544	64.2432	27.8667	3.23779	0.114
71	68.0319	32.9389	68.0778	33.0592	7.18256	-0.241
72	58.2182	6.6725	58.2347	6.7012	2.49756	1.377
73	67.7167	20.7320	67.7346	20.7218	2.04633	-0.606
74	61.8655	5.4701	61.8654	5.4730	0.15323	0.040
75	63.7235	26.3352	63.7017	26.3147	2.63722	-0.235
76	67.0190	21.5718	66.9961	21.5820	2.59686	0.437
77	67.6268	30.4870	67.6552	30.5849	5.23597	0.183
78	67.8719	20.9856	67.8746	20.9925	0.41887	-0.016
79	64.3083	28.4076	64.2552	28.3962	5.95496	-0.015
80	67.7283	33.5455	67.7392	33.5471	1.21992	0.22
81	67.8038	20.8545	67.8053	20.8600	0.28655	0.08
82	58.2967	6.5724	58.3084	6.5936	1.80348	1.286
83	69.2867	30.3752	69.3053	30.2395	5.7547	1.312
84	64.6549	31.1682	64.6112	31.4012	12.181	-1.105
85	61.3251	4.7509	61.3182	4.8699	6.42932	1.797
86	68.0854	32.8920	68.1089	32.8732	2.74052	0.322
87	59.9061	6.5654	59.9286	6.6829	7.04467	1.967
88	57.7294	11.3507	57.8121	11.3890	9.50076	2.434

Table 9: Comparison of IMS Locations and Locations Using New P_n and S_n Tables

No.	IMS latitude (°N)	IMS longitude (°E)	New latitude (°N)	New longitude (°E)	Distance between new and IMS solution (km)	Differ. in origin time between new and IMS
89	58.0512	11.6504	58.0740	11.6658	2.70094	1.109
90	67.9581	20.1437	67.9624	20.1573	0.74612	0.026
91	64.7029	30.8697	64.6751	30.9634	5.44969	-0.139
92	65.4978	22.8995	65.4896	22.9519	2.59719	0.107
93	67.6858	30.6084	67.7192	30.7642	7.59175	0.004
94	67.7537	20.1562	67.7616	20.1718	1.10239	0.283
95	68.0300	32.3409	68.1924	32.5309	19.8	0.631
96	67.6805	33.4909	67.6677	33.5583	3.20065	-0.552
97	64.7586	30.4693	64.7425	30.5658	4.94119	0.074
98	58.1097	6.7534	58.1416	6.8054	4.69789	1.37
99	67.7648	20.8015	67.7759	20.8375	1.96416	0.468
100	67.5965	30.2999	67.6594	30.2490	7.35424	1.393
101	63.8302	25.4430	63.8216	25.4146	1.69806	-0.197
102	68.0522	32.5634	68.0755	32.5684	2.61176	0.374
103	69.3469	30.4185	69.3492	30.3755	1.71563	0.43
104	64.6912	31.1872	64.6422	31.4717	14.6696	-1.043
105	58.7476	10.0722	58.7247	10.0383	3.22333	1.164
106	67.7713	20.9327	67.7906	20.9772	2.86217	0.781
107	66.4619	15.0951	66.4745	15.0209	3.59951	0.148
108	69.6892	30.5212	69.7399	30.5857	6.19392	-0.42
109	67.0742	20.9543	67.0679	21.0268	3.23623	0.278
110	67.7191	33.0275	67.7502	33.2606	10.4713	-0.592

Table 9: Comparison of IMS Locations and Locations Using New P_n and S_n Tables

No.	IMS latitude (°N)	IMS longitude (°E)	New latitude (°N)	New longitude (°E)	Distance between new and IMS solution (km)	Differ. in origin time between new and IMS
111	69.4016	30.8897	69.4144	30.8449	2.26994	0.486

Table 10: Comparison of IMS bulletin with two-array (NORESS, FINESA) locations

1	2	3	4	5	6	7	8	9	10	11	12
1.	68.09	32.50	1292.45	802.24	41.78	19.54	-0.20	0.97	0.65	2.04	1.86
2.	69.63	30.66	1326.95	937.74	33.68	10.99	-0.26	4.15	0.33	4.87	0.55
3.	65.11	27.18	929.91	413.26	51.64	7.20	0.03	1.04	-0.01	1.55	4.82
4.	67.14	21.18	855.36	678.06	29.27	341.71	-1.40	1.26	-1.33	1.29	-0.80
5.	66.36	15.10	651.98	767.60	14.20	320.30	-1.20	-0.14	-1.10	-0.16	-1.27
6.	67.19	21.10	857.61	684.49	28.86	341.63	-0.78	-0.52	-0.73	-0.51	-0.79
7.	68.12	32.79	1304.67	810.60	41.91	20.20	-1.46	-1.45	-0.05	-0.39	-27.04
8	67.15	21.45	863.86	675.17	29.82	342.68	-0.83	-0.88	-0.62	-0.80	-2.54
9	67.08	21.35	854.46	668.99	29.94	342.06	-1.07	-1.34	-1.02	-1.20	-1.38
10.	67.19	21.08	857.80	685.75	28.77	341.58	0.40	1.26	0.45	1.13	-1.63
11.	67.57	30.11	1175.81	710.87	41.75	14.02	0.83	2.38	1.35	3.31	10.67
12.	67.63	33.94	1323.15	786.52	45.01	25.16	0.19	0.93	0.70	1.31	0.51
13.	65.76	25.09	879.98	484.62	44.63	354.64	-0.75	0.14	-0.71	0.43	1.09
14.	69.32	30.41	1298.35	902.43	34.59	10.97	1.53	3.92	2.84	6.29	35.99
15.	69.22	30.40	1290.48	890.74	34.99	11.13	-0.71	-1.03	-0.38	-0.93	-1.77
16.	67.65	33.86	1321.01	786.49	44.87	24.88	3.61	5.17	3.92	5.04	8.10
17.	68.04	32.97	1306.49	805.27	42.44	20.98	-0.15	-0.37	0.24	-0.01	4.27

Table 10: Comparison of IMS bulletin with two-array (NORESS, FINESA) locations

1	2	3	4	5	6	7	8	9	10	11	12
18.	67.73	20.75	897.94	746.29	25.74	342.37	-1.79	1.54	-1.78	1.53	-0.36
19.	67.02	21.57	855.67	659.43	30.72	342.63	-2.49	0.28	-2.25	0.19	-5.16
20.	67.63	30.48	1192.67	721.66	41.90	15.09	0.36	1.10	1.06	2.43	15.95
21.	67.87	21.03	917.36	756.32	25.80	343.65	0.25	-0.75	0.25	-0.75	-0.01
22.	65.50	22.90	780.46	479.45	42.24	342.10	0.63	-1.37	0.62	-1.06	-2.25
23.	67.68	30.60	1200.19	729.31	41.76	15.29	0.07	0.18	0.44	0.70	7.29
24.	67.76	20.16	886.87	759.07	24.28	340.72	-1.97	-1.80	-1.97	-1.86	0.23
25.	68.03	32.37	1284.34	793.92	41.92	19.37	5.80	8.67	5.80	7.74	-1.59
26.	67.60	30.28	1183.62	715.75	41.82	14.53	-1.24	-2.16	-1.24	-2.66	5.20
27.	69.35	30.42	1300.03	904.89	34.51	10.94	-0.21	0.03	0.91	2.08	25.63
28.	66.43	15.11	659.68	772.50	14.02	320.77	-0.68	0.11	-0.60	0.09	-1.14
29.	69.69	30.52	1327.12	942.87	33.31	10.57	-1.11	-0.52	0.74	0.77	-16.18
30.	67.07	20.96	843.73	675.51	29.04	340.71	-0.54	-0.44	-0.31	-0.27	-3.47
31.	67.72	33.01	1291.35	774.25	43.89	22.31	-0.02	-1.11	0.23	-0.69	-1.09

- 1 - Event number;
- 2 - IMS latitude ($^{\circ}$ N);
- 3 - IMS longitude ($^{\circ}$ E);
- 4 - IMS distance to NORESS (km);
- 5 - IMS distance to FINESA (km);
- 6 - IMS azimuth from NORESS ($^{\circ}$);
- 7 - IMS azimuth from FINESA ($^{\circ}$);
- 8 - Azimuth bias of two-array locations from NORESS for IMS tables ($^{\circ}$);
- 9 - Azimuth bias of two-array locations from FINESA for IMS tables ($^{\circ}$);
- 10 - Azimuth bias of two-array locations from NORESS for new P_n tables ($^{\circ}$);
- 11 - Azimuth bias of two-array locations from FINESA for new P_n tables ($^{\circ}$);
- 12 - Difference of distances between IMS and two-array locations, (new P_n travel-time table) - (IMS travel-time table) (km).

References

- Bache, T.C., S.R. Bratt, J. Wang, R.M. Fung, C. Kobryn, and J.M. Given (1990). The intelligent monitoring system, *Bull. Seism. Soc. Am.* **80**, 1833-1851.
- Bath, M. (1981). Average crustal travel-times in Sweden re-examined, *Pure Appl. Geophys.* **119**, 1116-1124.
- Berzon, I.S. (1977). Seismic exploration of vertically-layered medium of basement, *Nedra*, Moscow, 320 (in Russian).
- Bratt, S.R. and T.C. Bache (1988). Locating events with a sparse network of regional arrays, *Bull. Seism. Soc. Am.* **78**, 780-798.
- Bratt, S.R., H.J. Swanger, R.J. Stead, F. Ryall, and T.C. Bache (1990). Initial results from the Intelligent Monitoring System, *Bull. Seism. Soc. Am.* **80**, 1852-1873.
- Cassell, B.R., S. Mykkeltveit, R. Kanestrom, and E.S. Husebye (1983). A North sea-southern Norway seismic crustal profile, *Geophys. J. R. astr. Soc.* **72**, 733-753.
- Dahlman, O. (1967). On Scandinavian crustal travel-times, *The Research Institute of National Defense*, Stockholm, 9.
- EUGENO-S Working Group (1988). Crustal structure and tectonic evolution of the transition between the Baltic Shield and the North German Caledonides, *Tectonophysics* **150**, 253-348.
- Guggisberg, B. (1986). Eine zweidimensionale refraktionsseismische interpretation der Geschwindigkeits - Tiefen - Struktur des oberen Erdmantels unter dem Fennoskandischen schild (Projekt FENNOLORA), *Diss. ETH Nr. 7945*, Zurich, 199.
- Hauser F. and R. Stangl (1990). The structure of the crust and lithosphere in Fennoscandia derived from a joint interpretation of *P*- and *S*-wave data of the FENNOLORA refraction seismic profile, in *Proceedings of the sixth workshop on the European geotraverse project*, 71-92.
- Husebye, E.S., J. Hovland, A. Christoffersson, K. Astrom, R. Slunga, and C.E. Lund (1986). Tomographical mapping of the lithosphere and asthenosphere beneath southern Scandinavia and adjacent areas, *Tectonophysics* **128**, 229-250.
- Imaging and understanding the lithosphere of Scandinavia and Iceland (1991). *Tectonophysics* **189**, 344.
- Kinck, J.J., E.S. Husebye, and F.R. Larson (1990). The Moho depth distribution in Fennoscandia and the regional tectonic evolution from Archean to Permian times, *Manuscript*, Dept. of Geology, Oslo University, 1-57.
- Korhonen, H., I.P. Kosminskaya, I. Azbel, N. Sharov, V. Zagorodny, and U. Luosto (1990). Comparison of crustal structure along DSS profiles in SE Fennoscandia, *Geophys. J. Int.* **103** 1, 157-162.
- Lund, C.E. (1979). The fine structure of the lower lithosphere underneath the Blue Road

- profile in northern Scandinavia, *Tectonophysics* **56**, 111-122.
- Luosto, U., E. Lanne, H. Korhonen, A. Guterh, M. Grad, R. Materzok, and E. Perchuc (1984). Deep structure of the Earth's crust on the SVEKA profile in central Finland, *Annales Geophysicae* **2**, 5, 559-570.
- Luosto, U., T. Tiira, H. Korhonen, I. Azbel, V. Burmin, A. Buyanov, I. Kosminskaya, V. Ionkis, and N. Sharov (1990). Crust and upper mantle structure along the DSS Baltic profile in SE Finland, *Geophys J. Int. Geophys.* **52**, 119-130.
- Luosto, U. (1991). Moho map of the Fennoscandia Shield based on seismic refraction data, in *Structure and dynamics of the Fennoscandian lithosphere*, Helsinki, 43-50.
- Mereu, R.F., S. Mykkeltveit, and E.S. Husebye (1983). Fennolora recordings at NOR-SAR, *J. Geophys.* **52**, 119-130.
- Mykkeltveit, S., F. Ringdal, T. Kvaerna, and R.W. Alewine (1990). Application of regional arrays in seismic verification research, *Bull. Seism. Soc. Am.* **80**, 1777-1800.
- Porkka, M.T., H. Korhonen, and K. Saviaro (1972). Study of P-wave velocity below Moho, *Pure and Applied Geophysics* **97**, 51-56.
- Proceedings of the colloquium on deep seismic sounding in northern Europe (1971). *The Swedish natural science research council*, Stockholm, 98.
- Proceedings of the sixth workshop on the European geotraverse project (1990). *The Commission of the European communities*, 457.
- Ryaboy, V. (1989). Upper mantle structure studies by explosion seismology in the USSR, DELPHIC, 154.
- Ryaboy, V. (1990). Upper mantle structure along a profile from Oslo (NORESS) to Helsinki to Leningrad, *Bull. Seism. Soc. Am.* **80**, 21194-2213.
- Sellevoll, M.A., P. Pomeroy (1968). A travel-time study for Fennoscandia, *Arbok for Universitetet i Bergen, Mat.-Naturv. Serie* **9**, 1-29.
- Sharov, N.V. (1991). Lithosphere of the Baltic shield according to seismic data (1991), in *Structure and dynamics of the Fennoscandian lithosphere*, Helsinki, 87-96.
- Shore, M.J. (1982). Seismic travel-time anomalies from events in the western Soviet Union, *Bull. Seism. Soc. Am.* **72**, 113-128.
- Stangl, R. (1990). Die struktur der lithosphare in Schweden, abgeleitet aus einer gemeinsameninterpretation der P- und S- wellen registrierungen auf dem FENNOLORA profil. *Phd. Thesis*, University of Karlsruhe, 154.
- Structure and dynamics of the Fennoscandian lithosphere (1991). *Institute of seismology of Helsinki university*, 120.
- Study of the deep structure beneath the eastern part of the Baltic shield and adjacent water areas by seismic methods (1986). *Kola branch Geological institute of the Soviet Acad-*

emy of Sciences, Apatity, 116.

Suteau-Henson, A. (1991). Three-component analysis of regional phases at NORESS and ARCESS: polarization and phase identification, *Bull. Seism. Soc. Am.* **81**, 2419-2440.

The European geotraverse (1989). Part 5: The Polar profile, *Tectonophysics* **162**, 171.

Vogfjord, K.S. and C.A. Langston (1990). Analysis of regional events recorded at NORESS, *Bull. Seism. Soc. Am.* **80**, 2016-2031.

The Norilsk DSS Profile in Northern Siberia: an Analysis of the 2-d Crustal Velocity Section Constructed by Soviet Seismologists

V. Ryaboy, H. Benz, J. Unger, and W. Leith

Introduction

Under an agreement between the Ministry of Geology of the USSR and the US Geological Survey, data from Soviet and US deep seismic sounding (DSS) profiles were exchanged in early 1991. The Soviet profile is nearly 230 km long, and is located in Northern Siberia, near Norilsk, in a region that has been designated as a site for a joint US/USSR seismic station. The accurate characterization of the crust and upper mantle in this region is essential for understanding details of seismic signal propagation recorded at the new station. The objective of this research is to evaluate the Soviet interpretation of the Norilsk DSS profile using theoretical travel times and synthetic seismograms from ray tracing.

Geological and Geophysical Background

The Norilsk profile trends NW-SE at the border between the north western part of the Precambrian Siberian platform and the Paleozoic West-Siberian platform plate within the Norilsk uplift (Figure 40, line 1-1). The Norilsk uplift is characterized by a complex geological structure, due partly to the presence of wide-spread trap intrusions within the sedimentary layers and deep faults. This region has been studied extensively because it is rich in a variety of ore deposits. The first crustal studies in Northern Siberia were based on recordings of mine explosions (Figure 40, line 4-4), (Tuezov, 1965), but several DSS lines have crossed the area since then. The crustal and upper mantle velocity sections were published for two long-range profiles. The Dikson-Khilok profile crossing the Siberian platform from north to south (Figure 40, line 2-2) is located 50-100 km east of the Norilsk profile (Egorkin et al., 1987), and the Vorkuta-Tixie profile (Figure 40, line 3-3) stretching from west to east in the northern areas of Siberia (Egorkin et al., 1980) crosses the northern part of the Norilsk profile. A joint interpretation of the geological and geophysical data, including DSS observations, was made for this region and indicates that the crustal thickness in the Norilsk region is less than 40 km, and that the depth to the basement varies from 5 to 10 km (Grichin et al., 1989).

The unpublished Norilsk profile data set consists of three-component analog field recordings from nine reversed and overlapping shots. Recordings of seismic waves were collected from five shot points within the profile and four off-end shots (Figure 41). The

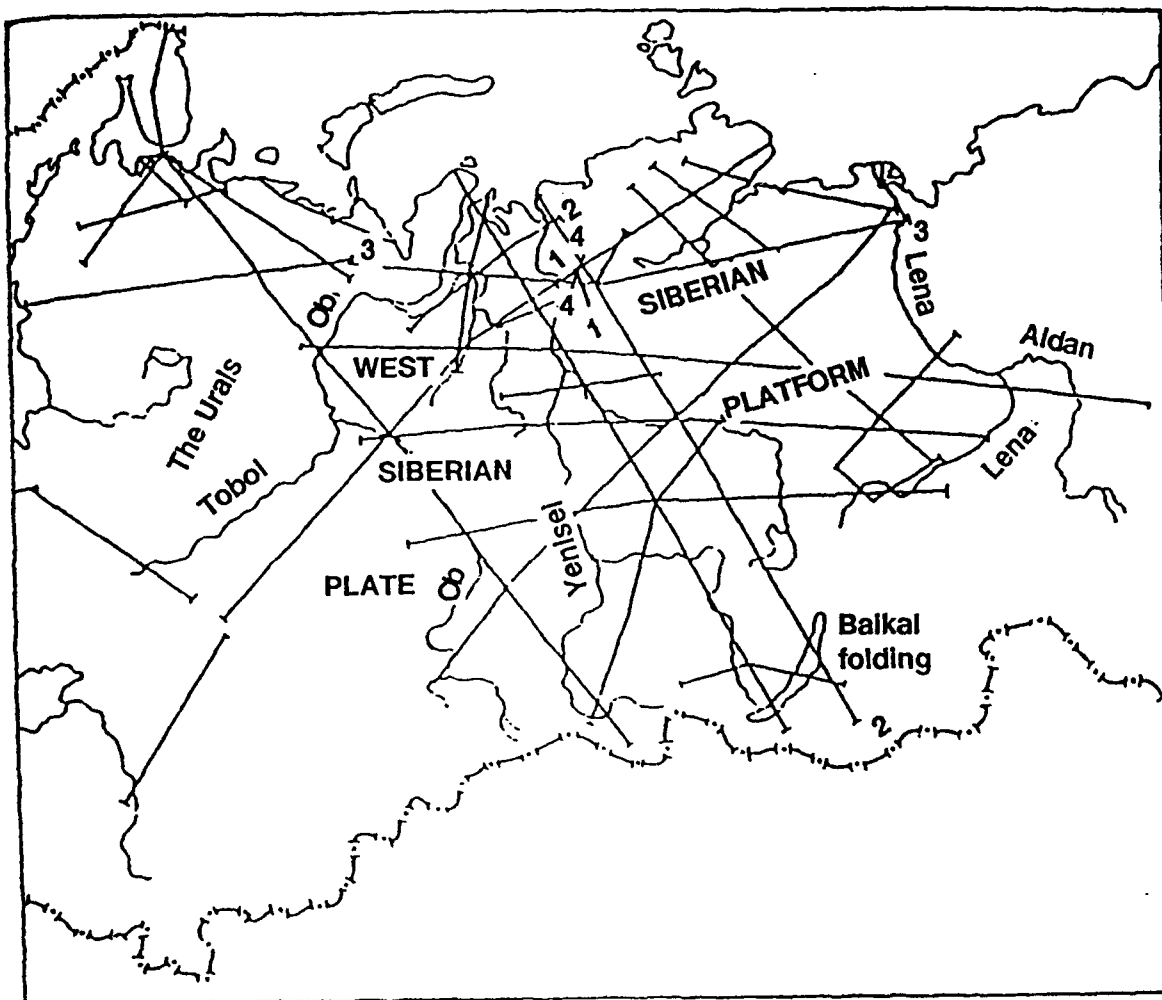


Figure 40: Location map of the DSS profiles in Northern Siberia and neighboring regions: 1-1 -- Norilsk profile, 2-2 -- Dikson-Khilok profile, 3-3 -- Vorkuta-Tixsie profile, 4-4 -- a profile based on recordings of mine explosions. Adapted from Egorkin et al.,(1989) with additions.

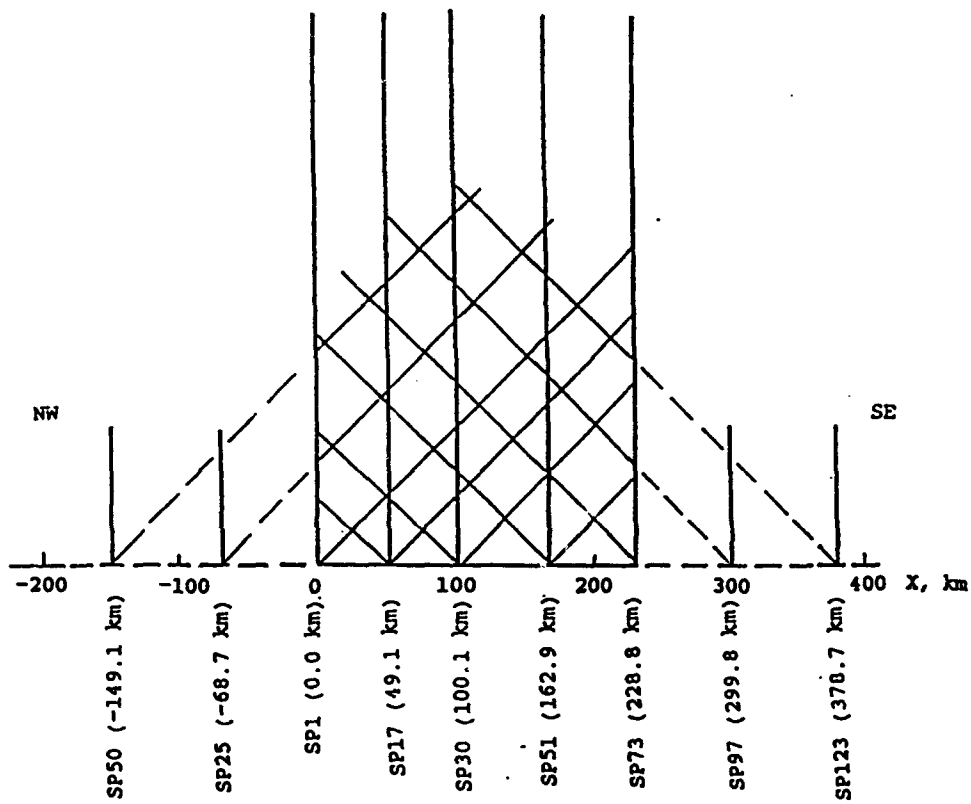


Figure 41: Field observation system for the Norilsk DSS profile.

explosions were recorded up to distances of 250-280 km for off-end shots, and 180-230 km for shots located within the profile. Station spacing varied from 3 to 5 km and the shot spacing averaged 40 km. Three-component portable analog seismic stations provided records in the 1.0-20.0 Hz frequency range. This system of field observations was designed to detect and correlate refracted, reflected, and converted body waves. The analog waveforms were digitized in the USSR at 50 samples per second.

Soviet seismologists interpreted the wave recordings as a complex, two-dimensional (2D) velocity model with crustal thickness varying from 42 to 48 km and high velocities (6.8 km/s) at depths as shallow as 13-15 km (Figure 42). Their velocity section is characterized by a number of laterally inhomogeneous layers consisting of different size blocks with high and low velocities. The blocks are separated by vertical or subvertical boundaries that were interpreted from reflected and converted waves or interpolated with the help of other criteria developed in the USSR (Egorkin et al., 1989). The linear dimensions of the blocks vary from approximately 10-20 to 50-100 km.

Analysis of the Crustal Velocity Model for the Norilsk DSS Profile

Crustal and upper mantle refracted waves were recorded on the Norilsk profile. Apparent velocities vary considerably: 2.0-5.0 (sedimentary layers), 6.0-6.5 (Pg), and 8.0-8.2 (Pn) km/s, respectively. The Pn wave is observed beyond 150-160 km from shot points and is typically weak. Reflected waves from crustal boundaries and the Moho (PMP) were recorded as secondary arrivals.

In order to substantiate the crustal velocity model constructed for the Norilsk profile by Soviet seismologists, we calculated theoretical travel-time curves and ray synthetic seismograms for a generalized version of their model. We attempted to accurately parametrize this 2D velocity model (Figure 42) by using a series of 11 laterally-heterogeneous layers, with each layer approximating a layer in the Soviet model (Figure 43). We made calculations for the refracted and reflected P-waves for three reversed and overlapping shot points (SP1, SP17, SP73), using the program Ray84 of J. Leutgert (USGS, Menlo Park), and compared these results with the observed data (Figures 44, 45, and 46).

According to the model, a complex group of arrivals from waves refracted in layers of the upper and middle crust up to depths of 20-25 km (Pg) should be recorded as the first arrivals from 40 to 230 km. Changes in the waveform characteristics of the first arrivals, a break and offset to later time in the travel time curves, and zones of increased and decreased amplitudes caused by vertical and lateral velocity inhomogeneities are observed in the synthetic record sections (Figures 45 and 46). At distances greater than 230 km, (not shown) Pn wave refracted in the upper mantle is the first arrival in the syn-

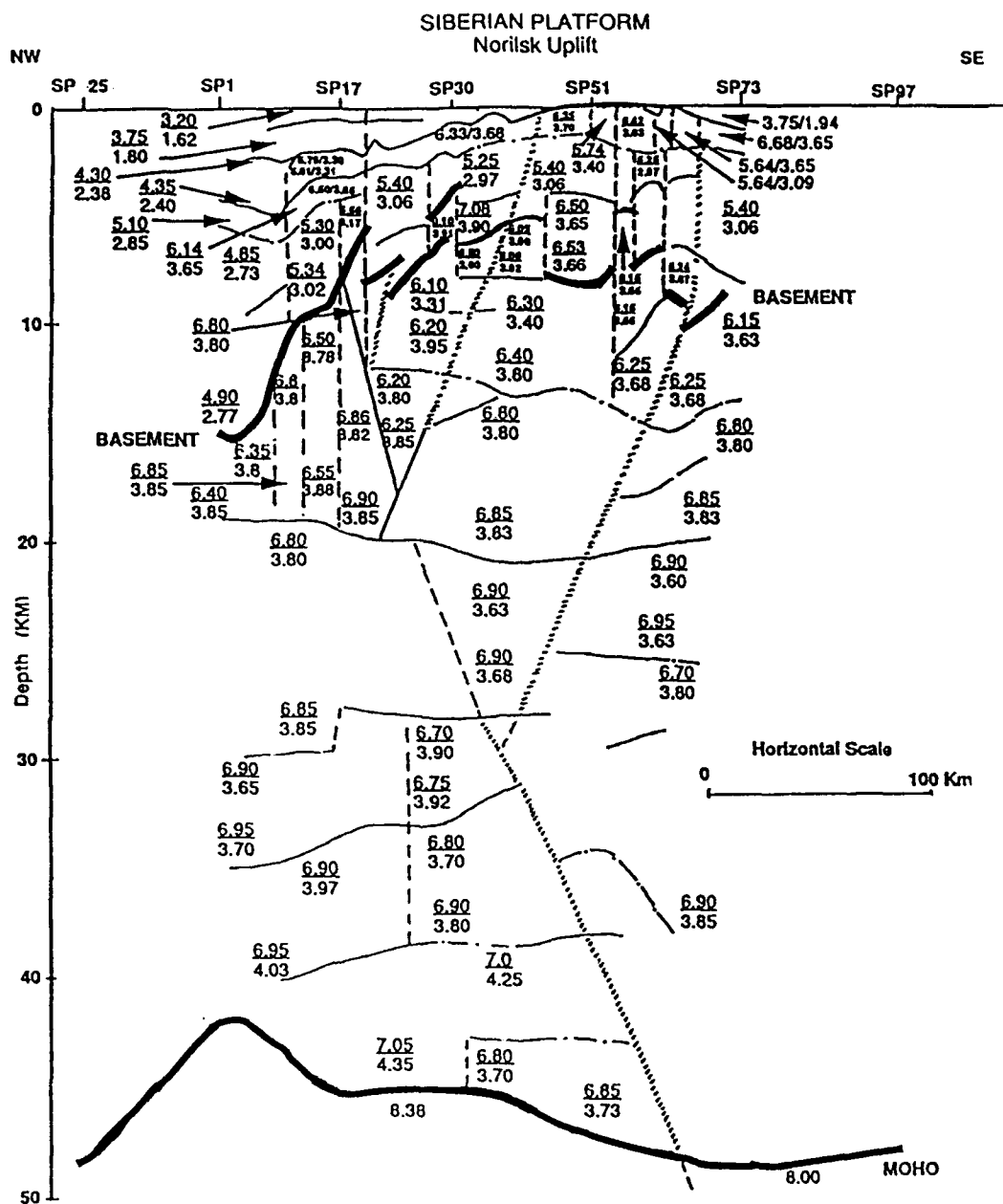


Figure 42: Crustal velocity section constructed by Soviet seismologists (A.V. Egorkin, L.N. Solodilov *et al.*) for the Norilsk profile. Numbers are velocities of P- and S-wave in km/s (above and below lines, respectively). Vertical exaggeration is 10:1.

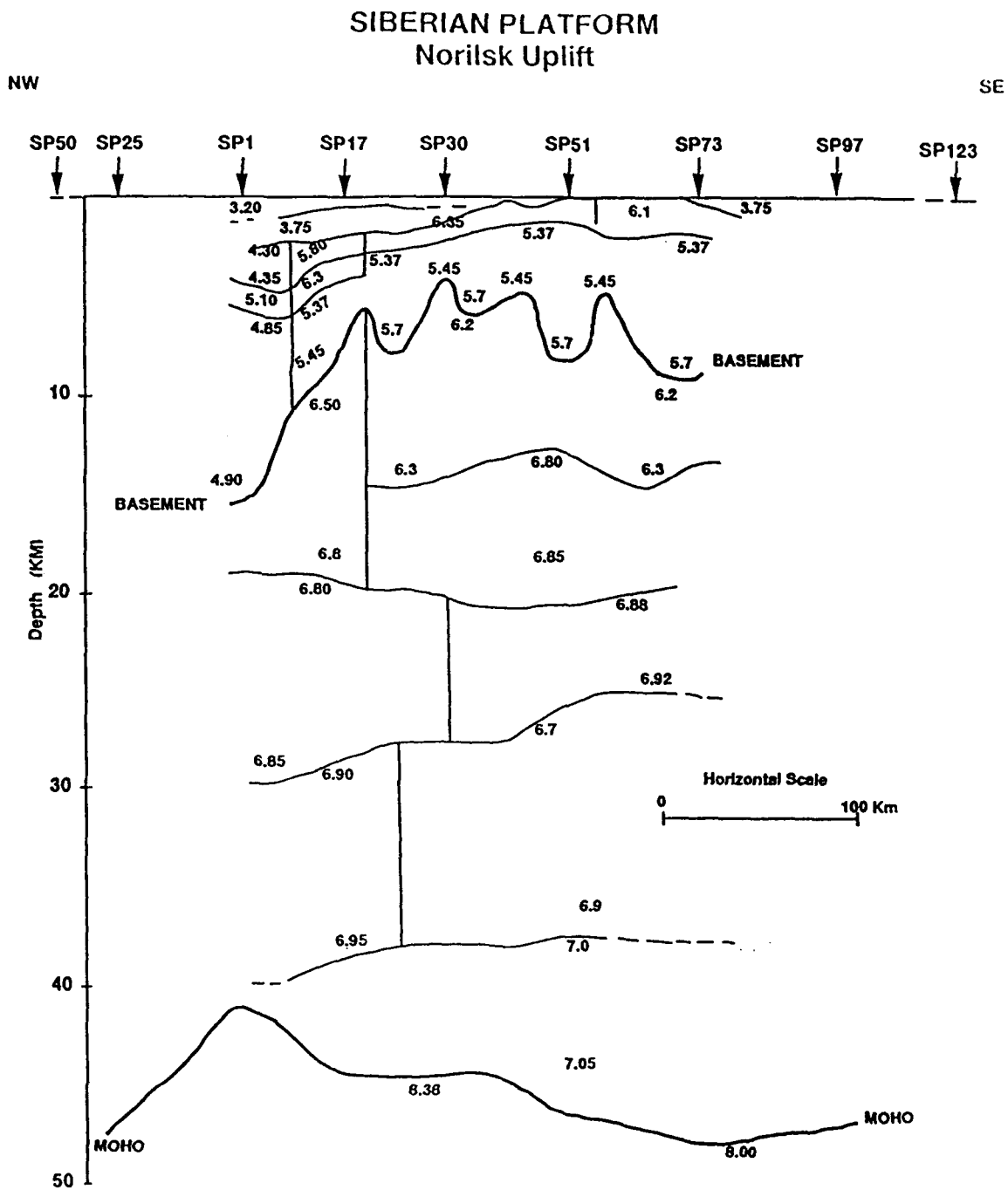


Figure 43: Two-dimensional crustal velocity model used for calculations of theoretical travel-time curves and synthetic seismograms. The model is a generalized version of the crustal velocity section constructed by Soviet seismologists for the Norilsk DSS profile (Figure 42). Numbers are P-wave velocities (in km/s) within crustal layers and blocks, and beneath the Moho.

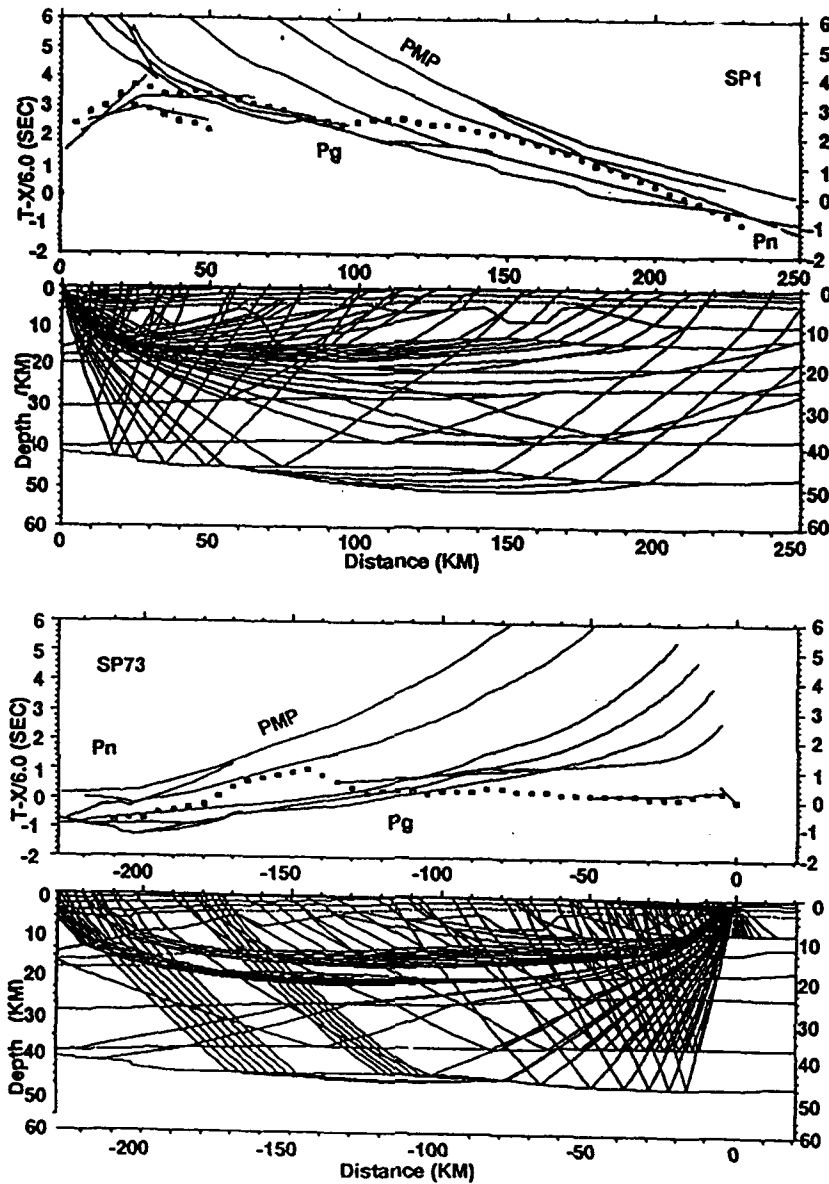


Figure 44: Two-dimensional ray tracing for reversed and overlapping shot points SP1 (top), SP73 (bottom). Open squares denote observed travel-times for first arrivals. Theoretical travel-time curves of reflected and refracted waves and ray paths are shown in solid lines.

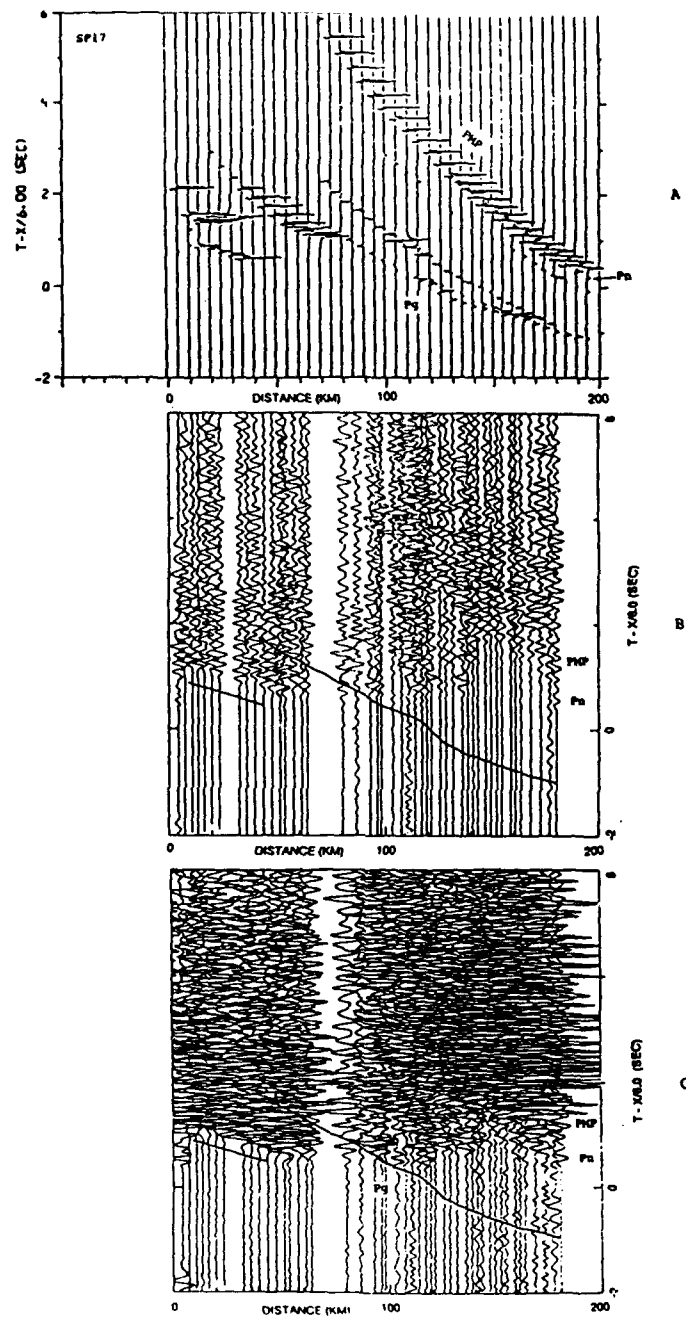


Figure 45: Synthetic (A) and observed (B and C) record sections of P-waves for SP17. Recordings (B and C) are trace-normalized and bandpass filtered between 3 and 10 Hz. Seismic wave amplitudes for (C) were increased relative to (B) to search for low amplitude arrivals. Solid lines on record sections (B) and (C) denote theoretical travel-time curves for first arrivals.

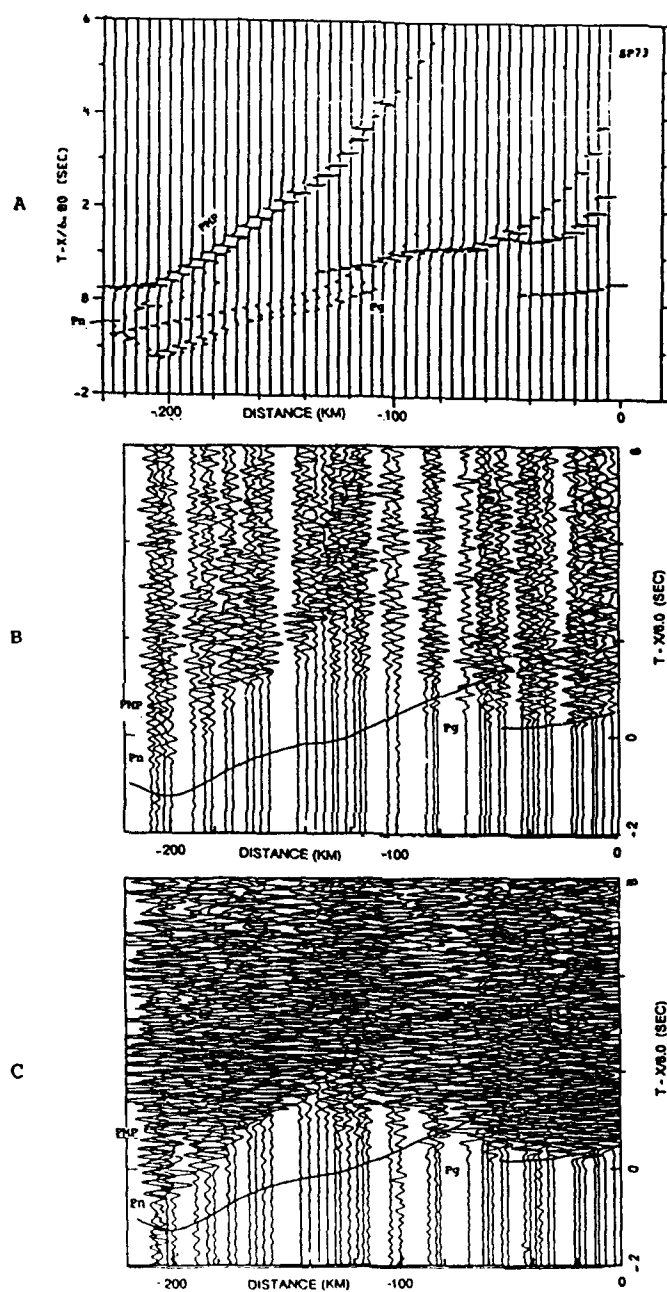


Figure 46: Same as Figure 45, but for SP73.

thetic sections. Information about the velocity structure of the lower crust can also be obtained from the analysis of later arrivals. The postcritical reflected wave from the Moho (PMP) is the strongest of the later arrivals of the synthetics, while waves reflected from the intermediate crustal boundaries are very weak.

At distances greater than 100-120 km, theoretical first arrival travel times are consistently 1-2 seconds faster than observed travel times (Figures 45 and 46). In this distance range of the observed data, the first arrivals attenuate and are offset to later times in the travel-time curves. Calculations do not predict this observed phenomenon. It is possible that our travel-time picks at distances greater than 100-120 km are secondary, high amplitude arrivals, and that the true first arrivals are very weak crustal refractions that are not observed. A thorough search was made for these arrivals, but none were detected for record sections constructed for different frequency ranges and amplifications (Figures 45 and 46).

Further careful analysis of all record section should probably more reliably determine if there are weak first arrivals that fit the predicted travel-times. It is worth noting that our synthetic analysis does not predict either attenuation or decreased amplitudes of the first arrivals at distances greater than 100-120 km (Figures 45 and 46). There are no large discrepancies between the theoretical and observed travel times for Pn waves. However, the Soviet model predicts a Pn wave cross-over point of 230-240 km and observations show that the cross-over occurs at distances of 150-160 km (Figures 45 and 46). There is one more important discrepancy between the synthetics and the observed data. According to calculations, reflected waves from the intermediate crustal boundaries recorded in the later arrivals should be very weak, but these waves are rather intensive on the observed record sections.

Conclusions

Preliminary analysis for three shot points (SP1, SP17, and SP73) of the Soviet crustal velocity model for the Norilsk DSS profile showed discrepancies between calculated and observed travel times and record sections. The major differences are:

For distances greater than 100-120 km, theoretical first arrival times were consistently faster than the observed travel times.

The Soviet model predicts a Pn cross-over point of 230-240 km, while the Pn wave was observed as a first arrival at distances of 150-160 km.

Predicted amplitudes of reflected waves from the intermediate crustal boundaries are very weak, but these waves are rather intensive on the observed record sections.

These discrepancies between the observed and theoretical data for prominent crustal and upper mantle P-waves will help us to construct an alternative two-dimensional crustal velocity model for the Norilsk profile that better fits the observed data. This model should contain lower crustal velocities and probably a thinner crust. At the neighboring Dikson-Khilok and Vorkuta-Tixie long-range profiles (Figure 40), high velocities of 6.8-7.0 km/s were observed at depths as shallow as 25-30 km (Egorkin et al., 1980, 1987). The results of this study indicate the importance of reinterpreting the Norilsk DSS profile.

References

- Egorkin, A.V., Chernyshev, N.M., Danilova, Ye. G., Kun, V.V., and Scheglova, L.B., "Regional section across the north of the Asiatic continent (Vorkuta-Tixie profile)," in *Seismic models of the lithosphere for the major geostructures on the territory of the USSR*, pp. 61-66, Nauka (Science) Publisher House (in Russian), Moscow, 1980.
- Egorkin, A.V., Zukanov, S.K., Pavlenkova, N.A., and Chernyshev, N.M., "Results of lithospheric studies from long-range profiles in Siberia," *Tectonophysics*, vol. 140, pp. 29-47, 1987.
- Egorkin, A.V., Zukanov, S.K., Mikhaltsev, A.V., and Chernyshev, N.M., "Integrated seismic investigations along geotraverses," in *Deep crustal studies of the USSR. Reports of Soviet Geologists*, pp. 226-237, Ministry of Geology of the USSR Publisher House (in Russian), Leningrad, 1989.
- Grichin, M.P., Zhero, O.A., Kramnik, V.N., Kuznetsov, V.L., Lotshev, V.I., Smirnov, L.V., and Surkov, V.S., "Deep structure of the Earth crust in platform regions of Siberia," in *Deep crustal studies of the USSR. Reports of Soviet Geologists*, pp. 152-162, Ministry of Geology of the USSR Publisher House (in Russian), Leningrad, 1989.
- Tuevov, I.K., "An application of mine explosions for crustal studies within transition zone between Siberian platform and Taimyr depression," *Geology and Geophysics (in Russian)*, no.2, pp. 123-127, 1965.

Simulations of Network Detection Capability Based on Noise Measurements from the GSETT-2 Experiment

Lori. T. Grant, Steve. R. Bratt and David. Corley

Introduction

The objective of this study is to simulate the global detection capability of the network used during the Group of Scientific Experts Second Technical Test (GSETT-2), between 22 April 1991 and 2 June 1991. The NETSIM computer program (Sereno *et al.*, 1990) is used to simulate network detection thresholds based on observational information from the GSETT-2 database including station coordinates, ambient noise conditions, instrument responses and usable data bandwidth after instrument corrections.

In addition to the GSETT-2 network simulations, the detection threshold for two sub-networks was also considered. The first was a subset of the GSETT-2 network, including 8 short-period arrays and the 4 high-frequency arrays. The second sub-network included only the 4 high-frequency arrays. The third network considered was a hypothetical "ideal" case consisting of the GSETT-2 network supplemented by 29 stations to enhance coverage in the Southern Hemisphere where GSETT-2 coverage is sparse. The additional stations in this hypothetical network are either existing, planned or proposed sites.

The simulations described in this report are theoretical estimates of our current capabilities for global detection. An empirical assessment of these capabilities can be made by comparing the GSETT-2 bulletin with local and regional bulletins. Such a study will be presented in a separate report.

This study differs from previous work in the following way. Sereno (1991) utilized the NETSIM program to assess the capabilities for monitoring the former Soviet Union with existing and proposed in-country networks. Signal and noise conditions in the former Soviet Union were not measured but were extrapolated from experience with arrays of the Intelligent Monitoring System (IMS, Bratt *et al.*, 1990) in Fennoscandia and from preliminary noise studies at the former-Soviet IRIS/IDA stations. The simulations in this study predict the capability of the GSETT-2 network and sub-networks, based on noise measured on waveforms archived during the 6-week GSETT-2 experiment. A major part of the work done by Sereno has been to normalize the source and path contributions to the NETSIM simulations. Much of Sereno's work is the starting point of this study which focuses on network coverage and site effects.

Description of the NETSIM Program

NETSIM is a computer program for simulating detection and location capability of seismic networks. Networks can consist of arrays and single stations with varying bandwidths. Signals from regional and/or teleseismic events are modeled by the program. The program simulates either detection threshold, detection probability, location uncertainty, or a combination of detection and location (e.g. minimum size of event that can be located with a given uncertainty).

The first step in NETSIM's detection module is to compute the probability of detection of each phase at each station for each epicenter in a geographic grid, using the signal, noise spectrum, station reliability and signal-to-noise ratio (*snr*) required for detection at each station. The signal spectrum is based on frequency-dependent source and attenuation estimates. The total noise spectrum is the sum of the station ambient noise and the noise due to the coda of previous phases. Thus, both signal and noise spectra are distance-dependent. NETSIM looks for the maximum *snr* over the entire spectral bandwidth for the specified interval and uses that *snr* to estimate the probability of detection for a phase at that station. The phase detection probabilities for all stations are then combined across the network to determine the probability of satisfying what can be complex detection criteria across the network. (e.g. detection criteria of "at least 3 P or Lg waves detected by the network" would mean 3 P's or 3 Lg's or 2 P's and 1 Lg or 1 P and 2 Lg's). The network magnitude detection threshold can be computed by iterating over magnitudes until a given network probability of detection is achieved (e.g. 90%).

NETSIM Input Parameters

NETSIM input parameters are organized into 5 categories shown schematically in Figure 47: Control, Source, Propagation, Noise and Site/Station. Each category can have several input files, represented by the small boxes in the figure. The following description of the input data is brief and more details about the NETSIM program can be found in Sereno *et.al.* (1990). For the simulations described in this report, the Source files and the Propagation files were held constant. The only changes were in the detection criteria and the Site/Station files that describe the network configuration and conditions at each station. Each NETSIM run has a unique control file which defines the simulation and points to the input files for the other 4 categories.

Control- The type of run (detection) is specified in the control file as well as the frequencies to include in the calculations (19 frequencies between 0.5 Hz and 19 Hz; 0.5 Hz increments below 5 Hz and 1 Hz increments above), the cross-over distance between regional and teleseismic phases (20 degrees), the representation of event size (M_{Lg}), and the range of event sizes to consider (0.5 to 6.0 M_{Lg}). Possible phases considered in each run are P

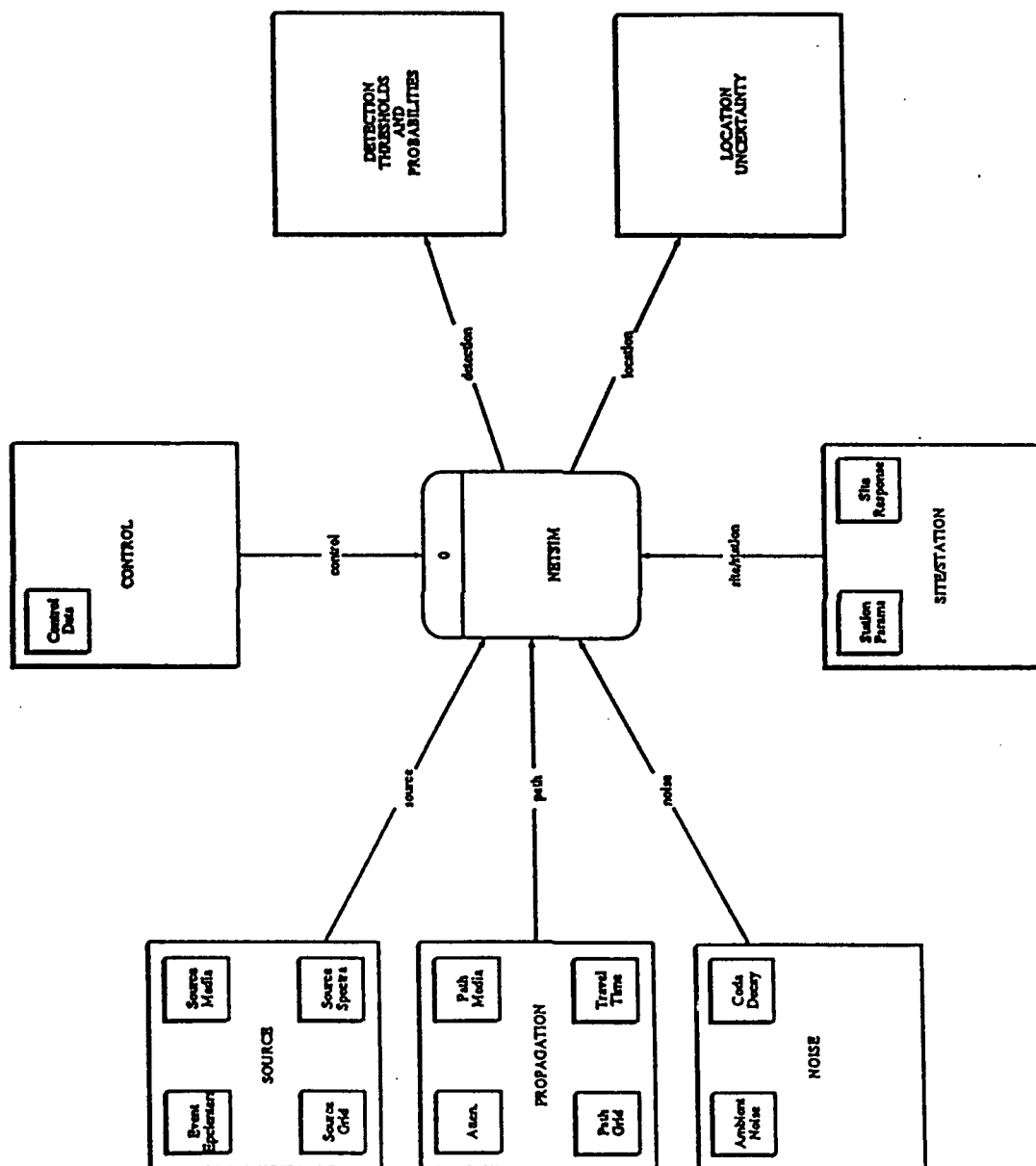


Figure 47: Schematic flow diagram for NetSim. Taken from Sereno *et.al.* 1990.

(or Pn), Pg, S (or Sn) and Lg.

Three different detection criteria are used in the runs: (1) Any P detected at any 2 stations; (2) Any P detected at any 3 stations; (3) Any P at any 2 stations *or* two local phases at one station. The first two criteria are used in the GSETT-2 runs while the third criterion is applied to simulate the sub-networks consisting of arrays.

Source- The source spectrum of each wave as a function of source medium and event size is estimated at each point in the epicenter grid. The epicenter grid is sampled at 10 degree increments in longitude (36 points) and in latitude between -80° and 80° (17 points), for a total of 612 points. A single source medium (granite) was specified for each grid point in the source grid file. Density, velocity and amplification factor are also specified for each wave. The explosion source file describes source spectra as a function of scalar seismic moment, M_0 , the corner frequency scaling inversely with the long-period level (Serenio *et al.*, 1990). Other data include the scaling relations for conversion between seismic moment and event size.

Propagation- The path medium file together with the path grid file describe areas of low attenuation (stable) and high attenuation (tectonic). Frequency-dependent attenuation, amplitude variance and travel-time tables for each wave over each path medium are also specified in the propagation files. The net attenuation is a summation of the attenuation across grid blocks along the entire path with the largest effect being at regional distances.

Noise- The power spectral density of the ambient noise (in nm^2/Hz) and its standard deviation (st. dev.) are specified for each station in the network. For these simulations, noise was measured using the GSETT-2 database for 39 out of 56 stations as described in the Noise Study section of this report. Coda decay rates are also specified for each phase.

Site/Station- Station coordinates, name of the file containing the ambient noise spectrum, st. dev. of the noise estimate, station reliability, and *snr* threshold for detecting each wave are listed for each station in a station file. The st. dev. of time residuals and st. dev. of azimuth residuals are given for use in the location module. This file also points to the local site response file containing a frequency-dependent array beam gain for each phase. The gain is specified as a function of frequency for each type of array: short-period array (spa) or high-frequency array (hfa). For arrays as well as single stations (ss), these site response files are used to define the bandwidth of usable data at each station.

Station reliability for the GSETT-2 time period is retrieved from the database as the percentage of time the station was operational. Station reliability ranges from 77% (at ARU) to 100% (for 8 stations). The default was 95%.

The default values for the frequency domain *snr* threshold are listed in Table 11 for each

phase type and each station type. The frequency-domain *snr* is estimated by Sereno (1991) to be 80% of the time-domain *snr*.

Table 11: SNR Thresholds by Phase and Station Type.

Type	P (or Pn)	Pg	S (or Sn)	Lg
ss	3.2	3.2	3.2	2.4
spa	3.2	3.2	2.0	1.5
hfa	3.2	3.2	2.0	1.5

Seismic Networks

All stations used in the simulations are shown in Figure 48. GSETT-2 stations are denoted with a cross inside a circle, GSETT-2 arrays are denoted with a cross inside a square. Additional stations, used in the hypothetical network, are denoted by an open circle. Table 12 lists the station code, coordinates, station type, and a description for each station. GSETT-2 stations are denoted by a "*" in the first column of the table. Stations denoted by a "+" in the first column are the additional stations in the hypothetical network. These include 5 IRIS stations (AAK, ASH, L01RPN, NOV, NRI); 3 CDSN stations (HIA, LZH, WMQ); 3 SRO stations (L04BOCO, L14BCAO, L19NWA0); and the WWSSN station, L08BDF. The remaining stations added to the hypothetical network are listed as either existing, planned or proposed station sites in a report of the International Seismological Observing Period, ISOP (Doornbos *et. al.*, 1991).

The GSETT-2 network includes 8 short-period arrays, 4 high-frequency arrays, and 46 single stations. Two of the GSETT-2 stations, SFP and PRF, were not used in the GSETT-2.

NETSIM Input Data from GSETT-2 Observations: Noise Study

This study differs from previous studies in that actual noise estimates were calculated using GSETT-2 waveforms. The program MASSPROC (Coyne, 1991) calculated average noise spectra directly from the database using up to 100 daytime and 100 nighttime noise windows for each station. The 5-second noise windows begin 15 seconds and end 10 seconds before reported first P-wave arrivals on the short-period vertical component when available, and broad-band vertical otherwise. Windows including or within 30 seconds after a reported phase detection were excluded. Noise spectra were corrected for the instrument response received from each station during GSETT-2.

The noise study was performed for 39 stations out of the 58 stations participating in

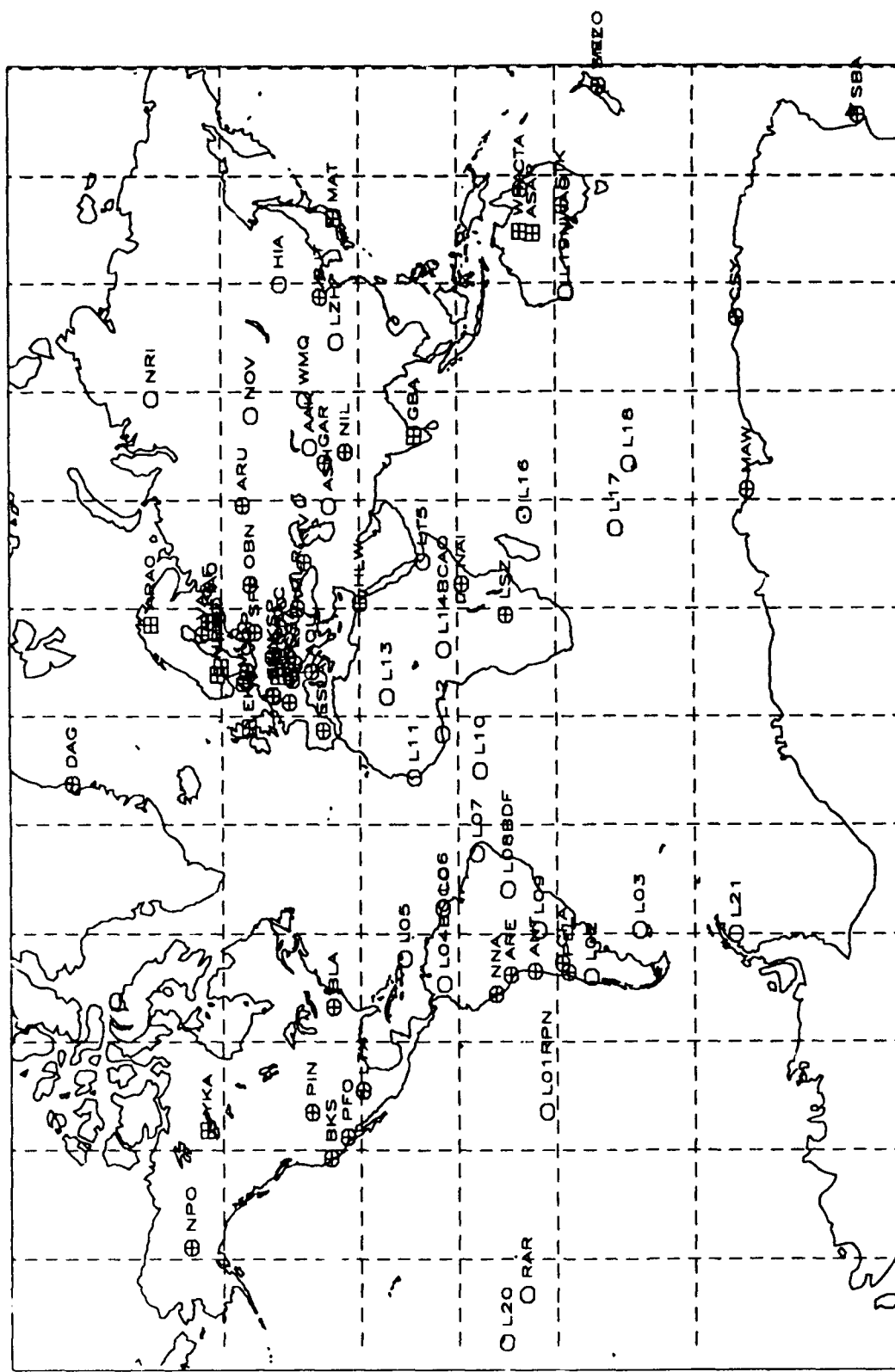


Figure 48: Stations used in simulations. GSEI T-2 stations are denoted by a cross inside a circle; GSEI T-2 arrays by a cross inside a square; and open circles represent additional stations in the hypothetical network.

Table 12: Stations Used in the Simulations

*	STA	LAT	LON	TYPE	DESCRIPTION
*	ANT	-23.705	-70.415	ss	ANTOFAGASTA,CHILE
*	AQU	42.354	12.403	ss	L'AQUILA,ITALY
*	ARA0	69.535	25.506	hfa	ARCESS ARRAY,NORWAY
*	ARE	-16.462	-71.491	ss	AREQUIPA,PERU
*	ARU	56.400	58.600	ss	ARTI,OBLAST,USSR(IRIS)
*	AS12	-23.704	133.962	spa	ALICE SPRINGS ARRAY,AUSTRALIA
*	BJT	40.040	116.175	ss	BAIJATUAN,CHINA
*	BKS	37.877	-122.235	ss	BYERLY,CALIFORNIA
*	BLA	37.211	-80.420	ss	BLACKSBURG,VIRGINIA
*	CFA	-31.607	-68.239	ss	CORONEL_FONTANA,ARGENTINA
*	COP	55.685	12.432	ss-	COPENHAGEN,DENMARK
*	CSY	-66.289	110.529	ss-	CASEY-ANTARCTIC_TERR.,AUS.
*	CTA	-20.088	146.254	ss	CHARTERS_TOWERS,AUS.
*	DAG	76.771	-18.655	ss	DANMARKSHAVN,GREENLAND
*	EKA	55.333	-3.159	spa	ESKDALEMUIR_ARRAY,UK
*	ENN	50.767	5.923	ss	EPEN,NETHERLANDS
*	ESLA	39.670	-3.960	ss	SONSECA_ARRAY_STATION,SPAIN
*	FIA0	61.444	26.079	hfa	FINESA_ARRAY,FINLAND
*	GAR	39.000	70.300	ss	GARM,USSR
*	GBA	13.615	77.590	spa	GAURIBIDANUR_ARRAY,INDIA
*	GEO0	48.836	13.704	hfa	GERESS_ARRAY,GERMANY
*	GRA1	49.692	11.222	spa	GRAFENBERG_ARRAY,GERMANY
*	HFS	60.133	13.684	spa	HAGFORS_ARRAY,SWEDEN
*	HLW	29.858	31.342	ss	HELWAN,UNITED_ARAB_REPUBLIC
*	KAF	62.113	26.306	ss	KANGASNIEMI,FINLAND

Table 12: Stations Used in the Simulations

*	STA	LAT	LON	TYPE	DESCRIPTION
*	KIV	43.950	42.683	ss	KISLOVODSK,USSR
*	KSP	50.843	16.293	ss	KSIAZ,POLAND
*	LJU	46.043	14.533	ss	LJUBLJANA,YUGOSLAVIA
*	LOR	47.267	3.851	ss	LORMES,FRANCE
*	LSZ	-15.277	28.188	ss	LUSAKA,ZAMBIA
*	LTX	29.334	-103.667	ss	LAJITAS,TEXAS
*	MAT	36.543	138.207	spa	MATSUSHIRO,JAPAN
*	MAW	-67.604	62.871	ss	MAWSON,ANTARCTICA
*	MLR	45.489	29.944	ss	MUNTELE_ROSU,ROMANIA
*	MUD	56.460	9.170	ss	DENMARK,DENMARK
*	NAI	-1.274	36.804	ss	NAIROBI,KENYA
*	NIL	33.650	73.252	ss	NILORE,PAKISTAN
*	NNA	-11.988	-76.842	ss	NANA,PERU
*	NPO	64.771	-146.887	ss	NORTH_POLE,ALASKA
*	NRA0	60.735	11.541	hfa	NORESS_ARRAY,NORWAY
*	OBN	55.117	36.567	ss	OBNINSK,USSR
*	OSS	46.690	10.133	ss	OVA_SPIN,SWITZERLAND
*	PEL	-33.144	-70.685	ss	PELDEHUE,CHILE
*	PFO	33.610	-116.460	ss	PINON_FLAT,CALIFORNIA
*	PIN	42.583	-109.717	ss	PINEDALE,WYOMING
*	PRF#	60.386	25.681	ss	PORVOO,FINLAND
*	RAR#	-21.212	-159.773	ss	RAROTONGA,COOK_ISLANDS
*	SBA	-77.850	166.756	ss	SCOTT_BASE,ANTARCTICA
*	SFP	54.280	23.300	ss	POLAND
*	SNZO	-41.310	174.705	ss	SOUTH_KARORI,NEW_ZEALAND

Table 12: Stations Used in the Simulations

*	STA	LAT	LON	TYPE	DESCRIPTION
*	SQTA	47.221	11.209	ss	SAINT_QUIRIN,AUSTRIA
*	STI	50.585	5.564	ss	SART-TILMAN,BELGIUM
*	STK	-31.882	141.592	ss	STEPHENS_CREEK,AUSTRALIA
*	VAF	63.042	22.671	ss	VAASA,FINLAND
*	VRAC	49.309	16.595	ss	VRANOV,CZECHOSLOVAKIA
*	WEL	-41.286	174.768	ss	WELLINGTON,NEW_ZEALAND
*	WRA	-19.766	134.389	spa	WARRAMUNGA_ARRAY,AUSTRALIA
*	YKA	62.493	-114.605	spa	YELLOWKNIFE_ARRAY,CANADA
+	AAK	42.600	74.500	---	ALA-ARCHA,KIRGIZ_SSR(IRIS)
+	ASH	38.000	58.400	---	ASHKHABAD,USSR(IRIS)
+	HIA	49.267	119.742	---	NEIMENGGU_PROV,CHINA(CDSN)
+	L01RPN	-27.158	-109.434	---	RAPA_NUI,EASTER_ISLAND(IRIS)
+	L02	-39.000	-72.000	---	ISOP-planned
+	L03	-50.000	-59.000	---	ISOP-planned
+	L04BOCO	4.585	-74.039	---	BOGOTA,COLOMBIA(SRO)
+	L05	17.000	-67.000	---	ISOP-proposed
+	L06	5.000	-53.000	---	ISOP-existing
+	L07	-6.000	-38.000	---	ISOP-proposed
+	L08BDF	-15.658	-47.902	---	BRASILIA_ARRAY,BRAZIL(WWNSS)
+	L09	-25.000	-59.000	---	ISOP-planned
+	L10	-7.000	-15.000	---	ISOP-planned
+	L11	14.000	-17.000	---	ISOP-existing(DAK,SENEGAL)
+	L12	5.000	-5.000	---	ISOP-planned
+	L13	22.000	5.400	---	ISOP-planned
+	L14BCAO	4.367	18.567	---	BANGUI,CENT_AFRICAN_REP.(SRO)

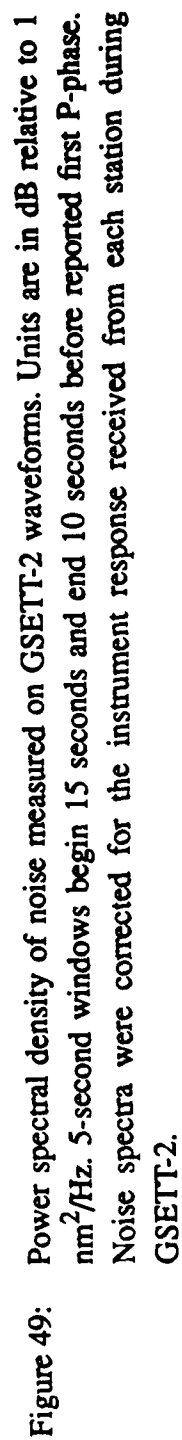
Table 12: Stations Used in the Simulations

*	STA	LAT	LON	TYPE	DESCRIPTION
+	L15	11.000	43.000	---	ISOP-existing
+	L16	-21.000	56.000	---	ISOP-planned
+	L17	-45.000	52.000	---	ISOP-existing
+	L18	-48.000	70.000	---	ISOP-existing
+	L19NWA O	-32.923	117.236	---	NARROGIN,AUSTRALIA(SRO)
+	L20	-15.000	-173.000	---	ISOP-existing
+	L21	-66.000	-60.000	---	ISOP-proposed....
+	LZH	36.087	103.844	---	LANCHOW,CHINA(CDSN)
+	NOV	54.900	83.300	---	NOVOSIBIRSK(NVS),USSR(IRIS)
+	NRI	69.400	88.000	---	NORIL'SK,CENTRAL_SIBERIA(IRIS)
+	WMQ	43.821	87.695	---	WULUMUCHE,CHINA(CDSN)

GSETT-2. It was not possible to get noise estimates for the other stations for various reasons. Some stations did not submit waveform data, some did not provide instrument responses, and for some, the waveform data and/or responses were deemed unreliable. Although we do not anticipate any major changes, all noise spectra presented in this report are preliminary. Current work is underway to verify each instrument-corrected spectrum.

The noise spectra were grouped into 8 categories, based on amplitude and shape, and numbered by increasing noise levels. All noise estimates are plotted by groups in Figure 49. The maximum usable frequency is shown to the right of the station name in the legend of each plot. This cut-off frequency is, in general, 80% of the Nyquist frequency. These frequencies were determined by visual inspection of the noise spectra and input to NETSIM through the site response files. In some cases, the cut-off frequency severely limits the bandwidth of the station. For example, AS12 should have a maximum frequency of 8 Hz, but only frequencies less than 3.5 Hz can be used, because of the shape of the provided instrument response beyond 3.5 Hz. Figure 50 shows the Nyquist and high-frequency cut-off for the 39 stations with noise estimates. The minimum frequency considered in the simulations is 0.5 Hz.

Group 1 had the lowest noise level. Noise spectra for stations LTX, PIN, YKA and WRA



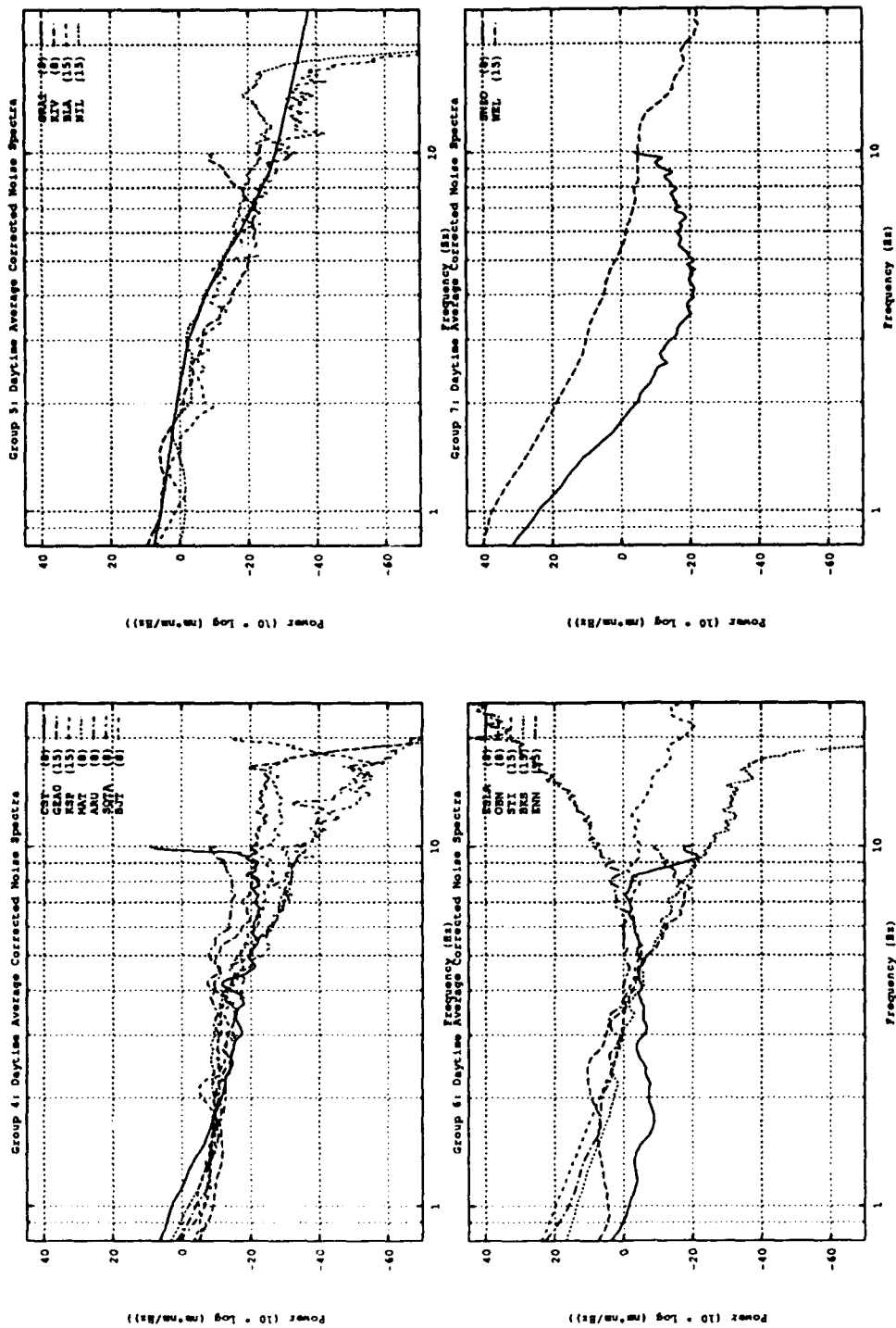


Figure 49: Continued.

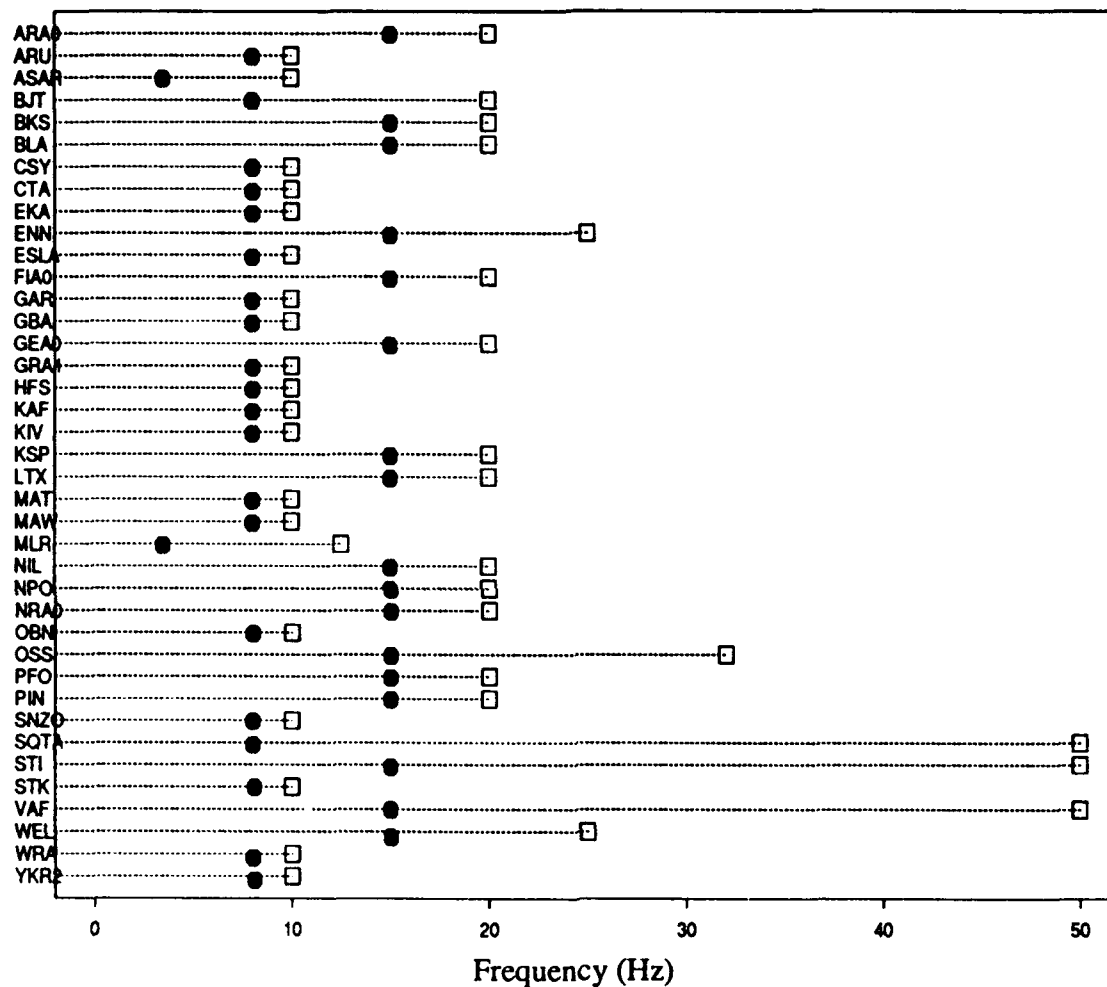


Figure 50: Nyquist frequency (open square) and cut-off frequency (solid dot) for each GSETT-2 station with noise measurements

have very similar shapes over the band 2 to 10 Hz, ranging from -20 dB at 2 Hz to -50 dB at 10 Hz. The spectrum of station STK has an anomalous shape and a lower cut-off frequency (8 Hz). Groups 2 and 2a have similar levels, ranging from -10 dB at 2 Hz to -40 dB at 10 Hz. Stations KAF, CTA, and MLR in groups 2 and 2a have lower cut-off frequencies. Group 3 includes GBA, OSS and PFO, with noise levels higher between 2 and 5 Hz than group 2a. AS12 is very limited in frequency (0 - 3.5 Hz), and GAR has a cut-off of 8 Hz. Group 4 ranges between -10 dB at 2 Hz and -30 dB at 10 Hz, and has a large variability in shape. Group 5 has the highest noise level with consistent shapes (0 dB at 2 Hz and -20 to -25 dB at 10 Hz). Groups 6 and 7 are characterized by high noise levels, different shapes and limited bandwidth. Figure 51 displays one spectrum from each of groups 1 -5. They show a consistent difference of 30 dB between 2 and 10 Hz.

For the 17 GSETT-2 stations without noise estimates, we substituted those obtained for MAT (for: ANT, AQU, ARE, CFA, HLW, NAI, NNA, PEL), CSY (for: DAG, SBA), KSP (for: LOR, LJU, LSZ, VRAC), STI (for: COP, MUD), and SNZO (for: RAR). All these substitutions correspond to noise-level group 4 or above and are based on expected noise conditions including proximity to ocean and station type. For example, SNZO noise from group 7 was used at RAR because we assumed high-noise conditions at this island station. Table 13 lists the stations, station type, sample rate (SR, in samples/sec.), component for noise measurement, noise group level, standard deviation of noise estimate (SD), cut-off frequency (f_{max} , in Hz), and, when a substitution was made, the substituting station is listed. The last column is the station reliability. Noise data used for the 29 additional stations are also listed.

Network Simulations of Detection Threshold

Simulations of detection thresholds for 4 different networks including GSETT-2, two sub-networks and a theoretical network, are discussed in this section.

To compare the simulations quantitatively, the world was divided into 6 general areas outlined in Figure 52. The number of epicenters in the geographic grid, number of GSETT-2 stations in the area, and latitude and longitude bounds are listed below for each area.

Eurasia;

152 epicenters; latitude 0° to 75° and longitude 0° to 180° ; 29 stations

Australia and Southeast Pacific;

56 epicenters; latitude 0° to -75° and longitude 120° to 180° ; 6 stations

Indian Ocean and South Atlantic;

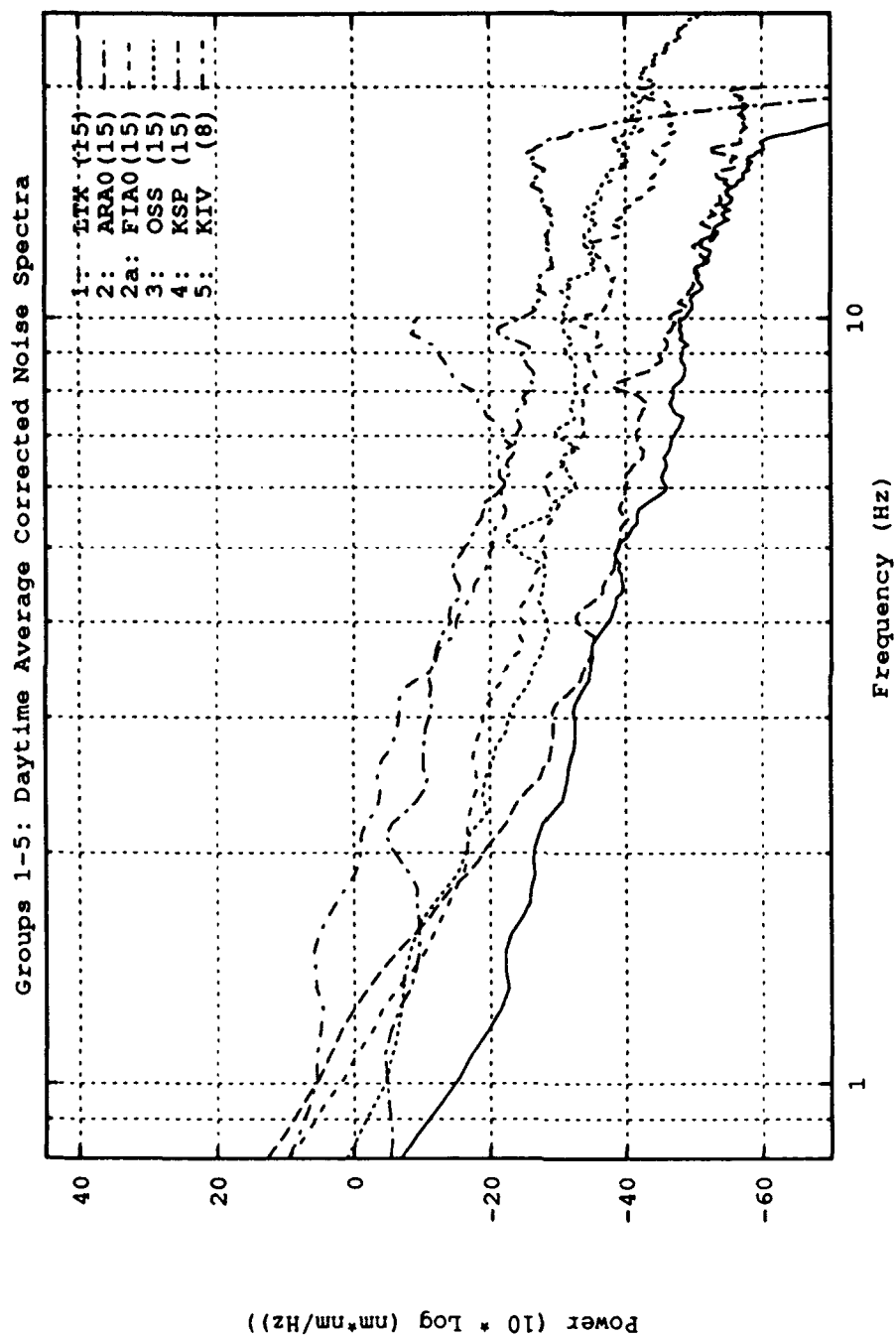


Figure 51: One noise spectrum from each of groups 1-5. Station LTX is in the lowest noise-level group, 1. Station KIV is in the highest noise-level group, 5. A 30 dB difference in noise levels between groups 1 and 5 is observed through the 2 to 10 Hz band. Cut-off frequencies are shown in parenthesis to the right of the station name.

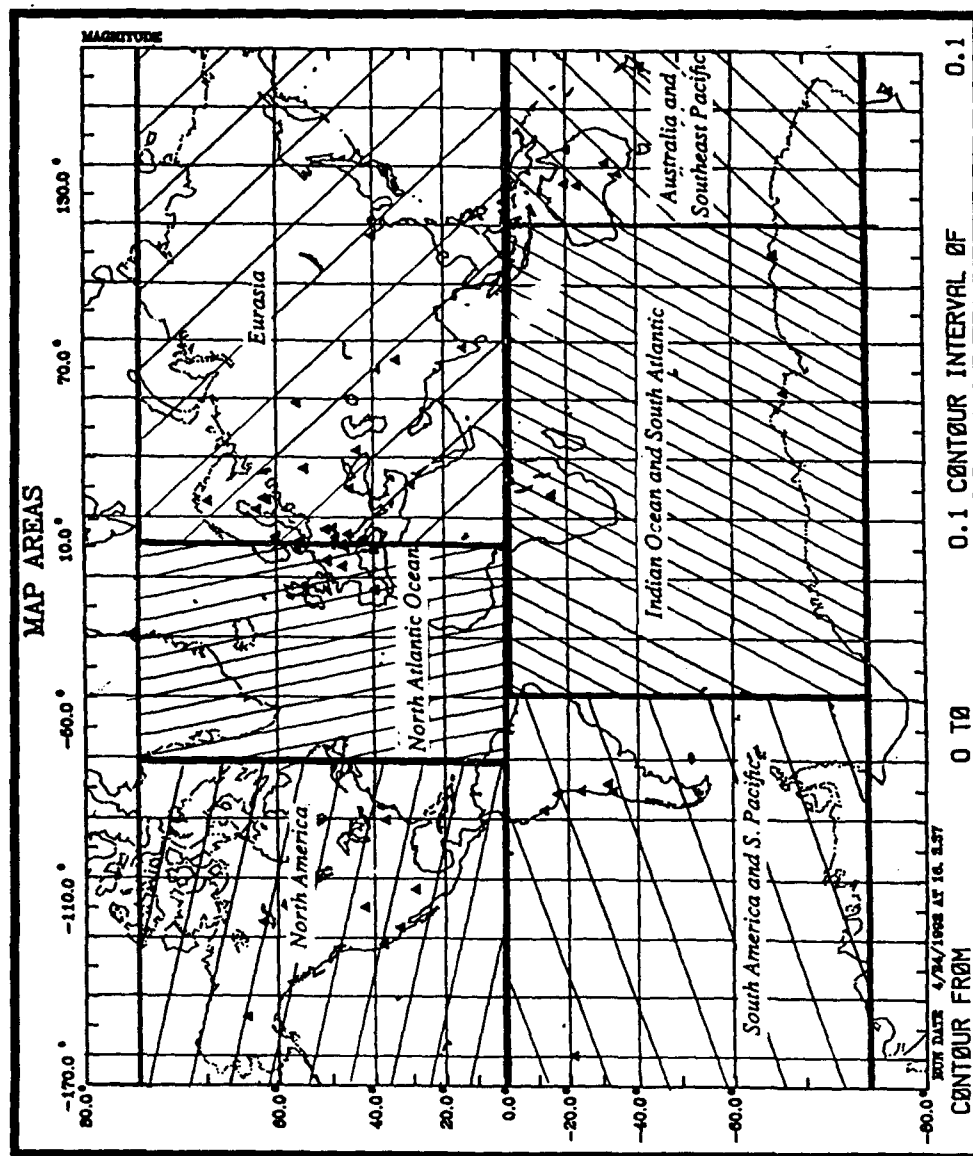


Figure 52: World map showing 6 areas for quantitative comparison of simulation results. (1) Eurasia, (2) Australia and Southeast Pacific Ocean, (3) Indian Ocean and South Atlantic Ocean, (4) South America and Southwest Pacific Ocean, (5) North America and North Atlantic Ocean.

Table 13: Noise Data for Each Station

*	STA	TYPE	SR	Comp	Noise	SD	f _{max}	SUB	REL
*	ANT	ss	--	--	-----	-----	3.5	MAT	0.950
*	AQU	ss	50	sz	-----	-----	8.0	MAT	0.990
*	ARA0	hfa	40	sz	group2	0.330	15.0	--	0.990
*	ARE	ss	--	--	-----	-----	3.5	MAT	0.950
*	ARU	ss	20	bz	group4	0.380	8.0	--	0.770
*	ASAR	spa	20	sz	group3	0.340	3.5	--	0.990
*	BJT	ss	40	sz	group4	0.300	8.0	--	0.990
*	BKS	ss	40	sz	group6	0.470	15.0	--	0.970
*	BLA	ss	40	sz	group5	0.350	15.0	--	0.990
*	CFA	ss	--	--	-----	-----	3.5	MAT	0.950
*	COP	ss	10	sz	-----	-----	3.5	STI	0.990
*	CSY	ss	20	sz	group4	0.400	8.0	--	0.980
*	CTA	ss	20	bz	group2a	0.370	8.0	--	0.990
*	DAG	ss	--	--	-----	-----	3.5	CSY	0.950
*	EKA	spa	20	sz	group2	0.310	8.0	--	0.990
*	ENN	ss	50	sz	group6	0.390	15.0	--	0.950
*	ESLA	ss	20	sz	group6	0.290	8.0	--	0.860
*	FIA0	hfa	40	sz	group2a	0.340	15.0	--	0.950
*	GAR	ss	20	bz	group3	0.350	8.0	--	0.900
*	GBA	spa	20	sz	group3	0.430	8.0	--	0.950
*	GEA0	hfa	40	sz	group4	0.320	15.0	--	0.910
*	GRA1	spa	20	bz	group5	0.350	8.0	--	0.950
*	HFS	spa	20	sz	group2a	0.310	8.0	--	0.950
*	HLW	ss	--	--	-----	-----	3.5	MAT	0.950
*	KAF	ss	20	sz	group2a	0.310	8.0	--	0.950

Table 13: Noise Data for Each Station

*	STA	TYPE	SR	Comp	Noise	SD	f _{max}	SUB	REL
*	KIV	ss	20	bz	group5	0.360	8.0	--	0.940
*	KSP	ss	40	sz	group4	0.380	15.0	--	0.960
*	LJU	ss	--	--	-----	-----	3.5	KSP	0.950
*	LOR	ss	50	sz	-----	-----	15.0	KSP	1.000
*	LSZ	ss	50	sz	-----	-----	15.0	KSP	1.000
*	LTX	ss	40	sz	group1	0.470	15.0	--	0.900
*	MAT	spa	20	sz	group4	0.470	8.0	--	1.000
*	MAW	ss	20	bz	group2	0.350	8.0	--	1.000
*	MLR	ss	25	sz	group2	0.370	3.5	--	0.940
*	MUD	ss	--	--	-----	-----	3.5	STI	0.950
*	NAI	ss	--	--	-----	-----	3.5	MAT	0.990
*	NIL	ss	40	sz	group5	0.420	15.0	--	0.990
*	NNA	ss	--	--	-----	-----	3.5	MAT	0.950
*	NPO	ss	40	sz	group2a	0.500	15.0	--	0.940
*	NRA0	hfa	40	sz	group2	0.340	15.0	--	1.000
*	OBN	ss	20	bz	group6	0.350	8.0	--	0.970
*	OSS	ss	64	sz	group3	0.330	15.0	--	1.000
*	PEL	ss	--	--	-----	-----	3.5	MAT	0.950
*	PFO	ss	40	sz	group3	0.500	15.0	--	1.000
*	PIN	ss	40	sz	group1	0.500	15.0	--	0.980
*	PRF	ss	20	sz	-----	-----	xxxxxx	XXXX	XXXX
*	RAR	ss	--	--	-----	-----	3.5	SNZO	0.950
*	SBA	ss	--	--	-----	-----	3.5	CSY	0.950
*	SFP	ss	40	sz	-----	-----	xxxxxx	XXXX	XXXX
*	SNZO	ss	20	sz	group7	0.300	8.0	--	0.950

Table 13: Noise Data for Each Station

*	STA	TYPE	SR	Comp	Noise	SD	f _{max}	SUB	REL
*	SQTA	ss	100	sz	group4	0.320	8.0	--	0.790
*	STI	ss	100	sz	group6	0.320	15.0	--	0.950
*	STK	ss	20	bz	group1	0.320	8.0	--	0.970
*	VAF	ss	100	sz	group2a	0.420	15.0	--	0.950
*	VRAC	ss	25	sz	-----	-----	8.0	KSP	0.950
*	WEL	ss	50	sz	group7	0.500	15.0	--	0.950
*	WRA	spa	20	sz	group1	0.380	8.0	--	0.830
*	YKR2	spa	20	sz	group1	0.340	8.0	--	1.000
+	AAK	ss	20	--	group3	0.350	8.0	GAR	1.000
+	ASH	ss	20	--	group3	0.350	8.0	GAR	1.000
+	HIA	ss	20	--	group3	0.350	8.0	GAR	1.000
+	L01RPN	ss	20	--	group7	0.300	8.0	SNZO	0.950
+	L02	ss	20	--	group4	0.470	8.0	MAT	0.950
+	L03	ss	20	--	group7	0.300	8.0	SNZO	0.950
+	L04BOCO	ss	20	--	group4	0.470	8.0	MAT	0.950
+	L05	ss	20	--	group7	0.300	8.0	SNZO	0.950
+	L06	ss	20	--	group4	0.470	8.0	MAT	0.950
+	L07	ss	20	--	group4	0.470	8.0	MAT	0.950
+	L08BDF	ss	20	--	group4	0.380	8.0	KSP	0.950
+	L09	ss	20	--	group4	0.380	8.0	KSP	0.950
+	L10	ss	20	--	group7	0.300	8.0	SNZO	0.950
+	L11	ss	20	--	group4	0.470	8.0	MAT	0.950
+	L12	ss	20	--	group4	0.470	8.0	MAT	0.950
+	L13	ss	20	--	group4	0.380	8.0	KSP	0.950
+	L14BCAO	ss	20	--	group4	0.380	8.0	KSP	0.950

Table 13: Noise Data for Each Station

*	STA	TYPE	SR	Comp	Noise	SD	f_{\max}	SUB	RFL
+	L15	ss	20	--	group4	0.470	8.0	MAT	0.950
+	L16	ss	20	--	group7	0.300	8.0	SNZO	0.950
+	L17	ss	20	--	group7	0.300	8.0	SNZO	0.950
+	L18	ss	20	--	group7	0.300	8.0	SNZO	0.950
+	L19NWA0	ss	20	--	group4	0.470	8.0	MAT	0.950
+	L20	ss	20	--	group7	0.300	8.0	SNZO	0.950
+	L21	ss	20	--	group4	0.470	8.0	MAT	0.950
+	LZH	ss	20	--	group3	0.350	8.0	GAR	1.000
+	NOV	ss	20	--	group3	0.350	8.0	GAR	1.000
+	NRI	ss	20	--	group3	0.350	8.0	GAR	1.000
+	WMQ	ss	20	--	group3	0.350	8.0	GAR	1.000
+	SFP	ss	20	--	group3	0.350	8.0	GAR	1.000

136 epicenters; latitude -75° to 0° and longitude -40° to 110° ; 3 stations

South America and S. Pacific;

112 epicenters; latitude -75° to 0° and longitude -170° to -40° ; 6 stations

North America;

96 epicenters; latitude 0° to 75° and longitude -170° to -60° ; 7 stations

North Atlantic Ocean;

56 epicenters; latitude 0° to 75° and longitude 0° to -60° ; 2 stations

GSETT-2 Network

Figure 53 shows the 90% M_{Lg} detection threshold for the GSETT-2 network with detection criteria requiring a P-type phase at any 2 stations. Minima occur where there is a cluster of stations allowing the detection criteria to be easily met in Fennoscandia, Australia, Western South America, and Western United States. Away from these minima, the detection threshold is between M_L 3.5 and 4.2. The most notable feature of detection threshold contours is that all of Fennoscandia, Europe, Western Eurasia, and the Northern part of the

African continent is enclosed by the 3.6 contour. Almost 50%, or 26 of the 56 GSETT-2 stations are inside this area. A smaller area including most of the North American continent is also enclosed by the 3.6 contour. Most of the world's oceans are covered by the 3.8 contour with the exception of the South Atlantic Ocean where the threshold reaches 4.2.

Figure 53(b) shows the GSETT-2 simulation with the detection criteria requiring a P-type phase at 3 stations. Here the areas enclosed by the 3.6 contour are smaller and the 4.2 contour covers a larger part of the South Atlantic. A difference plot of the two simulations is shown in Figure 53(c). The values of the detection threshold for each area are summarized in Table 14. The median threshold for the world increases by 0.2 when 3 P's are required for a valid event. The largest changes are in North America, South America, and Australia. In these areas, there are several stations close together but the surrounding areas do not have many stations.

GSETT-2 Arrays: 12-Array Network

The next network considered is a subset of the GSETT-2 network including only the 8 short-period arrays and the 4 high-frequency arrays. Figure 54a shows the 90% M_{Lg} detection thresholds. Seven out of the twelve arrays are in Eurasia, so the median threshold does not increase in that area with respect to the GSETT-2 network. In South America, where there are no arrays, the increase is 0.3 with respect to GSETT-2 network. The detection criteria were changed slightly for the next simulation, shown in Figure 54b, to allow any two P-type phases at any 2 stations or two local phases (P_g and L_g). These criteria are used in routine analysis of array data.

GSETT-2 High-Frequency Arrays: 4-Array Network

Another subset of the GSETT-2 network is modeled using only the four high-frequency arrays which comprise the IMS-2 network: ARCESS, NORESS, FINESSA and GERESS. The 90% M_{Lg} detection threshold contours are shown in Figure 55(a) for 3 P phases and (b) for 2 P phases or 2 local phases. Table 15 summarizes the thresholds for the 12-array and 4-array networks for the 3-P criterion. Table 16 summarizes the results for the 2-phase criteria. The main difference between the 12-array and the 4-array networks is in the southern Hemisphere. Without the additional arrays (GBA, MAT, YKA, WRA and ARAR) outside of Eurasia, the threshold quickly reaches 4.8 and stays above 4.8 throughout the Southern hemisphere.

Hypothetical 85-Station Network

The hypothetical 85-Station Network includes the 58 GSETT-2 stations and 27 additional stations chosen from existing or proposed seismic sites. Observed noise estimates are used

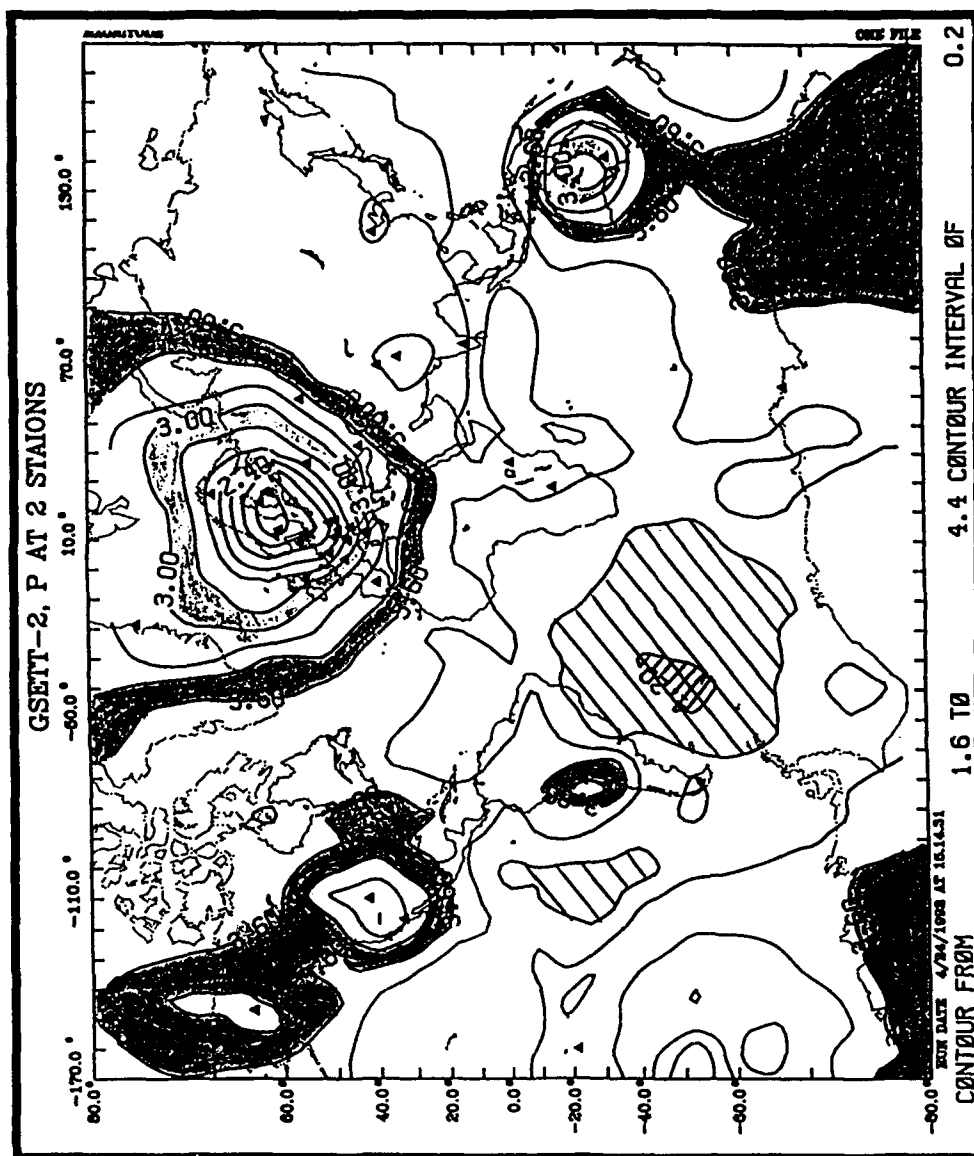


Figure 53: 90% M_{LG} Detection Threshold for GSETT-2 Network. (a) Detection criteria of 2 P phases at any 2 stations. (b) Detection criteria of 3 P phases at any 3 stations. (c) Difference between (b) and (a) showing increase in detection threshold when 3 P's are required versus 2 P's for a valid event.

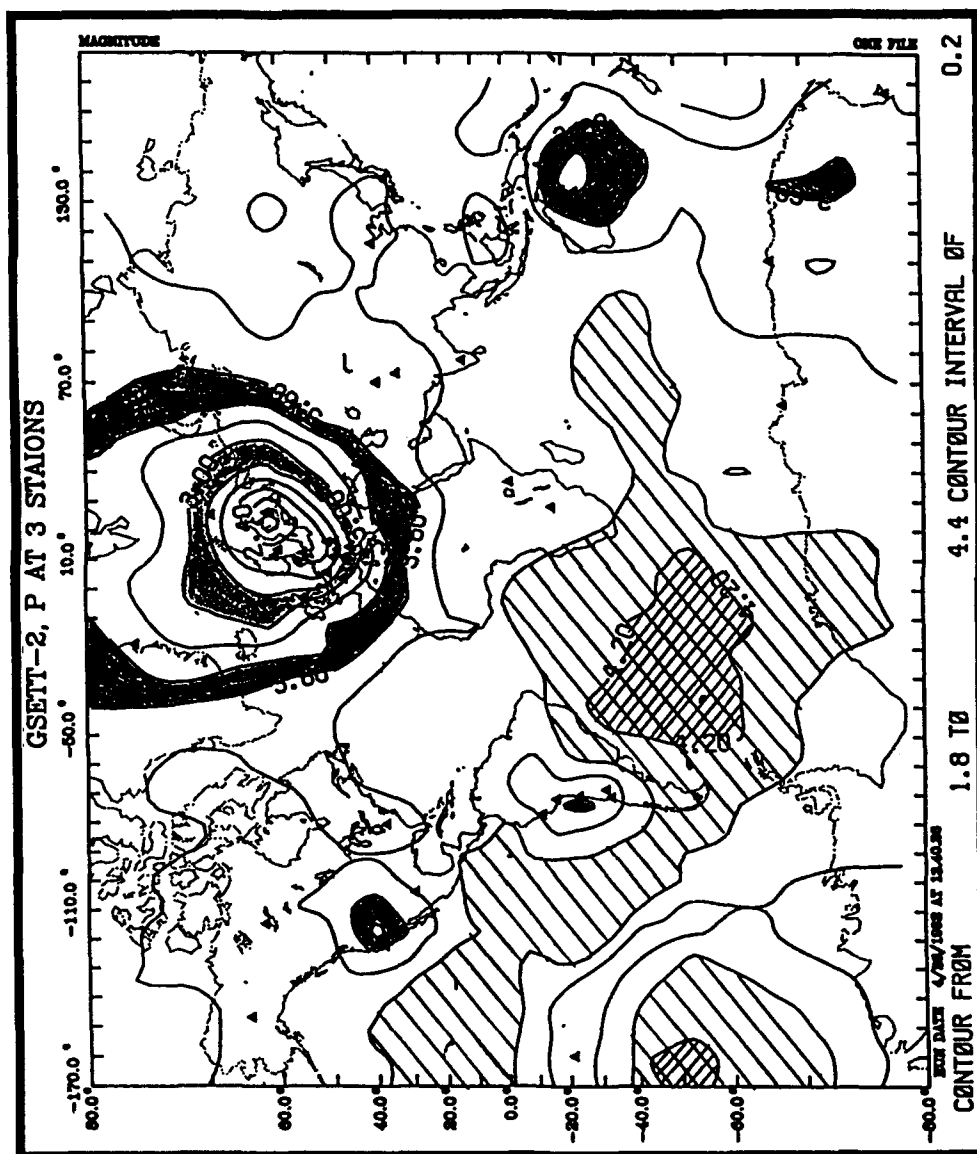
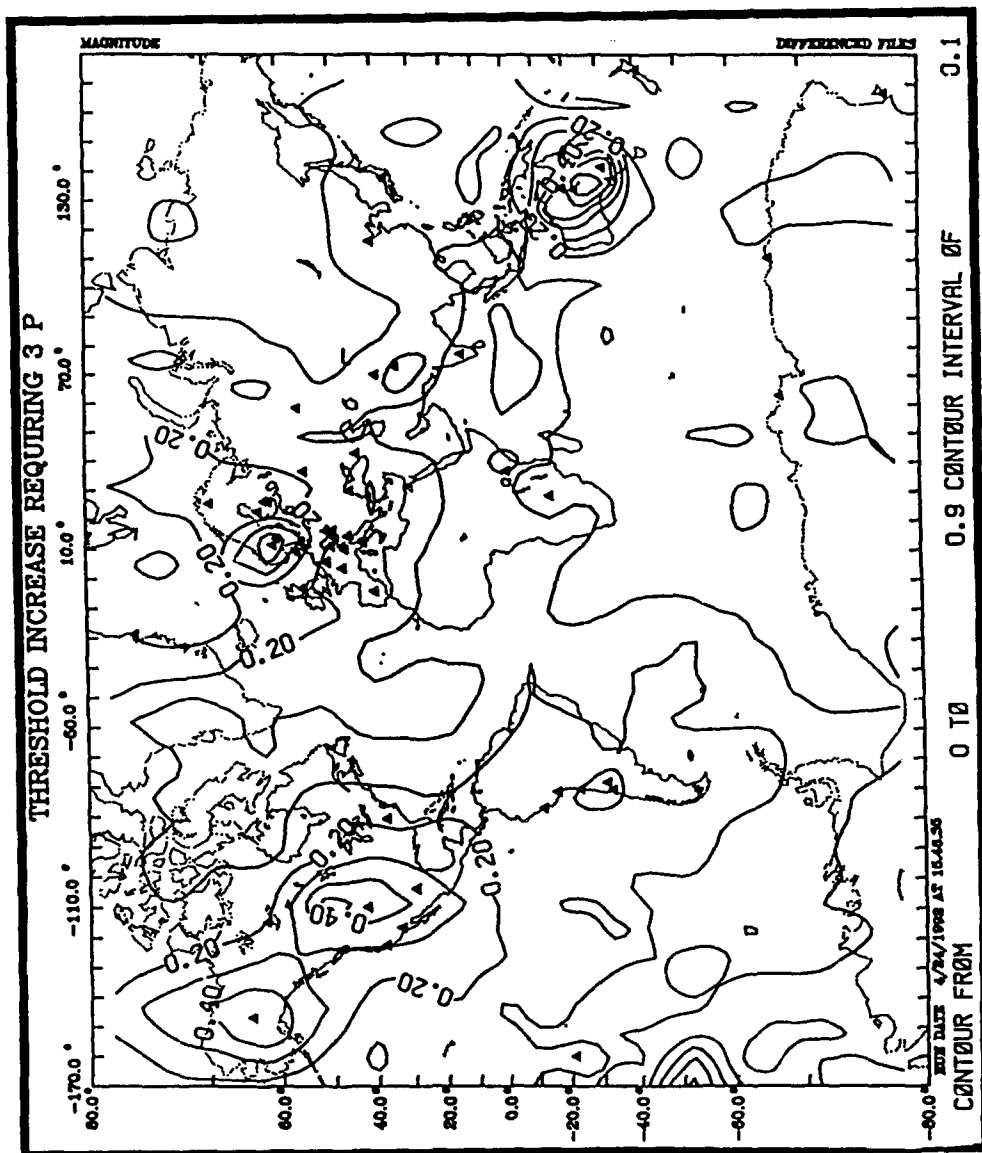


Figure 53(b):



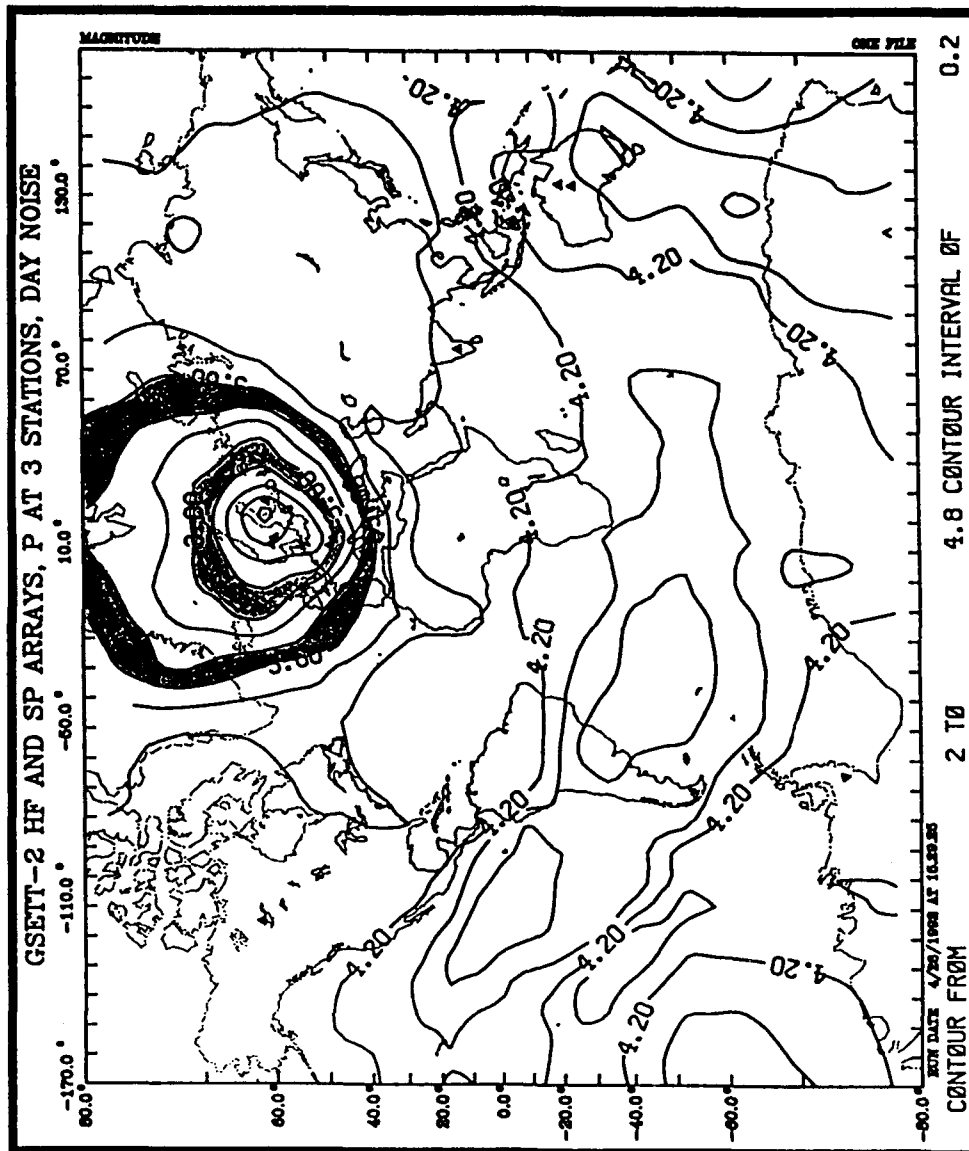
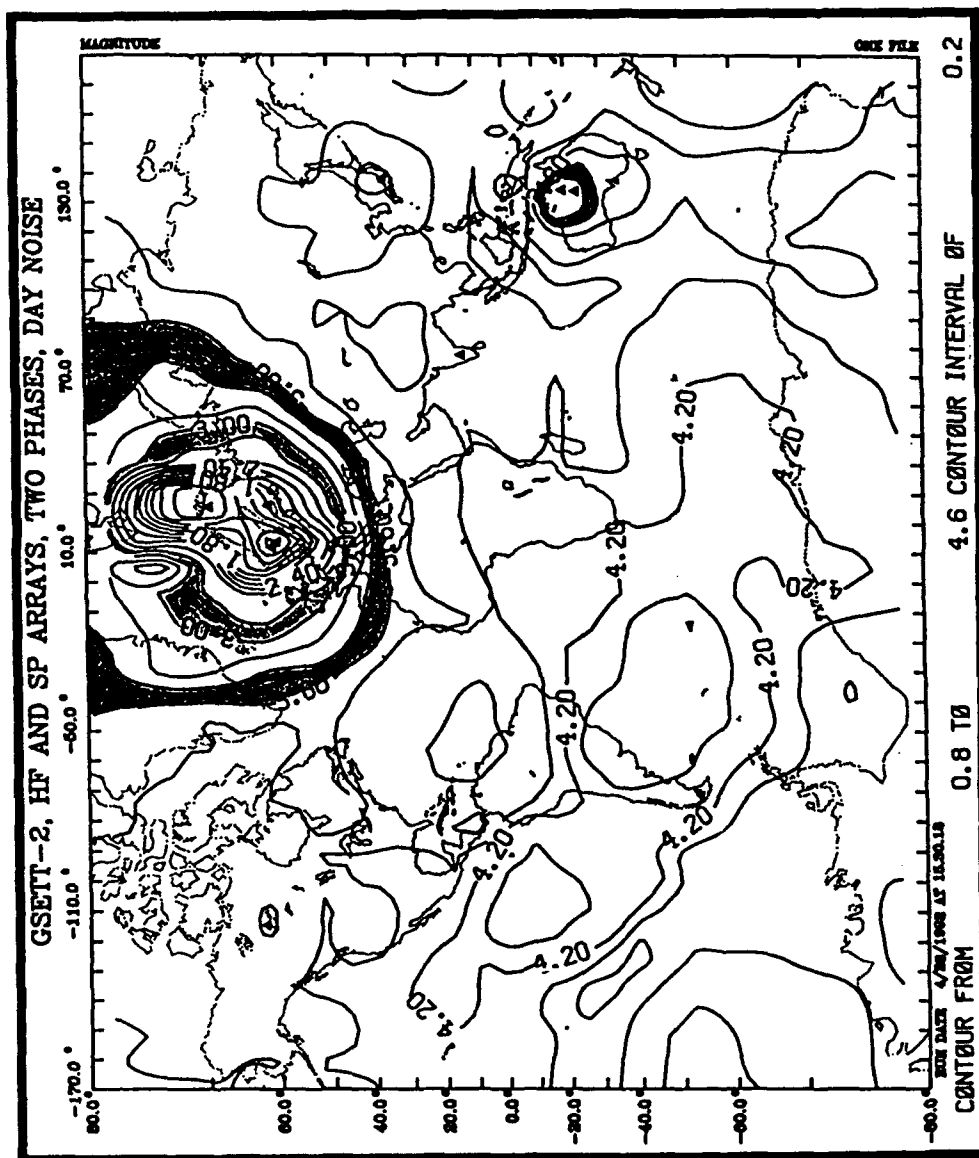


Figure 54: 90% M_{Lg} Detection Threshold for 12-Array Network. (a) Detection criteria requiring 3 P phases at any three stations. (b) Detection criteria requiring 2 P phases at any two stations or one Pg and one Lg at any station.



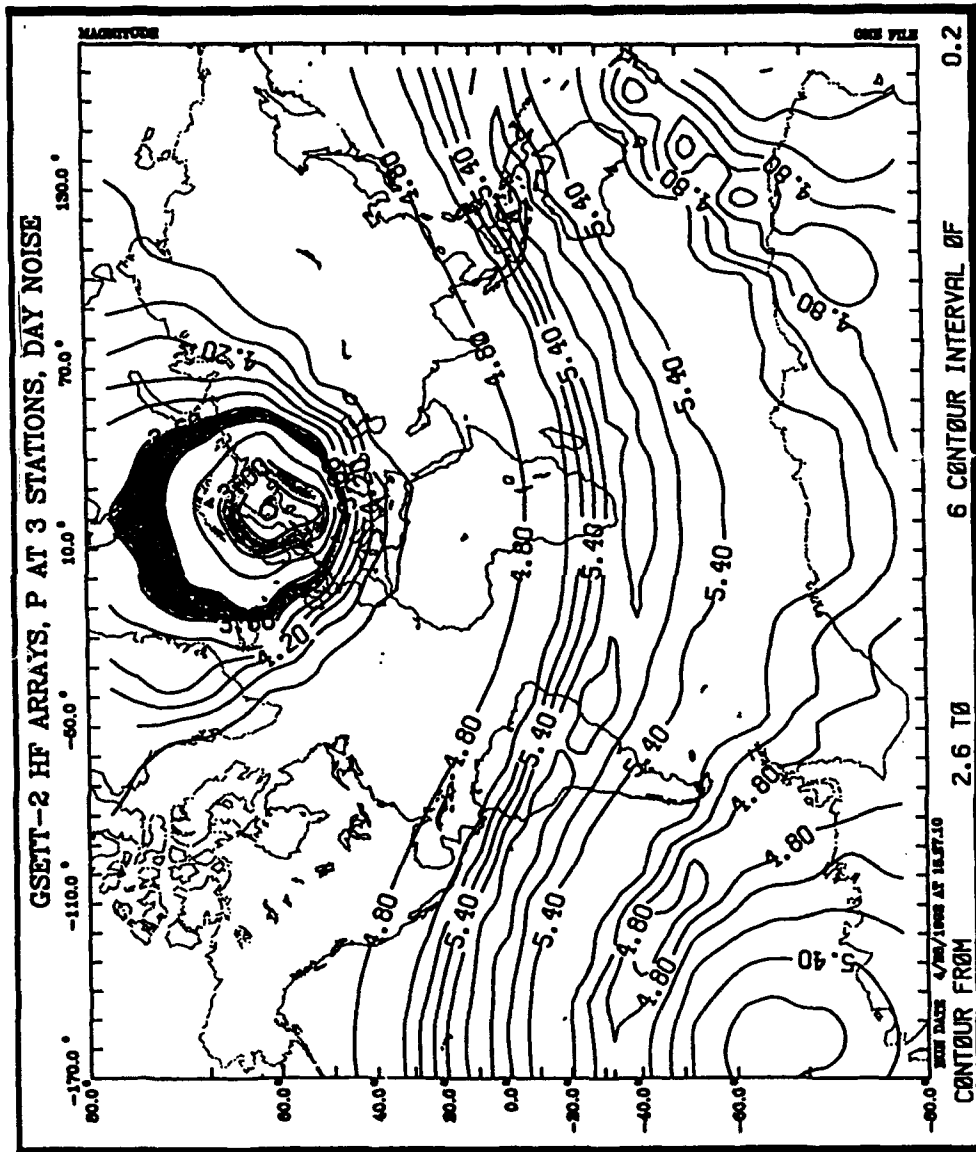


Figure 55: 90% M_{Lg} Detection Threshold for 4-Array Network. (a) Detection criteria requiring 3 P phases at any three stations. (b) Detection criteria requiring 2 P phases at any two stations or one Pg and one Lg at any station.

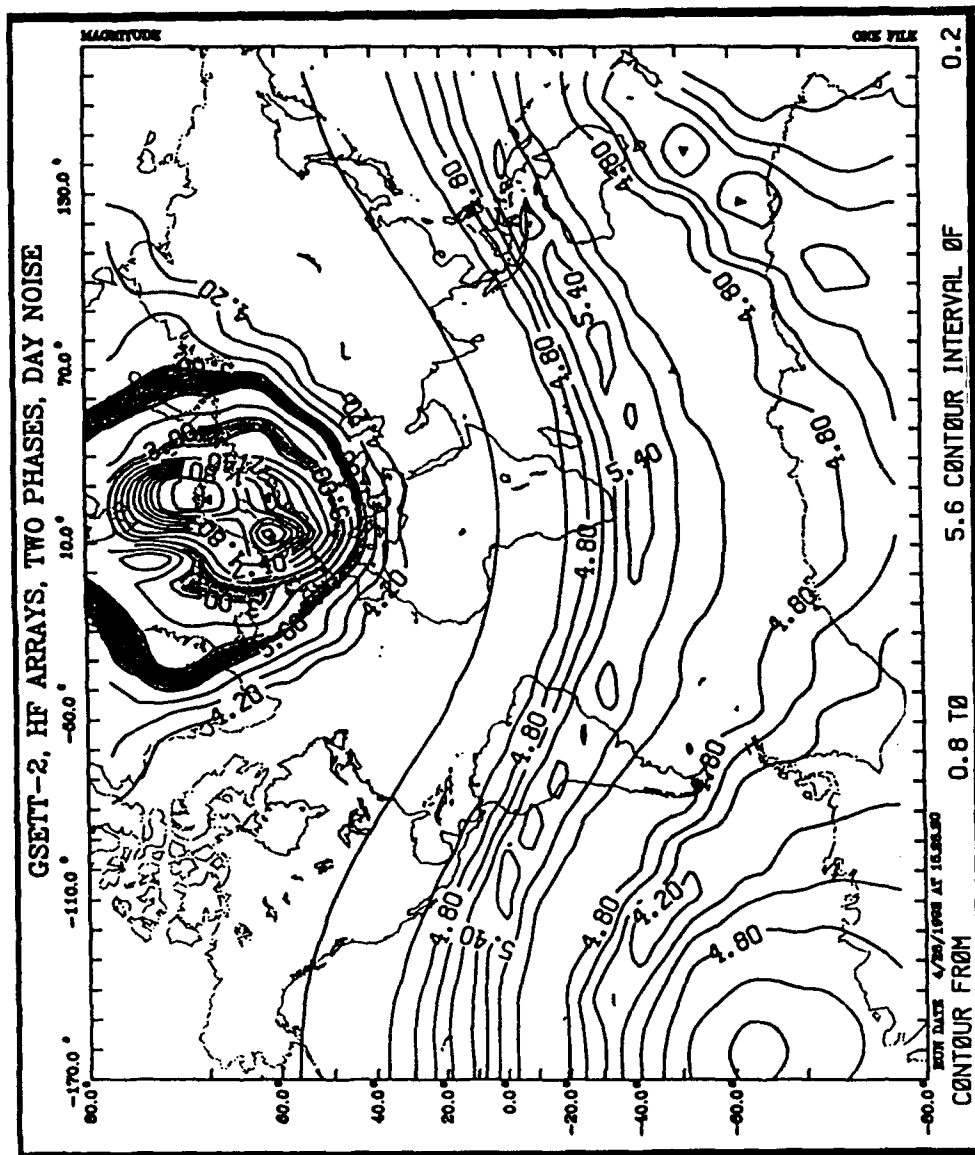


Figure 55(b):

Table 14: GSETT-2 90% M_{Lg} Detection Threshold

AREA	2 P	Min-Max M _{Lg}	3 P	Min-Max M _{Lg}	Difference
	Median M _{Lg}		Median M _{Lg}		Increase (Median)
World	3.0	(1.8 - 4.3)	3.2	(2.0 - 4.4)	0.2
Eurasia	2.9	(1.8 - 3.9)	3.0	(2.0 - 4.1)	0.1
Australia and S.Pac	3.3	(2.6 - 4.0)	3.7	(3.3 - 4.1)	0.4
Indian Ocean and S. Atlantic	3.9	(3.5 - 4.3)	4.0	(3.6 - 4.4)	0.1
South America and S. Pac	3.7	(3.2 - 4.3)	4.0	(3.5 - 4.4)	0.3
North America	3.5	(3.0 - 4.0)	3.8	(3.3 - 4.2)	0.3
North Atlantic Ocean	3.2	(2.5 - 3.9)	3.4	(2.8 - 4.0)	0.2

Table 15: GSETT-2 Sub-networks 90% M_{Lg} Detection Threshold, Requiring 3 P

AREA	12-Array		4-Array	
	Median M_{Lg}	Min-Max M_{Lg}	Median M_{Lg}	Min-Max M_{Lg}
World	3.1	(2.0 - 4.1)	4.3	(2.6 - 5.9)
Eurasia	3.0	(2.0 - 3.9)	4.2	(2.6 - 5.9)
Australia and S.Pac	3.7	(3.3 - 4.0)	5.2	(4.4 - 5.9)
Indian Ocean and S. Atlantic	3.9	(3.6 - 4.1)	5.2	(4.5 - 5.9)
South America and S. Pac	3.7	(3.4 - 4.1)	5.1	(4.4 - 5.9)
North America	3.7	(3.3 - 4.1)	5.3	(4.6 - 5.9)
North Atlantic Ocean	3.3	(2.8 - 3.8)	4.1	(3.3 - 5.9)

Table 16: GSETT-2 Sub-networks Requiring 2 P or 2 Local Phases

AREA	12-ARR		4-ARR	
	Median M_{Lg}	Min-Max M_{Lg}	Median M_{Lg}	Min-Max M_{Lg}
World	2.7	(0.9 - 4.6)	3.2	(0.9 - 5.5)
Eurasia	2.5	(0.9 - 4.1)	3.2	(0.9 - 5.5)
Australia and S.Pac	3.5	(2.8 - 4.2)	4.8	(4.0 - 5.5)
Indian Ocean and S. Atlantic	4.1	(3.7 - 4.6)	4.9	(4.2 - 5.5)
South America and S. Pac	4.1	(3.7 - 4.5)	4.8	(4.0 - 5.5)
North America	4.1	(3.7 - 4.5)	4.9	(4.3 - 5.5)
North Atlantic Ocean	3.3	(2.5 - 4.1)	3.7	(2.8 - 4.6)

for the GSETT-2 stations where available and substitute noise estimates otherwise, as listed in Table 13. The 90% M_{Lg} Detection Threshold for the Hypothetical 85-Station Network is shown in Figure 56(a) and the difference plot showing the improvement in detection capability over the GSETT-2 network is shown in Figure 56(b). Thresholds for each area are listed in Table 17 for the Hypothetical Network and are compared to the GSETT-2 Network.

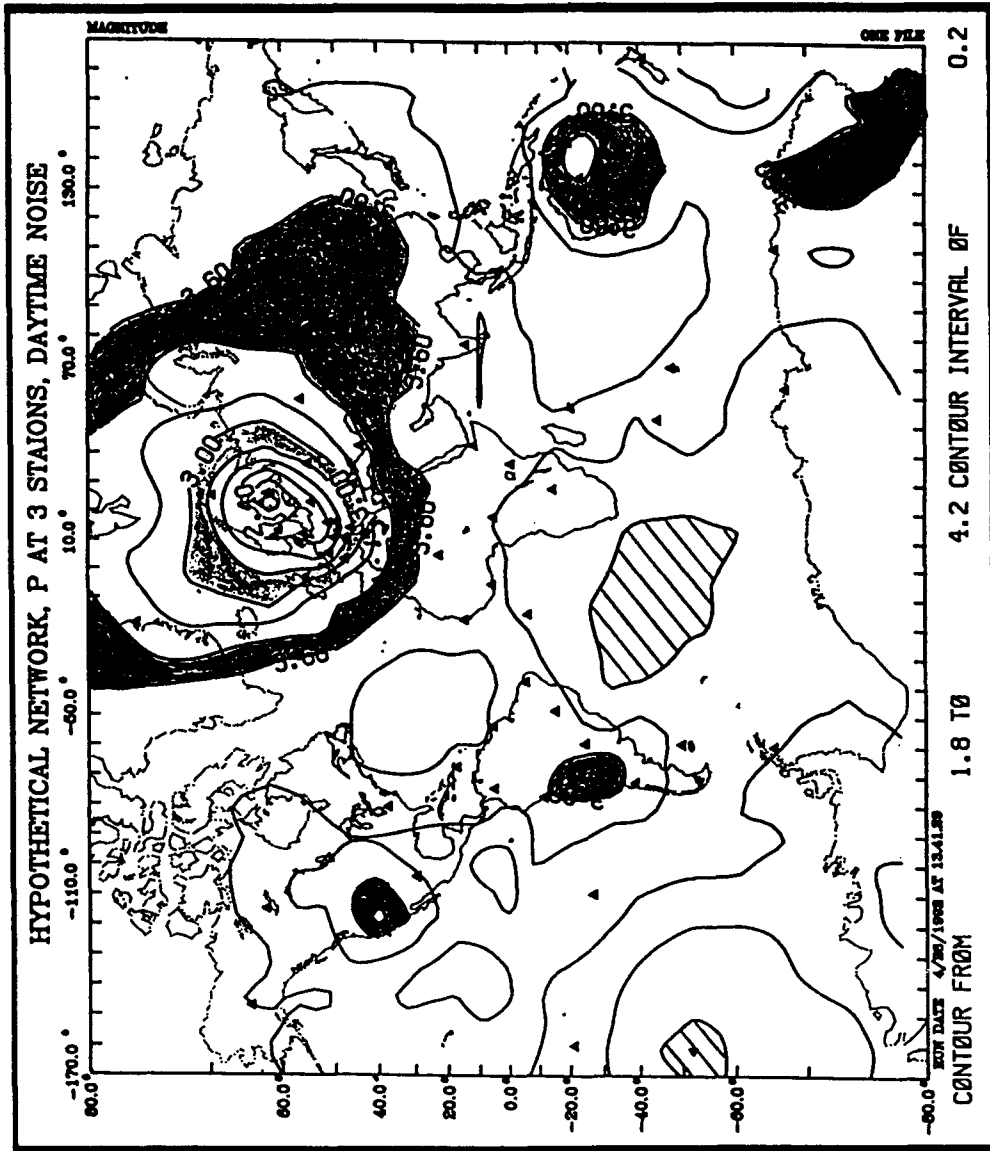


Figure 56: 90% M_{Lg} Detection Threshold for Hypothetical 85-Station Network. (a) Detection criteria requiring 3 P phases at any three stations. (b) Difference plot showing theoretical improvement in detection threshold compared to the GSETT-2 Network shown in Figure 53(b).

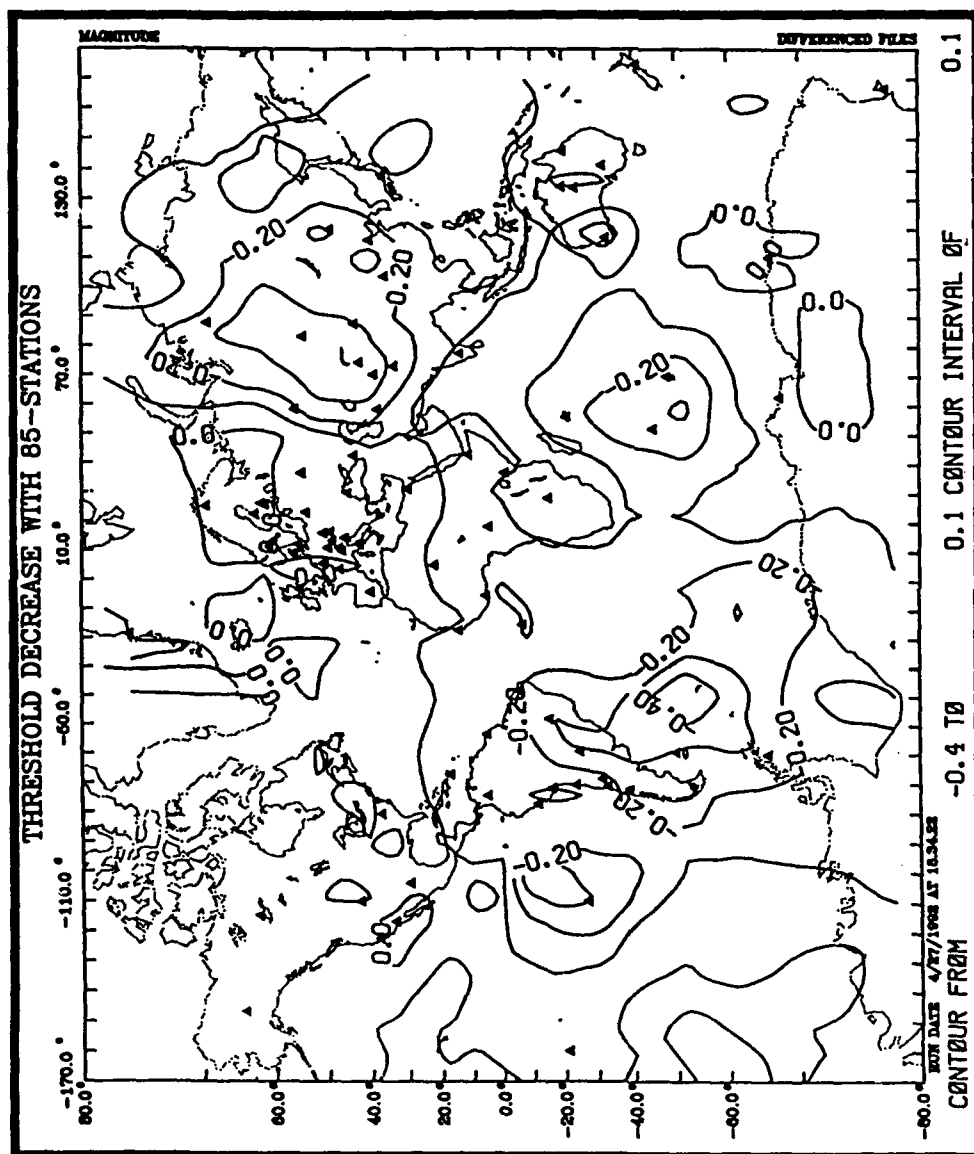


Table 17: Hypothetical 85-Station Network Requiring 3 P Phases

AREA	HYPO85 Sta		GSETT 2		Diff.
	Median M _{Lg}	Min-Max M _{Lg}	Median M _{Lg}	Min-Max M _{Lg}	Decrease (Median)
World	3.1	(2.0 - 4.1)	3.2	(2.0 - 4.4)	- 0.1
Eurasia	3.0	(2.0 - 3.9)	3.0	(2.0 - 4.1)	0.0
Australia and S.Pac	3.7	(3.3 - 4.0)	3.7	(3.3 - 4.1)	0.0
Indian Ocean and S. Atlantic	3.9	(3.6 - 4.1)	4.0	(3.6 - 4.4)	- 0.1
South America and S. Pac	3.7	(3.4 - 4.1)	4.0	(3.5 - 4.4)	- 0.3
North America	3.7	(3.3 - 4.1)	3.8	(3.3 - 4.2)	- 0.1
North Atlantic Ocean	3.3	(2.8 - 3.8)	3.4	(2.8 - 4.0)	- 0.1

Summary

The detection threshold for the GSETT-2 network with 2 P-phases ranges from a large area of thresholds lower than 3.0 which includes Fennoscandia, western Europe, and the western part of the former Soviet Union and parts of the Barents Sea to a large area in the South Atlantic ocean where the thresholds are above 4.0. Most of North America has a detection threshold less than 3.6. Smaller local minima occur in Western South America and Australia. When 3 P-phases are required, the median world threshold increases by 0.2 from 3.0 to 3.2. In areas of isolated groups of stations (Australia, South America), the requirement of an additional P-phase raises the threshold by as much as 0.4.

The high-frequency and short-period arrays alone have a worldwide median threshold of 0.1 greater than the full GSETT-2 network. In the area of South America and Southwest Pacific, the increase is 0.3.

The addition of 29 stations to make the hypothetical network, mostly in the Southern Hemisphere and eastern Eurasia, lowers the worldwide median threshold by only 0.1. In the South Pacific Ocean the additional stations lowered the median threshold by 0.4. This small decrease in threshold with the addition of so many stations is not surprising considering that the stations were added in isolated locations and the simulation required 3-P phases for a valid network detection.

Future Work

Noise estimates have been improved for some GSETT-2 stations or have been calculated where they were not available at the time of this study. This was possible because waveforms and instrument responses have been added to the GSETT-2 database. Future work will first consist of improving the estimates of input parameters. Specifically, studies of detection threshold requirements for each station will be completed. Then, the program can be used to answer the question of how many stations and of which type are required to monitor specific areas of the globe.

Acknowledgments

We thank Ann Seteau for helpful editing of this report. We also appreciate Jerry Carter's help in calculation of the noise spectra.

References

- Bratt, S. R., H.J. Swanger, R.J. Stead, F. Ryall, and T.C. Bache (1990). Initial Results from the Intelligent Monitoring System. *Bull. Seism. Soc. Am.*, Vol. 80, No. 6, pp 1852-1873.
- Bratt, S. R. (1992). "Global Monitoring to Low Thresholds: Where We Stand," Proceedings of the 13th Annual DARPA/PL Seismic Research Symposium (8-10 October), Keystone, Colorado, Invited Paper, page 2. PL-TR-91-2208, ADA241325.
- Coyne, J. M. (1991). MASSPROC, Center for Seismic Studies Manual Page for Massproc.
- Doornbos, D.J., E. R. Engdahl, and T. H. Jordan (1991). "International Seismological Observing Period Preliminary Science Plan", Proceedings of ISOP (19-22 March), Denver, Colorado.
- Sereno, T. J., S. R. Bratt, G. Yee (1990). "NETSIM: A Computer Program for Simulating Detection and Location Capability of Regional Seismic Networks". *Annual Technical Report* SAIC-90/1163, Sci. Appl. Int. Corp., San diego, Calif.
- Sereno, T. J. (1991). Simulation of the Detection and Location Capability of Regional Seismic Networks in the Soviet Union. *Final Report* SAIC-91/1061

Summary Note on Starting and Improving a Regional Network

Anne Suteau-Henson

Introduction

This brief note summarizes and integrates the results of our research related to the way the US would proceed to monitor with an in-country regional network of three-component (3-C) stations and arrays. Of particular interest are the following questions:

- What initial capabilities can be expected of both 3-C stations and arrays?
- How would the network capabilities improve with time?

We do not address the questions of site selection or the mix of 3-C stations and arrays. It is obvious that arrays are preferable to 3-C stations given a fixed number of sites and that quiet sites are preferable to noisy ones. Questions of the station mix require both political (array sites require far more area than 3-C sties) and economic (arrays are more expensive than 3-C stations) inputs, and noise can be estimated from past experience based on geology, proximity to water, cultural noise sources, and weather. Our experience with 3-C stations is derived from the IRIS/IDA stations within the former Soviet Union and from the 3-C stations of the high-frequency arrays in Scandinavia. The NORESS and ARCESS arrays provided the data for the array studies. Relevant studies were published by other researchers, and we will refer to them, as appropriate.

To start a new in-country monitoring network, decisions must be made regarding the number of stations and their type (arrays, 3-C stations, or both). Other factors involved are, for arrays, the number of elements, their spacing, and the array aperture, and for both station types, the useful frequency band. Then, computational methods and parameters for automated processing must be selected. A number of studies, mostly empirical, have compared the capabilities of 3-C stations and arrays for direction (especially, azimuth) estimation and phase identification. Their relative performance in other aspects of monitoring (detection, phase association, distance estimation, magnitude estimation, discrimination) have received comparatively less attention. Most studies agree that the critical factors affecting the performance of 3-C stations more than that of arrays are signal-to-noise ratio (SNR) and site-dependence. In the following, we summarize our and other results concerning the monitoring capabilities one can expect from 3-C stations and arrays.

Azimuth Estimation

When starting a new regional network, it is reasonable to use processing parameters that "worked" for other operational networks. Several studies report azimuth errors obtained with appropriate (but not optimized) processing parameters. For example, Suteau-Henson (1990), using automated processing, obtained a standard deviation (s.d.) of 14 deg for azimuth estimates of 3-C data at NORESS with 3-C SNR > 2 , compared to 11 deg for the vertical-array data from the same events. Bame *et al.* (1990), studying regional Pn at the NORESS array, found that most azimuth errors were less than 20 deg, with a mean close to zero, with appropriate processing parameters. For regional P-waves at 3-C RSTN stations, Walck and Chael (1991) found that more than 75% of azimuths had errors less than 20 deg without optimization. Ruud and Husebye (1992), testing a 3-C detector on 3 days of data from the NORESS element C4 and comparing the results to those in the NORESS array bulletin, found 3-C azimuth errors within 20 deg. Therefore, little difference was found in the azimuth estimation performance of 3-C stations and arrays under two conditions: sufficient SNR and "good" site. In the following, we review in more detail the effects of SNR and site-dependence.

Harris (1990) used theoretical considerations, simulation, and an empirical study to compare the direction estimation performance of 3-C stations and arrays over the entire SNR range. His results indicate that, as SNR decreases, a gradual and uniform deterioration occurs for 3-C stations, until an asymptotic plateau is reached at very low SNR. For arrays, there is a sharp transition between a high SNR floor and a low SNR plateau. There is a SNR band for which arrays have small errors, but not 3-C stations. This is confirmed by our empirical study at NORESS (Suteau-Henson, 1990), that found the capability of 3-C stations to be critically dependent on SNR. For 3-C SNR > 2 , the scatter is very large, and therefore, the 3-C direction estimates are unreliable. Noise had no significant effect on the array estimates, indicating Harris' low SNR plateau was not reached. Similarly, a 3-C SNR threshold of 5 dB were obtained by Walck and Chael (1991) at RSTN stations, and by Jarpe and Dowla (1991) at the high-frequency element of NORESS, for useful azimuth estimates from polarization of 3-C data.

The other factor significantly affecting azimuth estimation at 3-C stations is site-dependence. Suteau-Henson (1990) observed a site-dependence for individual 3-C elements within NORESS. Similar observations were made in other studies, outside Scandinavia. For example, Walck and Chael (1991) found that the azimuth accuracy varied with receiver structure for regional P waves at RSTN stations (see also US/GSE/49, 1987). Stations in Precambrian terranes yielded very accurate azimuths for SNR > 5 dB, while for stations in sedimentary rocks, either no reasonable azimuths could be obtained or a strong dependence on the computational method existed (i.e., assumptions about the type of P

particle motion). The effect of this factor on monitoring was particularly brought to light by Riviere-Barbier *et al.* (1992), who processed one month of continuous data from a network of four 3-C IRIS/IDA stations in the Soviet Union. Stations near geologic boundaries showed systematic azimuth and incidence errors, that could be related to lateral heterogeneities in structure. Also, because of receiver structure, no useful azimuths could be obtained at two of the stations when assuming rectilinear particle motion for P-waves.

Phase Identification

The capabilities of 3-C stations and arrays for phase identification are also different. While arrays can easily classify detections as teleseismic P, regional P, regional S, or noise, based on their apparent velocity from f-k analysis (Bratt *et al.*, 1990), an inadequate performance (only about 75%) was obtained at the 3-C IRIS/IDA stations in the Soviet Union, using polarization, frequency, and SNR as predictors of detection type (Suteau-Henson, 1992a). Adequate performance, however, was obtained at the 3-C arrays of NORESS and ARCESS (about 90%) for a P versus S classification, using either a classical discriminant or a neural network. As for azimuth estimation, SNR is an important factor, and the performance increases to over 95% for 3-C SNR > 2 (Suteau-Henson, 1992b). Patnaik and Sereno (1991) found that, within NORESS or ARCESS, the variation in single-element performance was only of about 5% (with an average of about 80% for all SNRs and 90% for SNR > 2). They also showed that processing parameters for phase identification developed at one site could usefully be adapted to a new site: adequate performance was obtained by applying neural networks trained at different sites.

Detection and Bulletin Production

We are aware of only one study directly comparing a 3-C detector and bulletin with an array bulletin obtained from the same recordings (Ruud and Husebye, 1992). The 3-C SNR at NORESS element C4 in the 5-15 Hz band was about 6-8 dB lower than for the NORESS array. The 3-C detector picked almost all array-detected S-phases, but sometimes missed the preceding Pn. The 3-C epicenter solutions were less stable, due to phase identification problems, and Pn azimuth errors at low SNR, as expected. Clearly, azimuth errors, both random and systematic, become more critical as distance increases, and this effect requires careful consideration when designing a new network.

Knowledge Acquisition

In the previous section, we summarized the monitoring capabilities that could be expected from a new network. With time, the process of knowledge acquisition should result in their improvement. Here, we review what we have learned about processing optimization

when enough data have become available.

Because of the unique structure at each of the four 3-C IRIS/IDA stations they studied in the Soviet Union, Riviere-Barbier *et al.* (1992) improved azimuth estimation by customizing processing parameters at each station. At two stations, elliptical polarization had to be assumed to obtain reliable estimates. After such customizing, azimuths within ± 25 deg were obtained for about 70% of events at most stations. Other studies evaluated the improvement in azimuth estimation achievable with processing optimization. Bame *et al.* (1990) thus obtained a s.d. decrease from 20 to 11 deg at the NORESS array, and even to 2 deg for $\text{SNR} > 5$ dB and from some specific source regions. Walck and Chael (1991) observed a 5-10% improvement for parameters customized by 3-C station in the RSTN network. Parameter optimization resulted in a s.d. as low as 6 deg (similar to the uncertainty for the NORESS array) at the high-frequency 3-C element of NORESS (Jarpe and Dowla, 1991).

Phase identification can also be improved as more knowledge is acquired at a particular 3-C site. This is due to characteristic polarization for each regional phase at each site. For example, Suteau-Henson (1991) shows that regional P have different average incidence at ARCESS and NORESS, and difference in polarization results in better Sn versus Lg classification at NORESS than at ARCESS. Patnaik and Sereno (1991) shows that, on average, a 10-15% increase in correct identification is achieved when retraining a neural network for a new site, as opposed to using weights from another site.

Suteau-Henson (1992c) shows that both 3-C azimuth estimation and phase identification could be further improved by taking into account the variation of polarization with azimuth and distance for a given site. A detailed study at ARCESS indicates systematic azimuth errors varying within ± 10 deg, depending on source area. Also, at NORESS for example, Pn incidence is a strong function of distance, decreasing by 10 deg, on average, from the cross-over distance to the regional range. Near the cross-over distance, it also varies with azimuth, by over 5 deg.

Other factors affecting the performance of azimuth estimation and phase identification, and therefore, that can result in improvement when customized for each site, are:

- array geometry for arrays (Bame *et al.*, 1990);
- frequency band (Riviere-Barbier *et al.*, 1992; Suteau-Henson, 1992a; Bame *et al.*, 1990; Walck and Chael, 1991);
- time-bandwidth (Jarpe and Dowla, 1991).

Although Bame *et al.* (1990) found that time window length had little effect on azimuth

estimation at the NORESS array, most of the events they studied were from a particular azimuth range, and this effect should be further investigated for a variety of azimuths. Walck and Chael (1991) concluded that the particular computational method used to obtain 3-C azimuth estimates had relatively little effect on the performance for "good" sites and SNR. However, assumptions about particle motion (such as rectilinear or elliptical), inherent to every method, strongly affect the results (see also Riviere-Barbier *et al.*, 1992).

Conclusions

As 3-C stations are less costly than arrays, much effort has been devoted to evaluating their monitoring capabilities and comparing them to those of arrays. The main conclusions of these studies are that the performance of 3-C stations is more sensitive to low SNR and to receiver structure, and it has been possible to somewhat quantify these effects. However, as shown by many examples, their capabilities (and those of arrays as well) can be improved with time by customizing processing parameters and using acquired knowledge.

References

- Bame D. A., M. C. Walck, and K. L. Hiebert-Dodd (1990). Azimuth Estimation Capabilities of the NORESS Regional Seismic Array, *Bull. Seism. Soc. Am.* 80, 1999-2015.
- Bratt. S. R., H. J. Swanger, R. J. Stead, F. Ryall, and T. C. Bache (1990). Initial results from the intelligent monitoring system, *Bull. Seism. Soc. Am.* 80, 1852-1873.
- Harris D. B. (1990). Comparison of the Direction Estimation Performance of High-Frequency Seismic Arrays and Three-Component Stations, *Bull. Seism. Soc. Am.* 80, 1951-1968.
- Jarpe S. and F. Dowla (1991). Performance of High-Frequency Three-Component Stations for Azimuth Estimation from Regional Seismic Phases, *Bull. Seism. Soc. Am.* 81, 987-999.
- Patnaik, G. B., and T. J. Sereno (1991). A Neural Network Approach to Initial Phase Identification From Three-Component Polarization Measurements, *Proceedings of 13th Annual PLIDARPA Seismic Research Symposium*, 8-10 October 1991, Keystone, Colorado. PL-TR-91-2208, ADA241325.
- Riviere-Barbier F., A. Suteau-Henson, V. Z. Ryaboy, and J. A. Carter (1992). Analysis of Three-Component Data from IRIS/IDA Stations in the USSR, *Bull. Seism. Soc. Am.* 82, 192-220.
- Ruud B. O. and E. S. Husebye (1992). A New Three-Component Detector and Automatic Single-Station Bulletin Production, *Bull. Seism. Soc. Am.* 82, 221-237.
- Suteau-Henson A. (1990). Estimating Azimuth and Slowness from Three-Component and Array Stations, *Bull. Seism. Soc. Am.* 80, 1987-1998.
- Suteau-Henson A. (1991). Three-Component Analysis of Regional Phases at NORESS and ARCESS: Polarization and Phase Identification, *Bull. Seism. Soc. Am.* 81, 2419-2440.
- Suteau-Henson A. (1992a). Initial Phase Identification at the IRIS/IDA Stations in the USSR, *This Report*.
- Suteau-Henson A. (1992b). Initial Phase Identification from Polarization at ARCESS and NORESS: A Comparison Between Discriminant and Neural Network, *This Report*.
- Suteau-Henson A. (1992c). Variation of Regional P Polarization and Azimuth Estimation at NORESS and ARCESS, *Center for Seismic Studies Report*.
- Walck M.C. and E. P. Chael (1991). Optimal Backazimuth Estimation for Three-Component Recordings of Regional Seismic Events, *Bull. Seism. Soc. Am.* 81, 643-666.
- US/GSE/49 (1987). A recommendation for inclusion of azimuth as a reportable parameter for three-component stations, in *United States Delegation to the Conference on Disarmament*, Geneva, Switzerland, 37 pp.

DISTRIBUTION LIST

Prof. Thomas Ahrens
Seismological Lab, 252-21
Division of Geological & Planetary Sciences
California Institute of Technology
Pasadena, CA 91125

Prof. Keiiti Aki
Center for Earth Sciences
University of Southern California
University Park
Los Angeles, CA 90089-0741

Prof. Shelton Alexander
Geosciences Department
403 Deike Building
The Pennsylvania State University
University Park, PA 16802

Dr. Ralph Alewine, III
DARPA/NMRO
3701 North Fairfax Drive
Arlington, VA 22203-1714

Prof. Charles B. Archambeau
CIRES
University of Colorado
Boulder, CO 80309

Dr. Thomas C. Bache, Jr.
Science Applications Int'l Corp.
10260 Campus Point Drive
San Diego, CA 92121 (2 copies)

Prof. Muawia Barazangi
Institute for the Study of the Continent
Cornell University
Ithaca, NY 14853

Dr. Jeff Barker
Department of Geological Sciences
State University of New York
at Binghamton
Vestal, NY 13901

Dr. Douglas R. Baumgardt
ENSCO, Inc
5400 Port Royal Road
Springfield, VA 22151-2388

Dr. Susan Beck
Department of Geosciences
Building #77
University of Arizona
Tuscon, AZ 85721

Dr. T.J. Bennett
S-CUBED
A Division of Maxwell Laboratories
11800 Sunrise Valley Drive, Suite 1212
Reston, VA 22091

Dr. Robert Blandford
AFTAC/TT, Center for Seismic Studies
1300 North 17th Street
Suite 1450
Arlington, VA 22209-2308

Dr. G.A. Bollinger
Department of Geological Sciences
Virginia Polytechnical Institute
21044 Derring Hall
Blacksburg, VA 24061

Dr. Stephen Bratt
Center for Seismic Studies
1300 North 17th Street
Suite 1450
Arlington, VA 22209-2308

Dr. Lawrence Burdick
Woodward-Clyde Consultants
566 El Dorado Street
Pasadena, CA 91109-3245

Dr. Robert Burrige
Schlumberger-Doll Research Center
Old Quarry Road
Ridgefield, CT 06877

Dr. Jerry Carter
Center for Seismic Studies
1300 North 17th Street
Suite 1450
Arlington, VA 22209-2308

Dr. Eric Chael
Division 9241
Sandia Laboratory
Albuquerque, NM 87185

Prof. Vernon F. Cormier
Department of Geology & Geophysics
U-45, Room 207
University of Connecticut
Storrs, CT 06268

Prof. Steven Day
Department of Geological Sciences
San Diego State University
San Diego, CA 92182

Marvin Denny
U.S. Department of Energy
Office of Arms Control
Washington, DC 20585

Dr. Cliff Frolich
Institute of Geophysics
8701 North Mopac
Austin, TX 78759

Dr. Zoltan Der
ENSCO, Inc.
5400 Port Royal Road
Springfield, VA 22151-2388

Dr. Holly Given
IGPP, A-025
Scripps Institute of Oceanography
University of California, San Diego
La Jolla, CA 92093

Prof. Adam Dziewonski
Hoffman Laboratory, Harvard University
Dept. of Earth Atmos. & Planetary Sciences
20 Oxford Street
Cambridge, MA 02138

Dr. Jeffrey W. Given
SAIC
10260 Campus Point Drive
San Diego, CA 92121

Prof. John Ebel
Department of Geology & Geophysics
Boston College
Chestnut Hill, MA 02167

Dr. Dale Glover
Defense Intelligence Agency
ATTN: ODT-1B
Washington, DC 20301

Eric Fielding
SNEE Hall
INSTOC
Cornell University
Ithaca, NY 14853

Dr. Indra Gupta
Teledyne Geotech
314 Montgomery Street
Alexandria, VA 22314

Dr. Mark D. Fisk
Mission Research Corporation
735 State Street
P.O. Drawer 719
Santa Barbara, CA 93102

Dan N. Hagedorn
Pacific Northwest Laboratories
Battelle Boulevard
Richland, WA 99352

Prof Stanley Flatte
Applied Sciences Building
University of California, Santa Cruz
Santa Cruz, CA 95064

Dr. James Hannon
Lawrence Livermore National Laboratory
P.O. Box 808
L-205
Livermore, CA 94550

Dr. John Foley
NER-Geo Sciences
1100 Crown Colony Drive
Quincy, MA 02169

Dr. Roger Hansen
HQ AFTAC/TTR
Patrick AFB, FL 32925-6001

Prof. Donald Forsyth
Department of Geological Sciences
Brown University
Providence, RI 02912

Prof. David G. Harkrider
Seismological Laboratory
Division of Geological & Planetary Sciences
California Institute of Technology
Pasadena, CA 91125

Dr. Art Frankel
U.S. Geological Survey
922 National Center
Reston, VA 22092

Prof. Danny Harvey
CIRES
University of Colorado
Boulder, CO 80309

Prof. Donald V. Helmberger
Seismological Laboratory
Division of Geological & Planetary Sciences
California Institute of Technology
Pasadena, CA 91125

Prof. Eugene Herrin
Institute for the Study of Earth and Man
Geophysical Laboratory
Southern Methodist University
Dallas, TX 75275

Prof. Robert B. Herrmann
Department of Earth & Atmospheric Sciences
St. Louis University
St. Louis, MO 63156

Prof. Lane R. Johnson
Seismographic Station
University of California
Berkeley, CA 94720

Prof. Thomas H. Jordan
Department of Earth, Atmospheric &
Planetary Sciences
Massachusetts Institute of Technology
Cambridge, MA 02139

Prof. Alan Kafka
Department of Geology & Geophysics
Boston College
Chestnut Hill, MA 02167

Robert C. Kemerait
ENSCO, Inc.
445 Pineda Court
Melbourne, FL 32940

Dr. Max Koontz
U.S. Dept. of Energy/DP 5
Forrestal Building
1000 Independence Avenue
Washington, DC 20585

Dr. Richard LaCoss
MIT Lincoln Laboratory, M-200B
P.O. Box 73
Lexington, MA 02173-0073

Dr. Fred K. Lamb
University of Illinois at Urbana-Champaign
Department of Physics
1110 West Green Street
Urbana, IL 61801

Prof. Charles A. Langston
Geosciences Department
403 Deike Building
The Pennsylvania State University
University Park, PA 16802

Jim Lawson, Chief Geophysicist
Oklahoma Geological Survey
Oklahoma Geophysical Observatory
P.O. Box 8
Leonard, OK 74043-0008

Prof. Thorne Lay
Institute of Tectonics
Earth Science Board
University of California, Santa Cruz
Santa Cruz, CA 95064

Dr. William Leith
U.S. Geological Survey
Mail Stop 928
Reston, VA 22092

Mr. James F. Lewkowicz
Phillips Laboratory/GPEH
Hanscom AFB, MA 01731-5000(2 copies)

Mr. Alfred Lieberman
ACDA/VI-OA State Department Building
Room 5726
320-21st Street, NW
Washington, DC 20451

Prof. L. Timothy Long
School of Geophysical Sciences
Georgia Institute of Technology
Atlanta, GA 30332

Dr. Randolph Martin, III
New England Research, Inc.
76 Olcott Drive
White River Junction, VT 05001

Dr. Robert Masse
Denver Federal Building
Box 25046, Mail Stop 967
Denver, CO 80225

Dr. Gary McCartor
Department of Physics
Southern Methodist University
Dallas, TX 75275

Prof. Thomas V. McEvilly
Seismographic Station
University of California
Berkeley, CA 94720

Dr. Art McGarr
U.S. Geological Survey
Mail Stop 977
U.S. Geological Survey
Menlo Park, CA 94025

Dr. Keith L. McLaughlin
S-CUBED
A Division of Maxwell Laboratory
P.O. Box 1620
La Jolla, CA 92038-1620

Stephen Miller & Dr. Alexander Florence
SRI International
333 Ravenswood Avenue
Box AF 116
Menlo Park, CA 94025-3493

Prof. Bernard Minster
IGPP, A-025
Scripps Institute of Oceanography
University of California, San Diego
La Jolla, CA 92093

Prof. Brian J. Mitchell
Department of Earth & Atmospheric Sciences
St. Louis University
St. Louis, MO 63156

Mr. Jack Murphy
S-CUBED
A Division of Maxwell Laboratory
11800 Sunrise Valley Drive, Suite 1212
Reston, VA 22091 (2 Copies)

Dr. Keith K. Nakanishi
Lawrence Livermore National Laboratory
L-025
P.O. Box 808
Livermore, CA 94550

Dr. Carl Newton
Los Alamos National Laboratory
P.O. Box 1663
Mail Stop C335, Group ESS-3
Los Alamos, NM 87545

Dr. Bao Nguyen
HQ AFTAC/TTR
Patrick AFB, FL 32925-6001

Prof. John A. Orcutt
IGPP, A-025
Scripps Institute of Oceanography
University of California, San Diego
La Jolla, CA 92093

Prof. Jeffrey Park
Kline Geology Laboratory
P.O. Box 6666
New Haven, CT 06511-8170

Dr. Howard Patton
Lawrence Livermore National Laboratory
L-025
P.O. Box 808
Livermore, CA 94550

Dr. Frank Pilotte
HQ AFTAC/TT
Patrick AFB, FL 32925-6001

Dr. Jay J. Pulli
Radix Systems, Inc.
2 Taft Court, Suite 203
Rockville, MD 20850

Dr. Robert Reinke
ATTN: FCTVTD
Field Command
Defense Nuclear Agency
Kirtland AFB, NM 87115

Prof. Paul G. Richards
Lamont-Doherty Geological Observatory
of Columbia University
Palisades, NY 10964

Mr. Wilmer Rivers
Teledyne Geotech
314 Montgomery Street
Alexandria, VA 22314

Dr. George Rothe
HQ AFTAC/TTR
Patrick AFB, FL 32925-6001

Dr. Alan S. Ryall, Jr.
DARPA/NMRO
3701 North Fairfax Drive
Arlington, VA 22209-1714

Dr. Richard Sailor
TASC, Inc.
55 Walkers Brook Drive
Reading, MA 01867

Prof. Charles G. Sammis
Center for Earth Sciences
University of Southern California
University Park
Los Angeles, CA 90089-0741

Prof. Christopher H. Scholz
Lamont-Doherty Geological Observatory
of Columbia University
Palisades, CA 10964

Dr. Susan Schwartz
Institute of Tectonics
1156 High Street
Santa Cruz, CA 95064

Secretary of the Air Force
(SAFRD)
Washington, DC 20330

Office of the Secretary of Defense
DDR&E
Washington, DC 20330

Thomas J. Sereno, Jr.
Science Application Int'l Corp.
10260 Campus Point Drive
San Diego, CA 92121

Dr. Michael Shore
Defense Nuclear Agency/SPSS
6801 Telegraph Road
Alexandria, VA 22310

Dr. Matthew Sibol
Virginia Tech
Seismological Observatory
4044 Derring Hall
Blacksburg, VA 24061-0420

Prof. David G. Simpson
IRIS, Inc.
1616 North Fort Myer Drive
Suite 1440
Arlington, VA 22209

Donald L. Springer
Lawrence Livermore National Laboratory
L-025
P.O. Box 808
Livermore, CA 94550

Dr. Jeffrey Stevens
S-CUBED
A Division of Maxwell Laboratory
P.O. Box 1620
La Jolla, CA 92038-1620

Lt. Col. Jim Stobie
ATTN: AFOSR/NL
Bolling AFB
Washington, DC 20332-6448

Prof. Brian Stump
Institute for the Study of Earth & Man
Geophysical Laboratory
Southern Methodist University
Dallas, TX 75275

Prof. Jeremiah Sullivan
University of Illinois at Urbana-Champaign
Department of Physics
1110 West Green Street
Urbana, IL 61801

Prof. L. Sykes
Lamont-Doherty Geological Observatory
of Columbia University
Palisades, NY 10964

Dr. David Taylor
ENSCO, Inc.
445 Pineda Court
Melbourne, FL 32940

Dr. Steven R. Taylor
Los Alamos National Laboratory
P.O. Box 1663
Mail Stop C335
Los Alamos, NM 87545

Prof. Clifford Thurber
University of Wisconsin-Madison
Department of Geology & Geophysics
1215 West Dayton Street
Madison, WS 53706

Prof. M. Nafi Toksoz
Earth Resources Lab
Massachusetts Institute of Technology
42 Carleton Street
Cambridge, MA 02142

Dr. Larry Turnbull
CIA-OSWR/NED
Washington, DC 20505

DARPA/RMO/SECURITY OFFICE
3701 North Fairfax Drive
Arlington, VA 22203-1714

Dr. Gregory van der Vink
IRIS, Inc.
1616 North Fort Myer Drive
Suite 1440
Arlington, VA 22209

HQ DNA
ATTN: Technical Library
Washington, DC 20305

Dr. Karl Veith
EG&G
5211 Auth Road
Suite 240
Suitland, MD 20746

Defense Intelligence Agency
Directorate for Scientific & Technical Intelligence
ATTN: DTIB
Washington, DC 20340-6158

Prof. Terry C. Wallace
Department of Geosciences
Building #77
University of Arizona
Tuscon, AZ 85721

Defense Technical Information Center
Cameron Station
Alexandria, VA 22314 (2 Copies)

Dr. Thomas Weaver
Los Alamos National Laboratory
P.O. Box 1663
Mail Stop C335
Los Alamos, NM 87545

TACTEC
Battelle Memorial Institute
505 King Avenue
Columbus, OH 43201 (Final Report)

Dr. William Wortman
Mission Research Corporation
8560 Cinderbed Road
Suite 700
Newington, VA 22122

Phillips Laboratory
ATTN: XPG
Hanscom AFB, MA 01731-5000

Prof. Francis T. Wu
Department of Geological Sciences
State University of New York
at Binghamton
Vestal, NY 13901

Phillips Laboratory
ATTN: GPE
Hanscom AFB, MA 01731-5000

AFTAC/CA
(STINFO)
Patrick AFB, FL 32925-6001

Phillips Laboratory
ATTN: TSML
Hanscom AFB, MA 01731-5000

DARPA/PM
3701 North Fairfax Drive
Arlington, VA 22203-1714

Phillips Laboratory
ATTN: SUL
Kirtland, NM 87117 (2 copies)

DARPA/RMO/RETRIEVAL
3701 North Fairfax Drive
Arlington, VA 22203-1714

Dr. Michel Bouchon
I.R.I.G.M.-B.P. 68
38402 St. Martin D'Heres
Cedex, FRANCE

Dr. Michel Campillo
Observatoire de Grenoble
I.R.I.G.M.-B.P. 53
38041 Grenoble, FRANCE

Dr. Jorg Schlittenhardt
Federal Institute for Geosciences & Nat'l Res.
Postfach 510153
D-3000 Hannover 51, GERMANY

Dr. Kin Yip Chun
Geophysics Division
Physics Department
University of Toronto
Ontario, CANADA

Dr. Johannes Schweitzer
Institute of Geophysics
Ruhr University/Bochum
P.O. Box 1102148
4360 Bochum 1, GERMANY

Prof. Hans-Peter Harjes
Institute for Geophysics
Ruhr University/Bochum
P.O. Box 102148
4630 Bochum 1, GERMANY

Prof. Eystein Husebye
NTNF/NORSAR
P.O. Box 51
N-2007 Kjeller, NORWAY

David Jepsen
Acting Head, Nuclear Monitoring Section
Bureau of Mineral Resources
Geology and Geophysics
G.P.O. Box 378, Canberra, AUSTRALIA

Ms. Eva Johannisson
Senior Research Officer
National Defense Research Inst.
P.O. Box 27322
S-102 54 Stockholm, SWEDEN

Dr. Peter Marshall
Procurement Executive
Ministry of Defense
Blacknest, Brimpton
Reading FG7-FRS, UNITED KINGDOM

Dr. Bernard Massinon, Dr. Pierre Mechler
Societe Radiomana
27 rue Claude Bernard
75005 Paris, FRANCE (2 Copies)

Dr. Svein Mykkeltveit
NTNF/NORSAR
P.O. Box 51
N-2007 Kjeller, NORWAY (3 Copies)

Prof. Keith Priestley
University of Cambridge
Bullard Labs Dept. of Earth Sciences
Madingley Rise, Madingley Road
Cambridge CB3 0EZ, ENGLAND